NANOSCALE SCANNING ELECTROCHEMICAL MICROSCOPY FOR STUDY OF CARBON MATERIALS AND HIGH-RESOLUTION IMAGING

by

Ran Chen

BS, Nanjing University, 2010

Submitted to the Graduate Faculty of

the Kenneth P. Dietrich School of Arts and Sciences in partial fulfillment

of the requirements for the degree of

Doctor of Philosophy

University of Pittsburgh

2017

UNIVERSITY OF PITTSBURGH

DIETRICH SCHOOL OF ARTS AND SCIENCES

This dissertation was presented

by

Ran Chen

It was defended on

August 21, 2017

and approved by

Steve G. Weber, Professor, Department of Chemistry

Adrian C. Michael, Professor, Department of Chemistry

Xinyan Cui, Professor, Department of Bioengineering

Dissertation Advisor: Shigeru Amemiya, Professor, Department of Chemistry

NANOSCALE SCANNING ELECTROCHEMICAL MICROSCOPY FOR STUDY OF CARBON MATERIALS AND HIGH-RESOLUTION IMAGING

Ran Chen, PhD

University of Pittsburgh, 2017

The nanogap voltammetry based on Scanning Electrochemical Microscopy (SECM) can monitor and study fast electron transfer (ET) reaction on macroscopic substrates of interest. The understanding of the electrochemical reactivity of carbon nanomaterials is of great importance not only for the application purposes, but also for fundamental electrochemistry. There are controversies about how the electronical reactivity of these materials depend on the electronic structures, defects and contamination. One theme of my PhD work is to study the electrochemical reactivity of various carbon nanomaterials using nanogap voltammetry based on SECM.

On the other hand, SECM at nanometer scale is a powerful technique, with unique advantages and unprecedented measurement capabilities, such as very high spatial resolution for surface imaging. However, it has been challenging to reliably characterize the size and geometry of the nanometer-size electrodes. The other aim of my PhD work is the development of methods for fabricating and characterizing nanoelectrodes for SECM.

Therefore, this thesis is based on two sections. In the first section, I fabricate graphene electrodes based on graphene grown by chemical vapor deposition, and apply nanogap voltammetry to study the ultrafast ET kinetics at graphene. I also study the ultrafast ET kinetics at highly ordered pyrolytic graphite (HOPG) with nanogap voltammetry. In the second section, I develop carbon nanoprobes with high electrochemical reactivity and well-controlled size and geometry based on chemical vapor deposition of carbon in quartz nanopipets. I also characterized the size and geometry of the nanopipets that support interfaces between two immiscible electrolyte

solutions (ITIES). I then prove the utility of such nanopipets by the SECM imaging on 100 nm diameter Si_3N_4 nanopores.

TABLE OF CONTENTS

1.0 INTRODUCTION 1

1.1 REFERENCES 4

2.0 ULTRAFAST ELECTRON TRANSFER KINETICS OF GRAPHENE GROWN BY CHEMICAL VAPOR DEPOSITION 5

2.1 INTRODUCTION 5

2.2 EXPERIMENTAL SECTION 8

2.3 RESULTS AND DISCUSSION 9

2.4 CONCLUSIONS 13

2.5 SUPPORTING INFORMATION 14

2.5.1 Chemicals and Materials 14

2.5.2 CVs at Polymer-Supported Graphene. 15

2.5.3 SECM Characterization of Pt Tips. 17

2.5.4 SECM-Based Nanogap Voltammetry. 18

2.5.5 Analysis of Nanogap Voltammograms. 20

2.5.6 Effects of Airborne Contamination on the FcMeOH Couple. 23

2.5.7 Effects of Airborne Contamination on the $Fe(CN)_6^{4-/3-}$ Couple. 24

ACKNOWLEDGEMENTS 27

2.6 REFERENCES 28

3.0 ORIGIN OF ASYMMETRY OF PAIRED NANOGAP VOLTAMMOGRAMS BASED ON SCANNING ELECTROCHEMICAL MICROSCOPY: CONTAMINATION NOT ADSORPTION 31

3.1 INTRODUCTION 31

3.2 THEORY 34

3.2.1 SECM-Based Nanogap Voltammetry. 34

3.2.2 Model. 35

3.2.3 Fc^+ Adsorption on the HOPG Surface. 38

3.2.4 Fc^{2+} Adsorption on the Glass Surface. 41

3.3 EXPERIMENTAL SECTION 43

3.3.1 Chemicals and Materials 43

3.3.2 Tip Fabrication. 44

3.3.3 SECM Measurement. 44

3.4 RESULTS AND DISSCUSSION 45

3.4.1 Nanogap Voltammetry with Non-Protected HOPG. 45

3.4.2 Nanogap Voltammetry with Water-Protected HOPG. 48

3.4.3 Weak Fc^+ Adsorption on the HOPG Surface. 50

3.4.4 Outer-Sphere ET Pathway of the $Fc^{2+/+}$ Couple at the HOPG Surface. ... 53

3.4.5 Misconception about Electron Exchange at the Glass Surface. 54

3.5 CONCLUSIONS 55

3.6 SUPPORTING INFORMATION 58

3.6.1 Dimensionless model. 58

3.6.2 Bipotentiostat. 62

3.6.3 Identical Diffusion Coefficient of Fc^+ and Fc^{2+} as Determined by Nanogap Voltammetry. 63

3.6.4 Negligible Drift of the Tip–HOPG Distance 64

3.6.5 Analysis of Nanogap Voltammograms. 65

3.6.6 Analysis of CVs of Weak Fc^+ Adsorption on the HOPG Surface. 67

3.6.7 Derivation of Eqs 23 and 24. 70

3.6.8 Derivation of Eqs 25. 71

ACKNOWLEDGEMENTS 72

3.7 REFERENCES 73

4.0 FOCUSED-ION-BEAM-MILLED CARBON NANOELECTRODES FOR SCANNING ELECTROCHEMICAL MICROSCOPY 77

4.1 INTRODUCTION 77

4.2 THEORY 79

4.3 EXPERIMENTAL SECTION 83

4.3.1 Chemicals and Materials 83

4.3.2 Tip Fabrication and Characterization. 83

4.3.3 Electrochemical Measurements. 84

4.4 RESULTS AND DISCUSSION 85

4.4.1 TEM, SEM and FIB Imaging. 85

4.4.2 Voltammetric Characterization. 87

4.4.3 Approach Curves at an Insulating Substrate 89

4.4.4 Approach Curves at a Conductive Substrate 92

4.4.5 Electrostatic Tip Damage. 95

4.5 CONCLUSIONS 96

ACKNOWLEDGEMENTS 98

4.6 REFERENCES 99

5.0 CHARACTERIZATION OF NANOPIPET-SUPPORTED ITIES TIPS FOR SCANNING ELECTROCHEMICAL MICROSCOPY OF SINGLE SOLID-STATE NANOPORES 103

5.1 INTRODUCTION 103

5.2 EXPERIMENTAL SECTION 106

5.2.1 Chemicals and Materials 106

5.2.2 Tip Fabrication. 106

5.2.3 TEM Characterization. 107

5.2.4 SECM Measurement. 108

5.3 RESUTLS AND DISSCUSSION 108

5.3.1 High-Magnification TEM Images of Quartz Nanopipets. 108

5.3.2 Nanopipet-Supported ITIES Tips. 110

5.3.3 SECM Imaging of Single Si_3N_4 Nanopores. 112

5.3.4 Single Nanopore Imaging with Largely Protruded ITIES Nanotips. 115

5.3.5 A Comparison between Hemispherical and Disk Tips 116

5.4 CONCLUSIONS 119

5.5 SUPPORTING INFORMATION 120

5.5.1 Finite Element Simulation. 120

ACKNOWLEDGEMENTS 124

5.6 REFERENCES 125

6.0 CONCLUSIONS 128

LIST OF TABLES

Table 2-1. Parameters from Nanogap Voltammograms at PMMA-Supported Graphene. 21

Table 2-2. Parameters from Nanogap Voltammograms at PS-Supported Graphene. 21

Table 3-1. Parameters Determined from Asymmetric and Symmetric Pairs of Nanogap Voltammograms. 48

LIST OF FIGURES

Figure 2-1. Nanogap voltammetry of the (A) oxidation and (B) reduction of the FcMeOH couple at a graphene electrode..... 8

Figure 2-2. Nanogap voltammograms of 0.5 mM FcMeOH at a PMMA-supported graphene electrode in 1 M KCl (solid lines). The tip current in the top and bottom panels is based on the SG/TC and feedback modes, respectively. Dotted lines are theoretical curves with a = 0.49 µm, r_g/a = 2.1, and the parameters in Table 2-1. Dashed lines are reversible. 10

Figure 2-3. Double-layer effects on (A) oxidation and (B) reduction of the FcMeOH couple at PMMA-supported graphene electrodes. 11

Figure 2-4. Nanogap voltammograms of 0.5 mM FcMeOH at PS-supported graphene in 1 M KCl (solid lines). The tip current in the top and bottom panels is based on the SG/TC and feedback mode, respectively. Dotted lines are the reversible voltammograms calculated with a = 0.49 µm, r_g/a = 1.7, and the parameters in Table 2-2. 12

Figure 2-5. CVs of 0.5 mM FcMeOH at (A) PMMA- and (B) PS-supported graphene electrodes in 1 M KCl. The potential was defined against the formal potential of the FcMeOH couple ….. 16

Figure 2-6. An SECM feedback approach curve with 0.5 mM FcMeOH at an unbiased gold substrate in 1 M KCl (circles). The tip potential was set to 0.35 V against Ag/AgCl, respectively. Probe scan rate, 19 nm/s. The positive feedback curve (red) was obtained theoretically[25] for a = 0.47 µm and r_g/a = 2.0.. 18

Figure 2-7. SECM feedback approach curves with 0.5 mM FcMeOH at (A) PMMA- and (B) PS-supported graphene electrode in 1 M KCl (circles). The potentials of tip and graphene electrodes

were set to 0.4 and 0 V against Ag/AgCl, respectively. Probe scan rate, 49 nm/s. Theoretical curves[25] are limited by diffusion (red line) or electron transfer (black line) with a rate constant of (A) 1.4 and (B) 1.2 cm/s and are given for a = 0.49 μm and r_g/a = (A) 2.1 and (B) 1.7..... 20

Figure 2-8. A comparison of theoretical nanogap voltammograms (red, magenta, green, and blue lines) with the experimental nanogap voltammogram of FcMeOH oxidation at PS-supported graphene at the shortest tip–substrate distance of 31 nm (black line).... 23

Figure 2-9. Nanogap voltammograms of 0.5 mM FcMeOH at a PS-supported graphene electrode in 1 M KCl (solid lines). Dots represent reversible voltammograms ($\lambda' \geq 10$) calculated with a = 0.49 μm, r_g/a = 1.7, and parameters in Table 2-2..... 24

Figure 2-10. CVs of 1 mM $Fe(CN)_6^{4-}$ at (A) PS- and (B) PMMA-supported graphene electrodes in 1 M KCl. The potential was scanned at 0.1 V/s and defined against the formal potential of the $Fe(CN)_6^{4-/3-}$ couple. Simulated voltammograms employed k^0 = (A) 1.4×10^{-4} and (B) 1.7×10^{-3} cm/s in addition to $\alpha = 0.5$..... 26

Figure 3-1. Scheme of SECM-based nanogap voltammetry in (A) SG/TC and (B) feedback modes at the airborne-contaminated HOPG surface. Fc^+ and Fc^{2+} represent (ferrocenylmethyl)trimethylammonium and its oxidized form, respectively..... 33

Figure 3-2. Simulated nanogap voltammograms with (black) and without (red) Fc^+ adsorption on the HOPG surface at d/a = 0.1. Solid and dashed lines represent forward and reverse waves, respectively, which overlap with each other without Fc^+ adsorption (red).... 39

Figure 3-3. Simulated nanogap voltammograms with (black) and without (red) Fc^{2+} adsorption on the glass sheath of a tip at d/a = 0.1. Solid and dashed lines represent forward and reverse waves, respectively, which overlap with each other without Fc^+ adsorption (red).... 42

Figure 3-4. Asymmetric pairs of nanogap voltammograms of 0.3 mM Fc^+ at the non-protected HOPG surface in 50 mM KCl. Forward and reverse waves are represented by solid and dashed lines. Dots represent reversible voltammograms without any adsorption effect (eqs 56 and 57 with $E^{0'}$ = 0.340 V, *a* = 506 nm, *RG* = 2.0, and parameters listed in Table 3-1).... 46

Figure 3-5. Symmetric nanogap voltammograms of 0.3 mM Fc^+ at the water-protected HOPG surface in 50 mM KCl. Forward and reverse waves are represented by solid and dashed lines. Dots represent reversible voltammograms without any adsorption effect (eqs 56 and 57) and fit with reverse waves to yield $E^{0'}$ = 0.340 V, *a* = 490 nm, *RG* = 1.9, and parameters listed in Table 3-1.... 49

Figure 3-6. (A) CVs of 0.3 mM Fc^+ at the water-protected HOPG surface in 50 mM KCl. Potential sweep rates are 0.1, 0.5, 1, 2, 3, 4, 5, 6, 7, 8, 9, and 10 V/s. The inset shows forward waves of experimental (solid) and simulated (dashed) CVs at 10 V/s. (B) Nanogap voltammograms simulated with weak Fc^+ adsorption on the HOPG surface at various *d* values and other parameters as determined from Figure 3-4. Solid and dashed lines represent forward and reverse waves, respectively.... 52

Figure 3-7. (A) Scheme of the SECM configuration employed in this study at d = a. Red boundaries show no normal flux. The blue boundary represents the bulk solution. Part (B) represents the region of part (A) surrounded by the dashed box.. 58

Figure 3-8. A symmetric pair of nanogap voltammograms of 0.3 mM Fc^+ in 50 mM KCl when a Pt tip was positioned just at the outside of the feedback distance from the non-protected HOPG surface. Forward and reverse waves are represented by solid and dashed lines, respectively.....64

Figure 3-9. Nanogap voltammograms of 0.3 mM Fc^+ in 50 mM KCl at the water-protected HOPG surface as measured in the SG/TC mode before and after a nanogap voltammogram was

measured in the feedback mode. Forward and reverse waves are represented by solid and dashed lines, respectively..... 65

Figure 3-10. (A) Experimental and simulated CVs of 0.3 mM Fc^+ in 50 mM KCl with water-protected HOPG. Potential sweep rate, 0.1 V/s. (B) The forward wave of an experimental CV at 10 V/s after the subtraction of a simulated CV. See the inset of Figure 3-6A for forward waves of original experimental and simulated CVs..... 68

Figure 3-11. A plot of Δi_p versus v (open circles) from CVs of 0.3 mM Fc^+ at the water-protected HOPG surface in 50 mM KCl and a theoretical fit (solid line).... 69

Figure 4-1. (A) Scheme of redox reactions at the tip and the conductive outer wall as defined in the cylindrical coordinate for simulation of SECM approach curves. (B) Approach curves simulated for a disk-shaped tip with a conductive and insulating outer wall ($\theta = 5^\circ$ and RG = 1.4). The tip current was normalized against different $i_{T,\infty}$ values for a conductive and insulating outer wall (see eq 4)..... 82

Figure 4-2. TEM images of carbon nanotips (A) before and (B) after FIB milling. Scale bar, 100 nm 86

Figure 4-3. SEM images of (A) unmilled and (B) FIB-milled carbon nanotips and the corresponding FIB images in parts C and D, respectively. Scale bars: 200 nm in parts A and B, and 500 nm in parts C and D 87

Figure 4-4. CVs (circles) of 1 mM $Ru(NH_3)_6Cl_3$ in PBS at (A) 49 and (B) 29 nm-radius tips of FIB-milled CVD carbon nanoelectrodes. Solid and dashed lines represent simulated CVs 88

Figure 4-5. Approach curves of SiO_2-coated silicon wafers as obtained by using FIB-milled carbon nanotips with a = (A) 119, (B) 44, and 27 nm in PBS of 1 mM $Ru(NH_3)_6Cl_3$. Solid and dashed lines represent simulated curves 91

Figure 4-6. Approach curves at gold-coated silicon wafers as obtained with (A) 5.0, (B) 1.0, and (C) 0.2 mM $Ru(NH_3)_6Cl_3$ in PBS by using FIB-milled carbon nanotips with a = 134, 123, and 139 nm, respectively. Solid and dashed lines represent theoretical curves from ref. 50 94

Figure 4-7. SEM images of (A) unmilled and (B) FIB-milled carbon nanotips with ESD damage. The latter tip was used for CV measurements in the bulk solution before SEM imaging. Scale bars: (A) 500 nm and (B) 200 nm 96

Figure 5-1. (A) An SECM cell with a nanoporous Si_3N_4 membrane and a DCE-filled nanopipet tip. (B) Constant-height SECM imaging of single Si_3N_4 nanopores 105

Figure 5-2. TEM images of a quartz nanopipet at (A) ×50,000, (B) ×100,000, and (C) ×200,000 as well as another nanopipet at (D) ×120,000..... 109

Figure 5-3. TEM images of nanopipets deformed by the electron beam at (A) ×80,000 and (B) ×100,000 110

Figure 5-4. TEM images of a nanoporous Si_3N_4 membrane at (A) ×12,000 and (B) ×60,000..... 112

Figure 5-5. (A) A 300 nm × 600 nm SECM image of single Si_3N_4 nanopores as obtained with a sphere-cap nanopipet tip in 1 M KCl containing 5 mM TBACl. Cross sections (circles) as indicated by black lines in Part (A) along (B) x and (C) y directions. Red circles indicate the experimental data points that broaden the nanopore image. Solid lines represent simulation results with a = 15 nm, r_g = 21 nm, h = 2.7 nm, and d = 14.25 nm. Dashed lines locate the edges of a 100 nm-diameter pore..... 114

Figure 5-6. (A) A 300 nm × 600 nm SECM image of single Si_3N_4 nanopores as obtained with a sphere-cap nanopipet tip in 1 M KCl containing 5 mM TBACl. Cross sections (circles) as indicated by black lines in Part (A) along (B) x and (C) y directions. Red circles indicate the

experimental data points that broaden the nanopore image. Solid lines represent simulation results with a = 15 nm, r_g = 21 nm, h = 12.1 nm, and d = 16.8 nm. Dashed lines locate the edges of a 100 nm-diameter pore 116

Figure 5-7. Finite element simulation of SECM line scans with disk and hemispherical tips over (A) single nanopore with a radius of 3a (dotted lines) and a length of 6a and (B) single conductive nanodisk with a radius of 3a (dotted lines). The lateral tip position was normalized against the tip radius, a 118

Figure 5-8. Scheme for the finite element simulation of SECM diffusion problems with a sphere-cap (or disk) tip positioned over (A) a nanopore and (B) a conductive nanodisk. Black boundaries are insulating, blue boundaries are simulation limits or a conductive substrate surface, and red boundaries are tip surfaces 121

LIST OF SCHEMES

Scheme 2-1. Scheme of fabrication of a polymer-supported graphene electrode; (1) drop cast of a polymer film, (2) attachment of polymer-supported graphene (15 mm × 15 mm) to polydimethylsiloxane (PDMS) support, (3) etching of the Cu foil, (4) and insulation of exposed Cu edges (2–3 mm in length). 7

ACKNOWLEDGEMENTS

First, I would like to sincerely thank Professor Shigeru Amemiya for all his guidance and support during my graduate research. I have learned a lot from his knowledge and passion for scientific research. I have gained a valuable experience from these years in his group.

I would like to thank Professor Stephen Weber, Professor Adrian Michael and Professor Xinyan Cui for serving on my committee and for their help and advices during my graduate program.

I would like to thank Professor Jiyeon Kim and Professor Mei Shen for helpful discussions and supports during my research. And I wish to thank all the current and former members of the Amemiya group for their help: Dr. Pavithra Pathirathna, Ryan Balla, Niraja Kurapati, Guanqun Meng, Erin Gramm, Dr. Nikoloz Nioradze, Dr. Alex Lima and Dr. Benjamin Kabagambe.

I also wish to thank the following groups for their help with different samples and research collaboration: Professor Haitao Liu group (graphene samples) and Professor Michael Mirkin group (carbon nanotips).

I wish to thank the following individuals for their support with different instruments for my research: Mr. Tom Gasmire, Mr. Jeff Sicher, Mr. Shawn Artman and Mr. Jeff Tomaszewski (Machine shop), Ms. Lori Neu (Glass shop), Mr. Dave Emala, Mr. Chuck Fleishaker and Mr. George Zuk (Electronics shop), Dr. Susheng Tan and Mr. Mike McDonald (NFCF).

Lastly, I would like to thank my family for their support and love. And I would like to thank my friends Zhe Ren, Zhenlv Han and Zherui Guo for their help and friendship.

1.0 INTRODUCTION

One aim of my PhD work is to study the electrochemical reactivity of various carbon nanomaterials using nanogap voltammetry based on scanning electrochemical microscopy (SECM). And another aim is to reliably fabricate and characterize nanoelectrodes for SECM.

The understanding of the electrochemical reactivity of carbon nanomaterials is of great importance not only for the application purposes, but also for fundamental electrochemistry. There are controversies about how the electronical reactivity of these materials depend on the electronic structures, defects and contamination. To address this issue, I applied the nanogap voltammetry based on nanoscale scanning electrochemical microscopy (SECM) to study the electron-transfer (ET) kinetics at graphene surface and highly pyrolytic graphite (HOPG) surface. On the other hand, SECM at nanometer scale is a powerful technique, with unique advantages and unprecedented measurement capabilities, such as very high spatial resolution for surface imaging. However, it has been challenging to reliably characterize the size and geometry of the nanometer-size electrodes. To address this issue, I developed methods to fabricate and quantitatively characterize the size and geometry of carbon nanoelectrodes and nanopipets.

In the second chapter, I report the heterogeneous ET kinetics at chemical vapor deposition grown graphene determined by nanogap voltammetry based on SECM.[1] More specifically, I demonstrate that the conventional use of poly(methylmethacrylate) (PMMA) for graphene transfer from a growth substrate to the electrode support causes slow and abnormal ET kinetics. By

applying the nanogap voltammetry based on SECM, the ET kinetics on the graphene electrode supported by either polystyrene or PMMA is obtained. When the graphene electrode is supported by polystyrene, unprecedentedly high standard ET rate constants ≥25 cm/s for ferrocenemethanol is obtained, which are ≥10 times higher than those obtained on graphene electrodes supported by PMMA, and at least 2–3 magnitude higher than those reported in literature on PMMA-transferred graphene electrodes.

In the third chapter, I show the application of nanogap voltammetry for the measurement of ultrafast ET kinetics on HOPG.[2] I demonstrate the advantage of this technique to assess the cleanness of the substrate surface in solution by confirming that the airborne contamination of HOPG causes the non-ideal asymmetry of paired nanogap voltammograms in (ferrocenylmethyl)trimethylammonium (Fc^+). Symmetric pairs of nanogap voltammograms are obtained on a cleaner HOPG surface that is exfoliated in humidified air and covered with a nanometer-thick water layer to suppress airborne contamination. This result disapproves the misconception that the asymmetry of such nanogap voltammograms results from the electron exchange mediated by Fc^{2+} adsorbed on the glass sheath of the nanoelectrode. Significantly, by applying nanogap voltammetry, we estimate extremely high standard ET rate constant ≥12 cm/s for the outer-sphere ET reaction of $Fc^{+/2+}$ at water-protected HOPG.

In the fourth chapter, I develop carbon nanoprobes with high electrochemical reactivity and well-controlled size and geometry based on chemical vapor deposition of carbon in quartz nanopipets.[3] The carbon-filled nanopipets are milled by focused ion beam to yield flat disk tips with a thin quartz sheath which is confirmed by transmission electron microscopy. The high electroreactivity of the carbon nanotips are confirmed by cyclic voltammetry in $Ru(NH_3)_6^{3+}$ which shows a high standard ET rate constant ≥10 cm/s. The tip size and geometry are characterized by

SECM approach curves. Carbon nanotips with inner and outer tip radii of down to ~27 and ~38 nm are fabricated and characterized this way. Importantly, carbon nanotips must be protected from electrostatic damage to provide reliable nanoelectrochemical measurements.

In the fifth chapter, I apply the SECM imaging on 100 nm diameter Si_3N_4 nanopores with nanopipet-supported interfaces between two immiscible electrolyte solutions (ITIES).[4] The size and geometry of the nanopipets are characterized by transmission electron microscopy. The nanopipets have an extremely small tip diameter of ~30 nm with a substantial tip roughness of ~5 nm. The ITIES interface supported by a rough nanopipet can form a sphere-cap geometry, and give higher tip current response than that with a disk-shape geometry. In the SECM imaging of 100 nm diameter Si_3N_4 nanopores, the spatial resolution or image contrast is not compromised by a sphere-cap tip, which is also confirmed by finite element simulation. These findings can augment the utility of protruded nanotips that can be more readily fabricated to facilitate nanoscale SECM imaging.

1.1 REFERENCES

(1) Chen, R.; Nioradze, N.; Santhosh, P.; Li, Z.; Surwade, S. P.; Shenoy, G. J.; Parobek, D. G.; Kim, Mi. A.; Liu, H.; Amemiya, S. *Angwe. Chem., Int. Ed.* **2015**, *54*, 15134-15137.

(2) Chen, R.; Balla, R. J.; Li, Z.; Liu, H.; Amemiya, S. *Anal. Chem.* **2016**, *88*, 8323-8331.

(3) Chen. R.; Hu, K.; Yu, Y.; Mirkin, M. V.; Amemiya, S. *J. Electrochem. Soc.* **2016**, *163*, H3032-H3037.

(4) Chen, R.; Balla, R. J.; Lima, A. S.; Amemiya, S. *Anal. Chem.* Accepted.

2.0 ULTRAFAST ELECTRON TRANSFER KINETICS OF GRAPHENE GROWN BY CHEMICAL VAPOR DEPOSITION

This work has been published as Chen, R.; Nioradze, N.; Santhosh, P.; Li, Z.; Surwade, S. P.; Shenoy, G. J.; Parobek, D. G.; Kim, Mi. A.; Liu, H.; Amemiya, S. Ultrafast Electron Transfer Kinetics of Graphene Grown by Chemical Vapor Deposition, *Angwe. Chem., Int. Ed.* **2015**, *54*, 15134-15137. The thesis author fabricated electrodes, collected and analyzed experimental data.

2.1 INTRODUCTION

Graphene grown by chemical vapor deposition[1] (CVD) is a promising electrode material for various electrochemical applications. The potential applications of CVD-grown graphene in energy conversion and storage are broad, including fuel cells, batteries, supercapacitors, and solar cells.[2] CVD-grown graphene is also important for electrochemical sensing.[3] The promise of CVD-grown graphene for these electrochemical applications lies in its large area, excellent electrical conductivity, high surface-to-mass ratio, superb transparency, and mechanical robustness and flexibility. In addition, many of these applications require fast electron transfer (ET) between graphene and redox species in a solution. It, however, is not fundamentally understood how heterogeneous ET kinetics at graphene/solution interfaces is affected by electronic structure, defects, and impurities.[4]

Currently, the electrochemical reactivity of CVD-grown graphene is considered low by comparison with other sp^2 hybridized carbon materials. Electrodes based on CVD-grown monolayer graphene yielded standard ET rate constants, k^0, in a range of 0.01–0.04 cm/s for ferrocenemethanol (FcMeOH)[5] and 0.04–0.2 cm/s for (ferrocenylmethyl)trimethylammonium ($FcTMA^+$).[6] These k^0 values for ferrocene-based simple redox couples are 2–3 orders of magnitude lower than those for $FcTMA^+$ at single-walled carbon nanotubes (7.6 cm/s)[7] and highly oriented pyrolytic graphite (HOPG; ≥17 cm/s).[8] Moreover, ET rates at CVD-grown graphene electrodes depended very weakly on the electrode potential to yield anomalously small (<0.1) or large (>0.9) transfer coefficients, α, for the reduction or oxidation, respectively, of various redox couples.[5b] By contrast, a normal α value of ~0.5 was reported for mechanically exfoliated graphene.[9]

Herein, we demonstrate that the electrochemical reactivity of CVD-grown graphene can be increased at least 2–3 orders of magnitude than that reported in the literature[5] simply by avoiding the conventional use of poly(methyl methacrylate) (PMMA) for electrode fabrication. PMMA has been used almost exclusively to transfer graphene from a metallic growth substrate to a target substrate.[1] During electrode fabrication based on PMMA-mediated transfer, a PMMA film is spread over graphene and is dissolved using organic solvents[5-6] to inevitably leave PMMA residues on the graphene surface.[10] In this work, we assess the effects of PMMA on the electrochemical reactivity of CVD-grown graphene by using polymer-supported electrodes (Scheme 2-1). With this setup, the graphene surface that is exposed to redox species is never coated with a PMMA film. In addition, a PMMA-free graphene electrode can be fabricated by using polystyrene (PS) support. Macroscopic electrodes based on PMMA- and PS-supported graphene yielded reversible cyclic voltammograms (CVs) of the FcMeOH couple at potential sweep rates of up to 0.8 V/s (Figure 2-5). The corresponding k^0 values of ≥0.4 cm/s for the FcMeOH couple

were at least 10–40 times higher than the k^0 values at PMMA-transferred graphene electrodes,[5] which were passivated by PMMA residues.

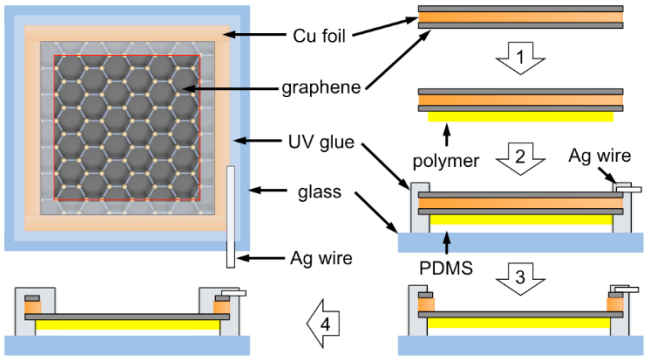

Scheme 2-1. Scheme of fabrication of a polymer-supported graphene electrode; (1) drop cast of a polymer film, (2) attachment of polymer-supported graphene (15 mm × 15 mm) to polydimethylsiloxane (PDMS) support, (3) etching of the Cu foil, (4) and insulation of exposed Cu edges (2–3 mm in length).

We employed scanning electrochemical microscopy[11] (SECM) to demonstrate the ultrafast ET kinetics of the FcMeOH couple at polymer-supported graphene electrodes. Specifically, SECM-based nanogap voltammetry[8, 12] was used to investigate both oxidation and reduction of the FcMeOH couple under extremely high mass-transport conditions. In nanogap voltammetry (Figure 2-1), an ultramicroelectrode with a Pt tip radius, a, of ~0.5 μm and a surrounding glass radius, r_g, of ~2a[12-13] was positioned over the graphene surface to form 30–450 nm-wide nanogaps (Figure 2-1). The FcMeOH oxidation was voltammetrically driven at the graphene electrode by cycling the electrode potential and was monitored by detecting $FcMeOH^+$ at a diffusion-limited rate at the Pt tip in the substrate-generation/tip-collection (SG/TC) mode (Figure 2-1A). In addition,

$FcMeOH^+$ was generated and monitored at a diffusion-limited rate at the tip in order to study the $FcMeOH^+$ reduction at the graphene electrode in the feedback mode (Figure 2-1B).

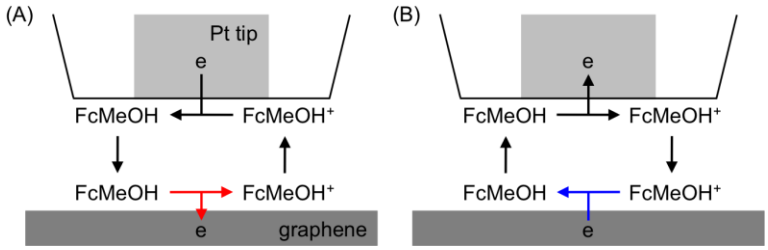

Figure 2-1. Nanogap voltammetry of the (A) oxidation and (B) reduction of the FcMeOH couple at a graphene electrode.

2.2 EXPERIMENTAL SECTION

Monolayer graphene was grown on a copper foil by the CVD method.[14] Graphene was coated with a polymer film by drop-casting a chlorobenzene solution of 46 mg/mL PMMA or 50 mg/mL PS. The polymer/graphene/copper/graphene composite was placed over a PDMS support and attached to a glass plate using UV-cure glue. The copper foil was etched in 0.2 M ammonium persulfate for 1.5–2 hours or in 1 M $FeCl_3$ in 10 % HCl for 40 min to yield polymer-supported graphene. The exposed edges of the copper foil were quickly insulated using UV-cure glue to minimize the airborne contamination of the graphene surface. The insulated graphene electrode was immersed immediately into the solution for CV and SECM characterization, which was

prepared with ultrapure water with extremely low concentrations of organic impurities (total organic carbon (TOC) of ≤1 ppb).

2.3 RESULTS AND DISCUSSION

Figure 2-2 shows nanogap voltammograms of the FcMeOH couple at PMMA-supported graphene electrodes (solid lines). The tip current was normalized against that in the bulk solution, $i_{T,\infty}$ (Equation 3). The graphene potential was defined against the formal potential of the FcMeOH couple. Each pair of voltammograms shown in an identical color was obtained at an identical tip–graphene distance, *d*, without significant thermal drift in tip position.[15] Each voltammogram was sigmoidal and retractable during a potential cycle as a result of the quasi-steady-state diffusion of redox species across a tip–graphene nanogap.[12]

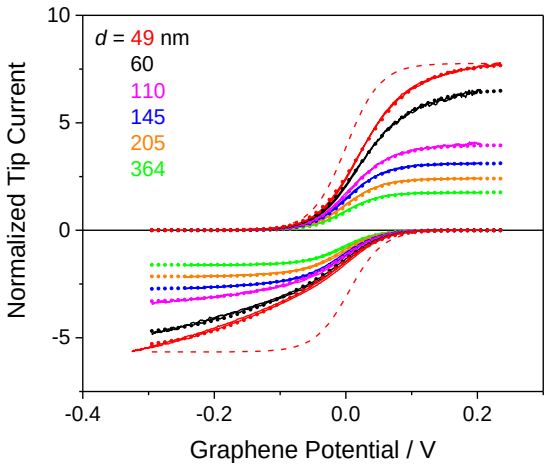

Figure 2-2. Nanogap voltammograms of 0.5 mM FcMeOH at a PMMA-supported graphene electrode in 1 M KCl (solid lines). The tip current in the top and bottom panels is based on the SG/TC and feedback modes, respectively. Dotted lines are theoretical curves with a = 0.49 μm, r_g/a = 2.1, and the parameters in Table 2-1. Dashed lines are reversible.

Nanogap voltammograms of FcMeOH oxidation at PMMA-supported graphene electrodes (the top half of Figure 2-2) were controlled by heterogeneous ET kinetics. These voltammograms were broader than expected for reversible voltammograms that were limited by the diffusion of FcMeOH across a tip–graphene nanogap (e.g., the dashed line at d = 49 nm). All voltammograms of FcMeOH oxidation at PMMA-supported graphene electrodes fit very well with theoretical voltammograms with a normal α value of 0.50 (dotted lines) to yield consistent k^0 values in a range of 1.0–2.1 cm/s at various tip–graphene distances (Table 2-1). Overall, k^0 = 1.6 ± 0.5 cm/s and α = 0.5 were obtained at various vertical and lateral tip positions (N = 37) above six PMMA-supported graphene electrodes. These k^0 values are 25–100 times higher than those at PMMA-transferred graphene electrodes,[5] which were passivated by PMMA residues.

Anomalously, nanogap voltammograms of $FcMeOH^+$ reduction at PMMA-supported graphene electrodes (the bottom half of Figure 2-2) were much broader than the kinetically limited voltammograms of FcMeOH oxidation with a normal α value of 0.5 when tip–graphene distances were short (i.e., 49–110 nm). The feedback tip current did not reach a diffusion-limited value even at very negative potentials. Good fits of experimental voltammograms with theoretical voltammograms yielded significantly low α and k^0 values of 0.29 ± 0.3 and 0.5 ± 0.2 cm/s (N = 23), respectively. We ascribe this weak potential dependence to a double-layer effect from the positive surface charges of the PMMA surface based on the oxidative removal of cryptoelectrons

by the graphene electrode. Liu and Bard reported that cryptoelectrons of the PMMA surface can be readily removed at much more negative potentials than the formal potential of the FcMeOH couple to reduce redox species in the solution.[16] With our setup, positive charges of the underlying PMMA surface do not affect the access of electrically neutral FcMeOH to graphene (Figure 2-3A), thereby yielding an α value of 0.50 for its oxidation. By contrast, the access of positively charged $FcMeOH^+$ to graphene is hampered by the positive surface charges of PMMA (Figure 2-3B). Consequently, $FcMeOH^+$ reduction at PMMA-supported graphene electrodes requires a more negative potential, thus yielding a smaller α value of ~0.3.

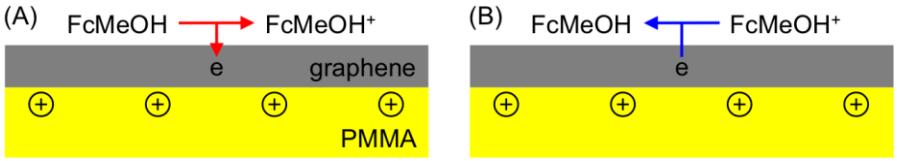

Figure 2-3. Double-layer effects on (A) oxidation and (B) reduction of the FcMeOH couple at PMMA-supported graphene electrodes.

We employed SECM-based nanogap voltammetry to find that ET kinetics at PMMA-free, PS-supported graphene electrodes are unprecedentedly fast. Reversible nanogap voltammograms (e.g., Figure 2-4) were obtained at PS-supported graphene (N = 32 for three electrodes) to yield extremely high k^0 values of up to ≥25 cm/s as the tip approached down to 31 nm from the graphene surface (Table 2-2 and Figure 2-8). These k^0 values are similar to the k^0 values of ≥17 cm/s for $FcTMA^+$ at HOPG.[8] This similarity suggests that the electrochemical reactivity of graphene as the top layer of HOPG is very different from that of graphene on a polar and positively charged PMMA support and is more analogous to that of graphene on a non-polar and neutral PS support. Noticeably, cryptoelectrons were not removable from the surface of PS nanospheres around the formal potential of the FcMeOH couple.[17] Mechanistically, the slower ET kinetics of PMMA-

supported graphene is ascribed to the weakened electronic coupling of graphene with the FcMeOH couple or its hampered reorganization at the interface by the positive charges and dipoles of the PMMA surface. Interestingly, k^0 values for the FcMeOH couple at PS-supported graphene were much higher than the k^0 values of 0.5 ± 0.1 cm/s at PMMA-transferred graphene with high densities of defects,[5c] which were introduced by Ar^+ irradiations to electronically activate graphene. Much higher k^0 values at PS-supported graphene indicate that the electrochemical reactivity of Ar^+-irradiated graphene was limited by PMMA residues.

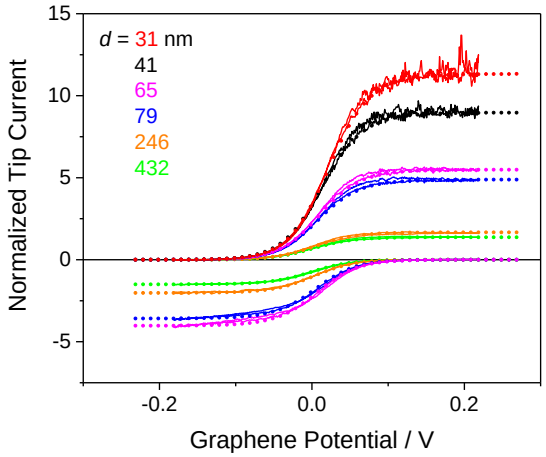

Figure 2-4. Nanogap voltammograms of 0.5 mM FcMeOH at PS-supported graphene in 1 M KCl (solid lines). The tip current in the top and bottom panels is based on the SG/TC and feedback mode, respectively. Dotted lines are the reversible voltammograms calculated with a = 0.49 µm, r_g/a = 1.7, and the parameters in Table 2-2.

Importantly, nanogap voltammograms of $FcMeOH^+$ reduction at PS-supported graphene electrodes quickly reached limiting currents without the feature of weak potential dependence (the bottom half of Figure 2-4). This result supports the notion that PMMA caused an anomalously weak potential dependence of $FcMeOH^+$ reduction in this and in previous[5b] studies. Noticeably,

limiting currents during $FcMeOH^+$ reduction were much lower than those during FcMeOH oxidation at identical tip positions and were nearly unchanged at tip–graphene distances of <50 nm (Figure 2-9). The asymmetric limiting currents are ascribed to the contamination of the graphene surface with airborne hydrocarbons as confirmed by ATR-FTIR.[18]. The hydrophobic contaminant layer is less permeable to the more hydrophilic form of a redox couple.[8] Accordingly, $FcMeOH^+$ reduction at contaminated graphene was more greatly hindered, yielding a lower limiting current. Importantly, hydrophobic FcMeOH can permeate quickly through the hydrophobic contaminant layer to reveal the ultrafast ET kinetics of PS-supported graphene. By contrast, the apparently much slower ET kinetics of the $Fe(CN)_6^{4-/3-}$ couple at polymer-supported graphene was limited by the low permeability of the hydrophobic contaminant layer to this multiply charged hydrophilic redox couple (Figure 2-10).

2.4 CONCLUSIONS

In conclusion, the electrochemical reactivity of PS-supported CVD-grown graphene to the FcMeOH couple is at least 2–3 orders of magnitude higher than that of PMMA-transferred graphene.[5] Remarkably, k^0 values of ≥25 cm/s at PMMA-free graphene exceeded the highest k^0 value reported for the FcMeOH couple so far, which is 6.8 cm/s at Pt nanoelectrodes.[19] The unprecedentedly high electrochemical reactivity of CVD-grown graphene is highly significant both fundamentally and practically. In addition, this work demonstrates the electrochemical transparency of atomically thin graphene, where a supporting material can affect ET kinetics. The hydrophobic airborne contamination of graphene[18] must be prevented to reliably study the

electrochemical reactivity of graphene not only to outer-sphere redox couples,[9, 20] which are typically multiply charges and hydrophilic,[5b] but also to inner-sphere redox couples, which are surface sensitive.[4]

2.5 SUPPORTING INFORMATION

2.5.1 Chemicals and Materials.

FcMeOH (Strem Chemicals, Newburyport, MA, USA) was recrystallized twice from hexane prior to use. $K_4Fe(CN)_6 \cdot 3H_2O$ (≥99.95%), chlorobenzene (anhydrous, 99.8%), PMMA (average molecular weight of ~996,000), and PS (average molecular weight of ~280,000) were obtained from Aldrich (Milwaukee, WI, USA). Copper foils (#46365 and #13382) were from Alfa Aesar (Ward Hill, MA, USA). UV-cure glues (OP420632GEL and OP420632) were obtained from Dymax (Torrington, CT, USA). All sample solutions were prepared by using ultrapure water that contained extremely low concentrations of organic impurities (total organic carbon (TOC) of ≤1 ppb). This ultrapure water was obtained by passing the final product (18.2 MΩ·cm and TOC of 3 ppb) of the Milli-Q Advantage A10 system (EMD Millipore, Billerica, MA, USA) through a specific activated-carbon filter (VOC Pak, EMD Millipore). The Milli-Q system was equipped with a Q-Gard T1 pack and a Quantum TEX cartridge and was fed with the purified tap water (15.0 MΩ·cm) by using the Elix 3 Advantage system (EMD Millipore).

2.5.2 CVs at Polymer-Supported Graphene.

Figure 2-5 shows reversible CVs of FcMeOH at PMMA- and PS-supported graphene electrodes at scan rates, v, of 0.050–0.8 V/s. A reversible CV with a peak separation of ~60 mV is obtained when k^0 satisfies the following conditions [21]

$$\Lambda = \frac{k^0}{\sqrt{DFv/RT}} \geq 15 \qquad (1)$$

where D (= 7.8×10^{-6} cm^2/s) is the diffusion coefficient of FcMeOH. Equation 1 gives $k^0 \geq 0.41$ cm/s for FcMeOH at v = 0.8 V/s. In addition, the area of an exposed graphene surface was estimated from a peak current, i_p, as given by [22]

$$i_p = 0.4463\sqrt{\frac{n^3F^3Dv}{RT}}Ac \qquad (2)$$

where c (= 0.5 mM) is the concentration of FcMeOH in 1 M KCl. CVs in Figures 2-6A and 2-6B give areas of 0.045 and 0.086 cm^2, respectively. Noticeably, neither PMMA- nor PS-supported graphene electrodes showed a voltammetric response based on the surface adsorption of FcMeOH. We speculate that FcMeOH adsorption at PMMA-transferred graphene electrodes was observed voltammetrically [5a] owing to PMMA residues.

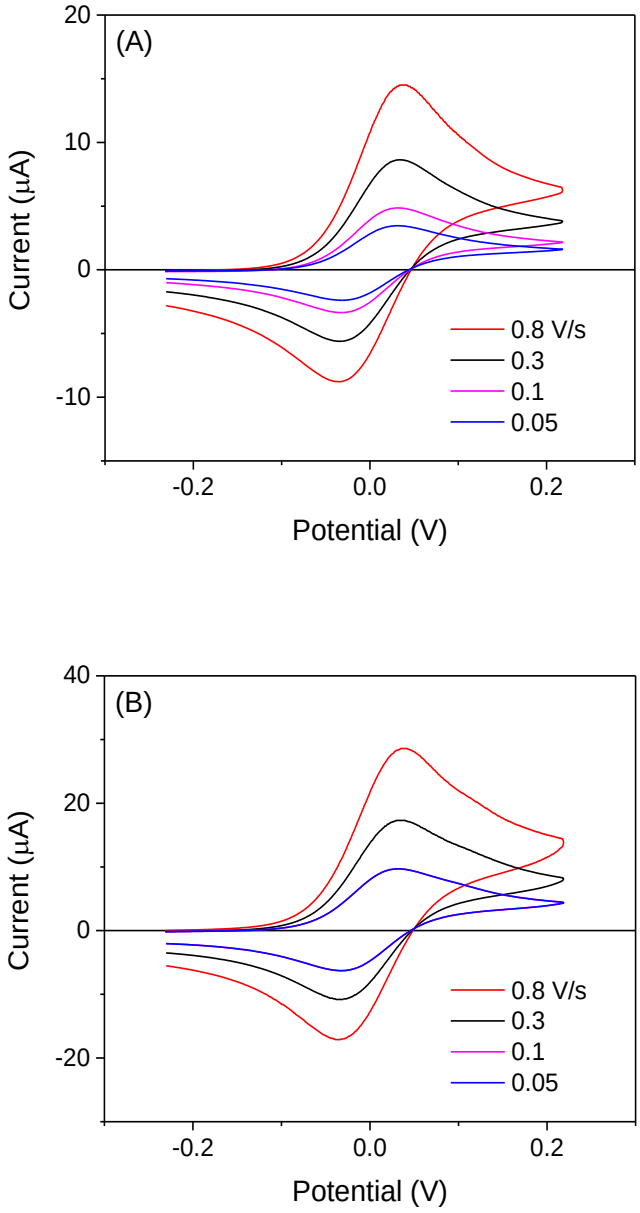

Figure 2-5. CVs of 0.5 mM FcMeOH at (A) PMMA- and (B) PS-supported graphene electrodes in 1 M KCl. The potential was defined against the formal potential of the FcMeOH couple.

2.5.3 SECM Characterization of Pt Tips.

SECM approach curves at a conductive substrate were measured to demonstrate the flat geometry of ~1 μm-diameter Pt tips used in this study. The Pt tips were fabricated by using focused-ion-beam (FIB) milling as reported elsewhere.[12,15] The radii of an FIB-milled Pt tip and its glass sheath were determined by scanning electron microscopy and were consistent with the tip current in the bulk solution, $i_{T,\infty}$, as given by

$$i_{T,\infty} = 4xnFDca \quad (3)$$

where x is a function of a/r_g,[23,24] and n (= 1) is the number of transferred electrons in the tip reaction. Pt and Ag/AgCl wires were used as counter and reference electrodes, respectively. An SECM cell was sealed using a rubber cap and silicon gaskets[8] to prevent the temperature change caused by the evaporation of water from the electrolyte solution and, subsequently, the thermal drift of the tip position[13] as well as the contamination of the electrolyte solution with airborne organic impurities.[8] The glass and Teflon components of the SECM cell were cleaned in piranha solution (a 1:3 mixture of 30% H_2O_2 and 95.0–98.0% H_2SO_4) for 90 minutes and in Milli-Q water for 15 minutes (3 times), and dried in air for 5 minutes (Caution: piranha solution reacts violently with organics and should be handled with extreme care!).

The flat tip of FIB-milled Pt probes approached down to ~10 nm from a flat gold substrate. To achieve the extremely short distance of the closet approach, the perpendicular alignment of the tip's axis with respect to the substrate surface was confirmed within ±0.5˚ by using a digital angle gauge. An experimental approach curve fitted well with a theoretical curve based on the diffusion-limited positive feedback effect from a conductive substrate (Figure 2-6). This good fit was obtained down to a distance of ~10 nm for the closest tip–substrate approach, d_c, by using inner and outer tip radii of 0.47 and 0.94 μm, respectively. The extremely small dc value confirms FIB-

milled Pt tips are flat enough to reliably measure <50 nm distances between the tip and the graphene surface for nanogap voltammetry.

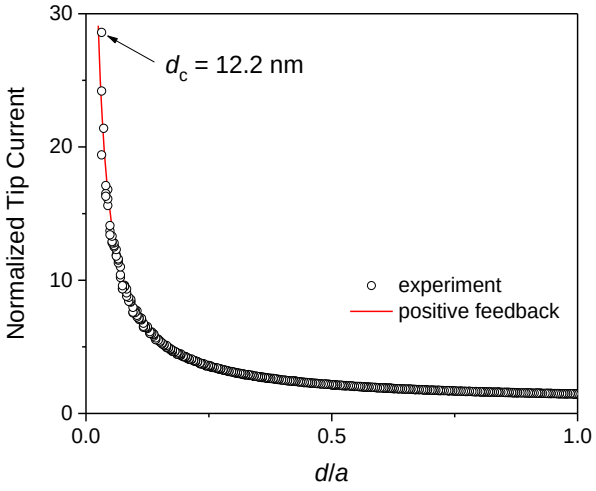

Figure 2-6. An SECM feedback approach curve with 0.5 mM FcMeOH at an unbiased gold substrate in 1 M KCl (circles). The tip potential was set to 0.35 V against Ag/AgCl, respectively. Probe scan rate, 19 nm/s. The positive feedback curve (red) was obtained theoretically[25] for a = 0.47 µm and r_g/a = 2.0.

2.5.4 SECM-Based Nanogap Voltammetry.

A homebuilt SECM instrument was accommodated in an isothermal chamber to enable nanogap voltammetry without the nanoscale thermal drift of the tip position.[13] A tip was positioned at a fixed distance from a polymer-supported graphene electrode by monitoring the feedback tip current during approach curve measurement (e.g., Figure 2-7). The resultant approach curves can be fitted with theoretical curves limited by either FcMeOH diffusion across the tip–graphene gap or $FcMeOH^+$ reduction at the graphene surface[25] by adjusting tip–graphene distances. Moreover, the positive feedback responses to polymer-supported graphene are lower than that to the gold

substrate (Figure 2-6), which is ascribed to the airborne contamination of the graphene surface. Thus, an actual tip–graphene distance was determined by nanogap voltammetry (see below).

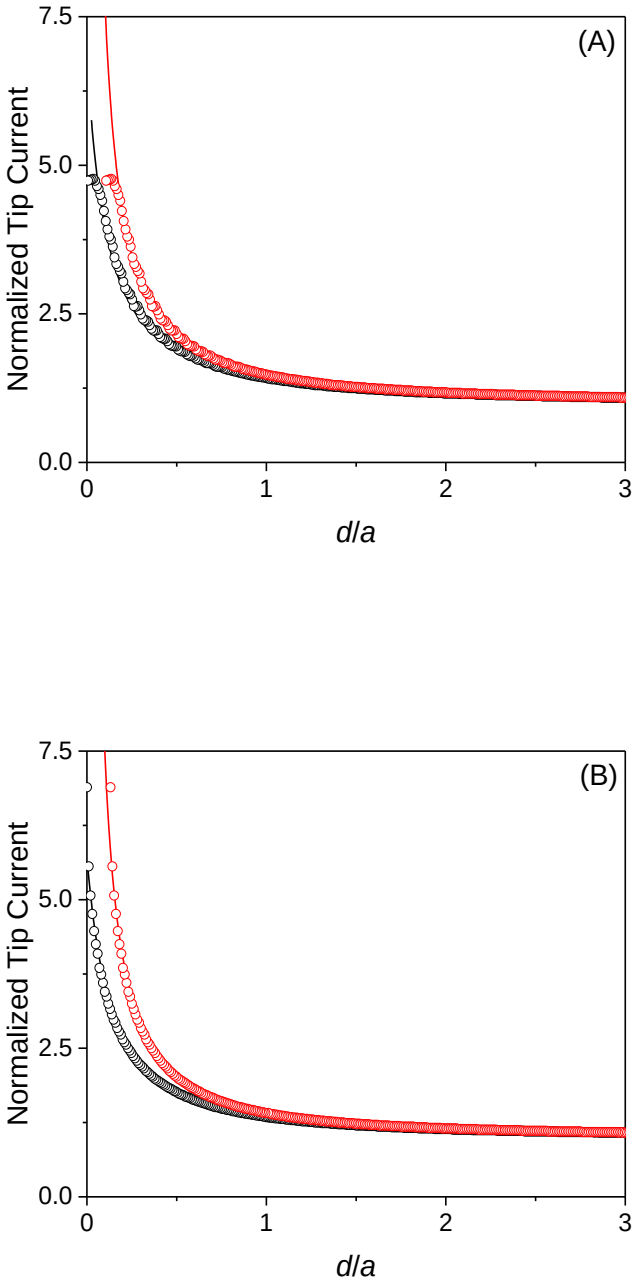

Figure 2-7. SECM feedback approach curves with 0.5 mM FcMeOH at (A) PMMA- and (B) PS-supported graphene electrode in 1 M KCl (circles). The potentials of tip and graphene

electrodes were set to 0.4 and 0 V against Ag/AgCl, respectively. Probe scan rate, 49 nm/s. Theoretical curves[25] are limited by diffusion (red line) or electron transfer (black line) with a rate constant of (A) 1.4 and (B) 1.2 cm/s and are given for a = 0.49 μm and r_g/a = (A) 2.1 and (B) 1.7.

2.5.5 Analysis of Nanogap Voltammograms.

Nanogap voltammograms of the FcMeOH couple at PMMA- and PS-supported graphene electrodes (Figures 2-2 and 2-4, respectively) were analyzed to yield parameters listed in Tables 2-1 and 2-2, respectively. In this analysis, the identical diffusion coefficient of 7.8×10^{-6} cm^2/s was assumed for FcMeOH and FcMeOH$^+$. Nanogap voltammograms of FcMeOH oxidation was fitted to the following equation[12]

$$\frac{i_T}{i_{T,\infty}} = \frac{\pi}{4xL\left(1/\theta_S + \theta_S^{\alpha-1}/\lambda' + 1\right)} + \frac{\theta_S}{\theta_S + 1}\left[\frac{i_T^{PF}}{i_{T,\infty}} - \frac{\pi}{4xL}\right] \quad (4)$$

with

$$q_S = \exp\left[F\left(E_S - E^{0'}\right)/RT\right] \quad (5)$$

$$\lambda = \frac{k^0 d}{D} \quad (6)$$

where $L = d/a$, i_T^{PF} is the corresponding positive feedback current, E_S is the potential of a graphene electrode, and $E^{0'}$ is the formal potential of the FcMeOH couple. Tip–graphene distances were determined from i_T^{PF} values by using the approximate equations given in ref. 25 and are shown in Figures 2-2 and 2-4. Nanogap voltammograms of FcMeOH$^+$ reduction were fitted with the following equation[12]

$$\frac{i_T}{i_{T,\infty}} = \frac{\pi}{4xL\left(\theta_S + \theta_S^{\alpha}/\lambda' + 1\right)} + \frac{1}{\theta_S + 1}\left[\frac{i_T^{PF}}{i_{T,\infty}} - \frac{\pi}{4xL}\right] \quad (7)$$

The tip–graphene distances thus determined were overestimated owing to more serious effects of airborne contamination on $FcMeOH^+$ reduction.

Table 2-1. Parameters from Nanogap Voltammograms at PMMA-Supported Graphene.

Oxidation (SG/TC Mode)			Reduction (Feedback Mode)		
d nm	k^0 cm/s	λ'	d nm	k^0 cm/s	λ'
49	1.6	1.0	69	0.45[a]	0.40
60	1.0	0.8	82	0.43[a]	0.45
110	1.4	2.0	133	0.47[a]	0.80
145	2.1	3.9	180	0.70	1.6
205	1.7	4.5	242	0.55	1.7
364	1.4	6.5	424	0.59	3.2

[a] $\alpha = 0.3$.

Table 2-2. Parameters from Nanogap Voltammograms at PS-Supported Graphene.

Oxidation (SG/TC Mode)		Reduction (Feedback Mode)	
d nm	k^0 cm/s[a]	d nm	k^0 cm/s[a]
31	≥25	—	—
40	≥19	—	—
65	≥12	98	≥7.9
79	≥9.9	115	≥6.8
246	≥3.2	344	≥2.3
432	≥1.8	540	≥1.4

[a] $\lambda' \geq 10$.

Importantly, we confirmed the reliability of kinetic measurements by nanogap voltammetry as follows. We were able to determine kinetic parameters, k^0 and α, without a diffusion limit from nanogap voltammograms at PMMA-supported graphene, where λ' was significantly smaller than 10 (Table 2-1).[12] By contrast, $\lambda' \geq 10$ was used to estimate k^0 values from reversible nanogap voltammograms at PS-supported graphene (Table 2-2).[12] The minimum k^0 value thus estimated was higher at a shorter tip–graphene distance, where a higher mass-transfer condition allowed us to address a higher k^0 value. We verified that $\lambda' \geq 10$ was appropriate to estimate even the highest k^0 value of ≥25 from the reversible nanogap voltammogram based on FcMeOH oxidation at PS-supported graphene. This experimental voltammogram was obtained at the shortest tip–substrate distance of 31 nm (red line in Figure 2-4). The same approach curve (black line in Figure 2-8) was fitted best with the theoretical reversible voltammogram (red line). In addition, the fluctuating tip current was mostly higher than the tip current calculated with λ' = 10 (magenta line) over a range of normalized tip currents of 5–10, thereby yielding $\lambda' \geq 10$. In fact, the experimental voltammogram significantly deviated from theoretical voltammograms with lower λ' values of 5 and 2.5 (green and blue lines, respectively). Noticeably, the lateral conductivity of polymer-supported graphene was high enough to enable reliable kinetic measurements. The k^0 values at PMMA-supported graphene were independent of the concentration of FcMeOH. Moreover, nanogap voltammograms at PS-supported graphene were reversible.

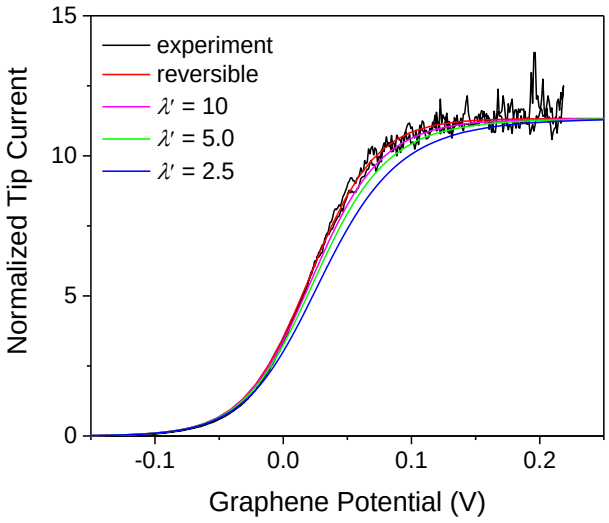

Figure 2-8. A comparison of theoretical nanogap voltammograms (red, magenta, green, and blue lines) with the experimental nanogap voltammogram of FcMeOH oxidation at PS-supported graphene at the shortest tip–substrate distance of 31 nm (black line).

2.5.6 Effects of Airborne Contamination on the FcMeOH Couple.

Nanogap voltammograms of $FcMeOH^+$ reduction at PS-supported graphene gave lower currents than those of FcMeOH oxidation, especially at short tip–graphene distances (Figure 2-9), which we ascribe to the airborne contamination of the graphene surface. Airborne contamination more seriously affects the reduction of more hydrophilic $FcMeOH^+$, the access of which to the underlying graphene surface is blocked more seriously by the hydrophobic contaminant layer.[8] Noticeably, the significant fluctuation of highly enhanced tip currents in Figure 2-9 evidences very short tip–graphene distances and corresponds to a distance change of only ±1 nm. Such small distance fluctuation can be caused by the vibration of the SECM system or the fluctuation of the piezo stage.[13]

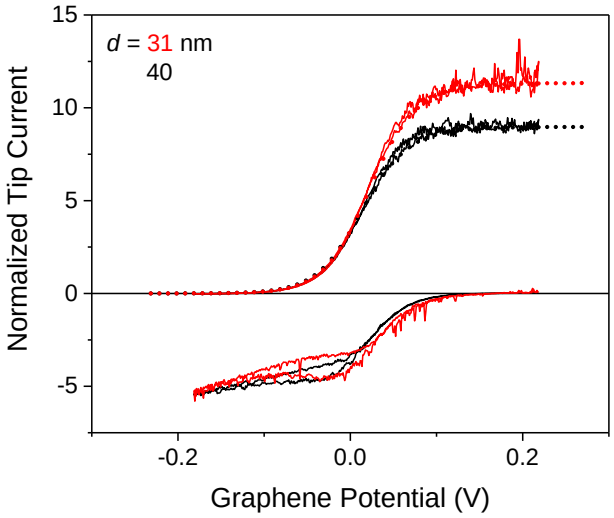

Figure 2-9. Nanogap voltammograms of 0.5 mM FcMeOH at a PS-supported graphene electrode in 1 M KCl (solid lines). Dots represent reversible voltammograms ($\lambda' \geq 10$) calculated with a = 0.49 µm, r_g/a = 1.7, and parameters in Table 2-2.

2.5.7 Effects of Airborne Contamination on the $Fe(CN)_6^{4-/3-}$ Couple.

We studied the CVs of the $Fe(CN)_6^{4-/3-}$ couple at polymer-supported graphene to demonstrate that the ET kinetics of the highly charged hydrophilic redox couple is controlled by the hydrophobic contaminant layer on the graphene surface. The CVs of $Fe(CN)_6^{4-}$ at three PS-supported graphene electrodes (e.g., Figure 2-10A) yielded very wide separations of 0.47 ± 0.07 V between voltammetric peaks, which correspond to low k^0 values of (9 ± 6) × 10^{-5} cm/s. In addition, each voltammetric peak was broader than the peak simulated with α = 0.5. The ET

kinetics of the $Fe(CN)_6^{4-/3-}$ couple at PS-supported graphene is slow and weakly dependent on the potential, because the access of the hydrophilic redox couple to the graphene surface is seriously hindered by hydrophobic airborne contaminants.[14, 18] The CVs of $Fe(CN)_6^{4-}$ at five PMMA-supported graphene electrodes (e.g., Figure 2-10B) gave narrower wide peak separations of 0.16 ± 0.04 V, which correspond to higher k^0 values of (2 ± 1) × 10^{-3} cm/s with a normal α value of 0.5. In comparison with PS-supported graphene, the apparently improved ET kinetics of the $Fe(CN)_6^{4-/3-}$ couple at PMMA-supported graphene is ascribed to the less serious contamination of the latter graphene surface with hydrophobic contaminants. We speculate that the positive surface charges of PMMA render the opposite side of the graphene surface less hydrophobic, thereby reducing the adsorption of hydrophobic contaminants. Moreover, the ET kinetics of the $Fe(CN)_6^{4-/3-}$ couple at PMMA-supported graphene is much faster than that at PMMA-transferred graphene, which yielded much wider peak separations of 1.0–1.2 V[26, 27] or much smaller voltammetric peaks[5b] owing to the contamination of the graphene surface with PMMA residues. The PMMA-supported graphene surface, however, is still significantly contaminated with airborne hydrocarbons during electrode fabrication.[14, 18] Importantly, Dryfe and co-workers reported that airborne contamination significantly compromises the ET kinetics of graphene exfoliated from natural graphite for the $Fe(CN)_6^{4-/3-}$ couple to yield a range of k^0 values between 1.3 × 10^{-4} and 2.1 × 10^{-3} cm/s from a monolayer to a bulk material.[20, 28]

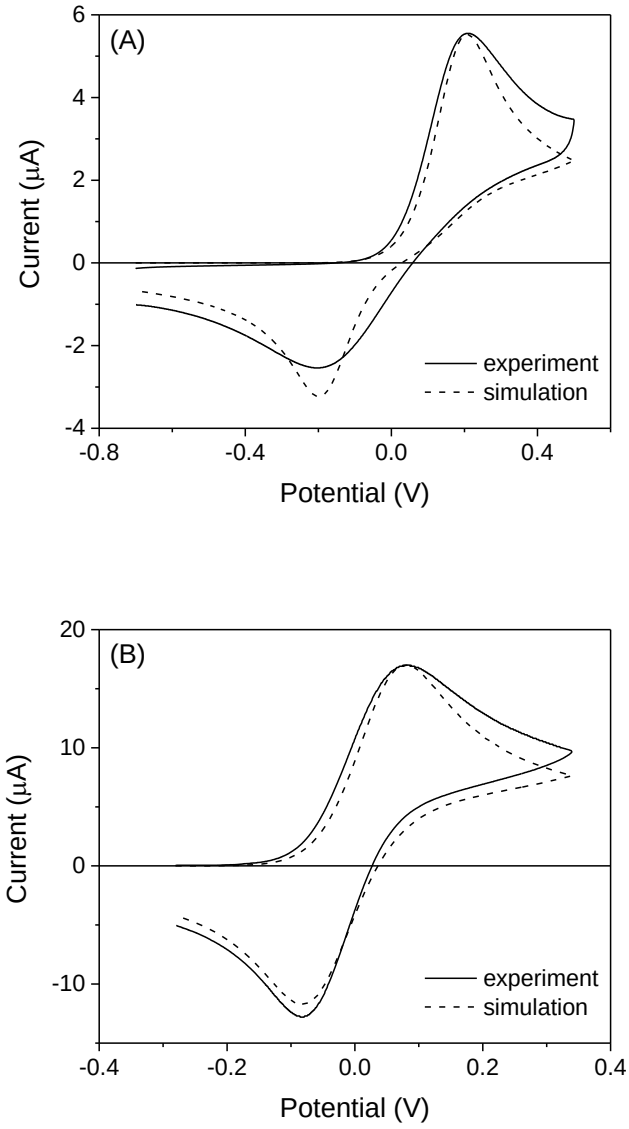

Figure 2-10. CVs of 1 mM $Fe(CN)_6^{4-}$ at (A) PS- and (B) PMMA-supported graphene electrodes in 1 M KCl. The potential was scanned at 0.1 V/s and defined against the formal potential of the $Fe(CN)_6^{4-/3-}$ couple. Simulated voltammograms employed k^0 = (A) 1.4×10^{-4} and (B) 1.7×10^{-3} cm/s in addition to $\alpha = 0.5$.

ACKNOWLEDGEMENTS

This work was supported by the NSF (CHE-1213452 for S.A. and CHE-1507629 for H.L.). H.L. also acknowledges partial support from the ONR (N000141310575) and the AFOSR (FA9550-13-1-0083). We thank Dr. Jiyeon Kim, Dr. Cheng Tian, Prof. Anahita Izadyar, Prof. Mei Shen, Niraja S. Kurapati, and Chaminda P. Gunathilaka for their help.

2.6 REFERENCES

(1) Li, X. S.; Cai, W. W.; An, J. H.; Kim, S.; Nah, J.; Yang, D. X.; Piner, R.; Velamakanni, A.; Jung, I. ; Tutuc, E.; Banerjee, S. K.; Colombo, L.; Ruoff, R. S. *Science* **2009**, *324*, 1312.

(2) Bonaccorso, F.; Colombo, L. ; Yu, G. ; Stoller, M. ; Tozzini, V.; Ferrari, A. C. ; Ruoff, R. S.; Pellegrini, V. *Science* **2015**, *347*, UNSP 1246501.

(3) Yang, W.; Ratinac, K. R.; Ringer, S. P.; Thordarson, P.; Gooding, J. J.; Braet, F. *Angew. Chem. Int. Ed.* **2010**, *49*, 2114;

(4) McCreery, R. L.; McDermott, M. T. *Anal. Chem.* **2012**, *84*, 2602.

(5) a) Li, W.; Tan, C.; Lowe, M. A.; Abruña, H. D.; Ralph, D. C. *ACS Nano* **2011**, *5*, 2264; b) Ritzert, N. L. ; Rodriguez-López, J. ; Tan, C.; Abruña, H. D. *Langmuir* **2013**, *29*, 1683; c) Zhong, J.-H.; Zhang, J.; Jin, X.; Liu, J.-Y.; Li, Q.; Li, M.-H.; Cai, W.; Wu, D.-Y.; Zhan, D.; Ren, B. *J. Am. Chem. Soc.* **2014**, *136*, 16609.

(6) Güell, A. G.; Ebejer, N.; Snowden, M. E.; Macpherson, J. V.; Unwin, P. R.; *J. Am. Chem. Soc.* **2012**, *134*, 7258.

(7) Heller, I.; Kong, J.; Heering, H. A.; Williams, K. A.; Lemay, S. G.; Dekker, C. *Nano Lett.* **2005**, *5*, 137.

(8) Nioradze, N.; Chen, R.; Kurapati, N.; Khvataeva-Domanov, A.; Mabic, S.; Amemiya, S. *Anal. Chem.* **2015**, *87*, 4836.

(9) Velický, M.; Bradley, D. F.; Cooper, A. J.; W. Hill, E.; Kinloch, I. A.; Mishchenko, A.; Novoselov, K. S.; Patten, H. V.; Toth, P. S.; Valota, A. T.; Worrall, S. D.; Dryfe, R. A. W. *ACS Nano* **2014**, *8*, 10089.

(10) Pirkle, A.; Chan, J.; Venugopal, A.; Hinojos, D.; Magnuson, C. W.; McDonnell, S.; Colombo, L.; Vogel, E. M.; Ruoff, R. S.; Wallace, R. M. *Appl. Phys. Lett.* **2011**, *99*, 122108.

(11) Amemiya, S.; Bard, A. J.; Fan, F.-R. F.; Mirkin, M. V.; Unwin, P. R. *Annu. Rev. Anal. Chem.* **2008**, *1*, 95.

(12) Nioradze, N.; Kim, J.; Amemiya, S. *Anal. Chem.* **2011**, *83*, 828.

(13) Kim, J.; Izadyar, A.; Nioradze, N.; Amemiya, S. *J. Am. Chem. Soc.* **2013**, *135*, 2321.

(14) Li, Z.; Wang, Y.; Kozbial, A.; Shenoy, G.; Zhou, F.; McGinley, R.; Ireland, P.; Morganstein, B.; Kunkel, A.; Surwade, S. P.; Li, L.; Liu, H. *Nat. Mater.* **2013**, *12*, 925;

(15) Kim, J.; Shen, M.; Nioradze, N.; Amemiya, S. *Anal. Chem.* **2012**, *84*, 3489.

(16) Liu, C.-Y.; Bard, A. J. *J. Am. Chem. Soc.* **2009**, *131*, 6397.

(17) Varleý, T. S.; Rosillo-Lopez, M.; Sehmi, S.; Hollingsworth, N.; Holt, K. B. *Phys. Chem. Chem. Phys.* **2015**, *17*, 1837.

(18) Kozbial, A.; Li, Z.; Conaway, C.; McGinley, R.; Dhingra, S.; Vahdat, V.; Zhou, F.; D'Urso, B.; Liu, H.; Li, L. *Langmuir* **2014**, *30*, 8598.

(19) Sun, P.; Mirkin, M. V. *Anal. Chem.* **2006**, *78*, 6526.

(20) Velický, M.; Bissett, M. A.; Toth, P. S.; Patten, H. V.; Worrall, S. D.; Rodgers, A. N. J.; Hill, E. W.; Kinloch, I. A.; Novoselov, K. S.; Georgiou, T.; Britnell, L.; Dryfe, R. A. W. *Phys. Chem. Chem. Phys.* **2015**, *17*, 17844.

(21) Bard, A. J.; Faulkner, L. R. *Electrochemical Methods: Fundamentals and Applications*; 2nd ed.; John Wiley & Sons: New York, 2001, p. 239.

(22) Bard, A. J.; Faulkner, L. R. *Electrochemical Methods: Fundamentals and Applications*; 2nd ed.; John Wiley & Sons: New York, 2001, p. 231.

(23) Shoup, D.; Szabo, A. *J. Electroanal. Chem.* **1984**, *160*, 27.

(24) Cornut, R.; Lefrou, C. *J. Electroanal. Chem.* **2007**, *604*, 91.

(25) Cornut, R.; Lefrou, C. *J. Electroanal. Chem.* **2008**, *621*, 178.

(26) Ambrosi, A.; Pumera, M. *J. Phys. Chem. C* **2013**, *117*, 2053.

(27) Brownson, D. A. C.; Varey, S. A.; Hussain, F.; Haigh, S. J.; Banks, C. E. *Nanoscale* **2014**, *6*, 1607.

(28) Valota, A. T.; Kinloch, I. A.; Novoselov, K. S.; Casiraghi, C.; Eckmann, A.; Hill, E. W.; Dryfe, R. A. W. *ACS Nano* **2011**, *5*, 8809.

3.0 ORIGIN OF ASYMMETRY OF PAIRED NANOGAP VOLTAMMOGRAMS BASED ON SCANNING ELECTROCHEMICAL MICROSCOPY: CONTAMINATION NOT ADSORPTION

This work has been published as Chen, R.; Balla, R. J.; Li, Z.; Liu, H.; Amemiya, S. Origin of Asymmetry of Paired Nanogap Voltammograms Based on Scanning Electrochemical Microscopy: Contamination not adsorption, *Anal. Chem.* **2016**, *88,* 8323-8331.The thesis author fabricated electrodes, collected and analyzed experimental data.

3.1 INTRODUCTION

Nanogap voltammetry based on scanning electrochemical microscopy[1-3] (SECM) emerged as a powerful nanoelectrochemical method to study ultrafast electron-transfer (ET) reactions at ultramicroelectrode tips and substrate electrodes. Recently, we enabled SECM-based nanogap voltammetry of a macroscopic substrate under quasi-steady states despite cycling the substrate potential within a wide range across the formal potential of a target redox couple.[4,5] With this approach, an SECM tip was positioned at a nanometer distance from the substrate to amperometrically monitor the reactant or product of a substrate reaction under high mass transport conditions across the tip–substrate nanogap. The resultant pair of nanogap voltammograms based on the oxidation and reduction of the redox couple enabled the reliable assessment of extremely high standard ET rate constants, k^0. Importantly, we formed an exceptionally stable nanogap by

developing an isothermal chamber to prevent the nanoscale thermal drift of the tip position.[6] Moreover, we revealed and prevented the electrostatic and electrochemical damage of submicrometer- and nanometer-sized platinum[7] and carbon[8] tips, which had been unnoticed previously.[9,10]

More recently, we reported the non-ideal asymmetry of paired nanogap voltammograms of (ferrocenylmethyl)trimethylammonium (Fc^+) at highly oriented pyrolytic graphite (HOPG)[11] as an important model of graphitic nanocarbons.[12] The amperometric response of a 1 μm-diameter Pt tip in nanogap voltammetry was largely enhanced when the electrolyte solution was prepared from ultrapure water with total organic carbon of 2 ppb or less and filled in a tightly sealed cell to prevent the organic contamination of the solution and, subsequently, the HOPG surface. The tip current, however, was higher by up to 25% in the substrate generation/tip collection (SG/TC) mode than the feedback mode, which is defined as the asymmetry of paired nanogap voltammograms. We hypothesized that non-ideal asymmetry between the two operation modes was due to airborne contamination of the HOPG surface[13,14] during ~15 minute-long air exposure for assembly of the sealed cell. We ascribed the higher tip current in the SG/TC mode to the higher permeability of the hydrophobic contaminant layer to less charged Fc^+ (Figure 3-1A). A lower tip current in the feedback mode was ascribed to the slower transport of more hydrophilic Fc^{2+} through the contaminant layer (Figure 3-1B).

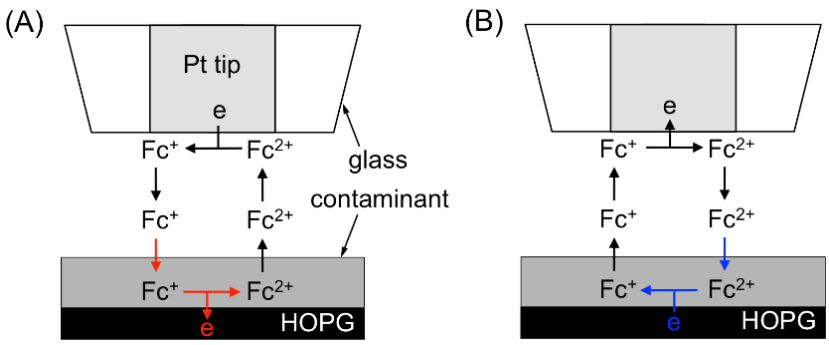

Figure 3-1. Scheme of SECM-based nanogap voltammetry in (A) SG/TC and (B) feedback modes at the airborne-contaminated HOPG surface. Fc^{+} and Fc^{2+} represent (ferrocenylmethyl)trimethylammonium and its oxidized form, respectively.

Herein, we report on the advantage of SECM-based nanogap voltammetry to assess the cleanness of a substrate surface in the electrolyte solution by confirming that the non-ideal asymmetry of paired nanogap voltammograms of the $Fc^{2+/+}$ couple at the HOPG surface is due to its airborne contamination.[11] Experimentally, we obtain symmetric pairs of nanogap voltammograms when HOPG is exfoliated in humidified air to form a nanometer-thick water adlayer, which reduces airborne contamination to <30% of the whole HOPG surface as confirmed by contact angle and ellipsometry measurements.[15] In addition, weak Fc^{+} adsorption on the HOPG surface is found as the origin of not the asymmetry, but the hysteresis of each nanogap voltammogram. Importantly, these results unambiguously disprove the recently proposed mechanismm[16] that the tip current in the SG/TC mode is enhanced more by the electron-exchange reaction mediated by Fc^{2+} adsorbed on the glass sheath of a Pt tip, i.e.

$$Fc^{+}(water) + Fc^{2+}(glass) \rightleftharpoons Fc^{2+}(water) + Fc^{+}(glass) \quad (1)$$

We demonstrate quantitatively that this reaction is highly unfavorable thermodynamically, because a product, Fc^{+}, is not adsorbed on the glass surface.[16]

Mechanistically, this study focuses on the $Fc^{2+/+}$ couple to prove that its electron-transfer reaction at the HOPG surface is mediated by the simple outer-sphere pathway as represented by[17,18]

$$Fc^{2+}(water) + e \rightleftharpoons Fc^{+}(water) \quad (2)$$

which was only assumed in our previous study[11] and was questioned recently.[16,19] Symmetric pairs of reversible nanogap voltammograms at the water-protected HOPG surface yield extremely high k^0 values of ≥12 cm/s, which we assign to the outer-sphere pathway, because we find quantitatively that no Fc^{2+} adsorption on the HOPG surface[16] thermodynamically suppresses other pathways, i.e., the inner-sphere ET pathway[17,18]

$$Fc^{2+}(HOPG) + e \rightleftharpoons Fc^{+}(HOPG) \quad (3)$$

and the electron-exchange pathway[20]

$$Fc^{+}(HOPG) + Fc^{2+}(water) \rightleftharpoons Fc^{2+}(HOPG) + Fc^{+}(water) \quad (4)$$

It is simply a misconception about basic electrochemical thermodynamics that these pathways are important for the $Fc^{2+/+}$ couple at the HOPG surface, where only Fc^{+} is adsorbed.[16,19]

3.2 THEORY

3.2.1 SECM-Based Nanogap Voltammetry.

In this work, we develop a theoretical model (Figure 3-7) to demonstrate that the asymmetry of paired nanogap voltammograms is not due to adsorption of Fc^{+} or Fc^{2+} on the HOPG surface or the glass sheath of a Pt tip, respectively. The model is defined by using dimensionless parameters (see Supporting Information) and is numerically solved by using the finite element simulation package, Multiphysics 5.2 (COMSOL, Burlington, MA). Specifically, we simulate the amperometric tip current based on Fc^{+} oxidation in the feedback mode and Fc^{2+} reduction in the SG/TC mode (Figure 3-1) while the HOPG potential is cycled in initially cathodic and anodic

directions, respectively. The simulated tip current is normalized against the tip current in the bulk solution, $i_{T,\infty}$, as given by

$$i_{T,\infty} = -4xnFD_{Fc^+}c_0a \quad (5)$$

where x is a function of glass geometry including RG[21] (= r_g/a; r_g and a are outer and inner tip radii, respectively), $n = 1$ for the one-electron oxidation of Fc^+, and D_{Fc^+} (= 6.0×10^{-6} cm^2/s)[11] and c_0 (= 0.3 mM) are the diffusion coefficient and concentration of Fc^+ in the bulk solution, respectively.

Noticeably, our model employs the terminology of the feedback mode,[22] where tip-generated Fc^{2+} is reduced to Fc^+ at the HOPG surface to complete redox cycling between the tip and the substrate (Figure 3-1B). The tip current in the feedback mode diminishes at more positive potentials owing to a shielding effect from the substrate.[23] This operation mode should not be called the competition mode,[16] which examines the identical irreversible reaction (e.g., the reduction of oxygen to water) at both tip and substrate electrodes without redox cycling between them.[24]

3.2.2 Model.

In our model, a disk-shaped SECM tip with inner and outer radii of 0.5 and 1 μm, respectively, is positioned at a fixed nanometer distance, d, from the HOPG surface in the electrolyte solution containing only Fc^+, which corresponds to initial conditions of $c_{Fc^+}(r,z,0) = c_0$ and $c_{Fc^{2+}}(r,z,0) = 0$ at $t = 0$ in the cylindrical coordinate. When the cycle of the HOPG potential is initiated at $t = 0$, the tip potential is stepped to oxidize Fc^+ in the feedback

mode or reduce Fc^{2+} in the SG/TC mode at diffusion-limited rates. The concentration of each redox-active species, *i* (=Fc^{+} or Fc^{2+}), is determined by the Fick's second law to satisfy

$$\frac{\partial c_i(r,z,t)}{\partial t} = D_i\left[\frac{\partial^2 c_i(r,z,t)}{\partial r^2} + \frac{1}{r}\frac{\partial c_i(r,z,t)}{\partial r} + \frac{\partial^2 c_i(r,z,t)}{\partial z^2}\right] \tag{6}$$

where D_i is the diffusion coefficient of the redox-active species. The amperometric tip current is calculated by solving eq 6 with the following boundary conditions at the HOPG surface and the glass sheath of a Pt tip as well as other boundary conditions defined in Figure 3-7.

HOPG. Boundary conditions at the HOPG surface ($z = -d$) are based on the outer-sphere ET reaction of diffusing Fc^{+} and Fc^{2+} (eq 2) and Fc^{+} adsorption. The HOPG potential, *E*, is cycled to yield the ET rate, v_{et}^{HOPG}, as given by reduction and oxidation rate constants, k_f^{HOPG} and k_b^{HOPG}, respectively, based on the Butler–Volmer model[25]

$$v_{et}^{HOPG} = k_f^{HOPG} c_{Fc^{2+}}(r,-d,t) - k_b^{HOPG} c_{Fc^{+}}(r,-d,t) \tag{7}$$

with

$$k_f^{HOPG} = k^0 \exp[-\alpha f(E-E^{0'})] \tag{8}$$

$$k_b^{HOPG} = k^0 \exp[(1-\alpha) f(E-E^{0'})] \tag{9}$$

where α is the transfer coefficient, $E^{0'}$ is the formal potential of the redox couple, and $f = F/RT$. In this work, reversible electron transfer at the HOPG surface is assumed (i.e., $\lambda = ak^0 / D_{Fc^{+}} = 100$ in eq 39). In addition, Fc^{+} adsorption on the HOPG surface[16,19] is defined as

$$Fc^{+}(\text{water}) \rightleftharpoons Fc^{+}(\text{HOPG}) \tag{10}$$

The adsorption rate, v_{ads}^{HOPG}, is given by[26]

$$v_{\text{ads}}^{\text{HOPG}} = k_{\text{ads}}^{\text{HOPG}} \left\{ c_{\text{Fc}^+}(r,-d,t)\left[\Gamma_{\text{Fc}^+}^{\text{HOPG}} - \Gamma_{\text{Fc}^+}^{\text{HOPG}}(r,-d,t)\right] - \frac{\Gamma_{\text{Fc}^+}^{\text{HOPG}}(r,-d,t)}{\beta_{\text{Fc}^+}^{\text{HOPG}}} \right\} \quad (11)$$

where $k_{\text{ads}}^{\text{HOPG}}$ is the adsorption rate constant, $\Gamma_{\text{Fc}^+}^{\text{HOPG}}$ is the saturated concentration of Fc^+ on the HOPG surface, $\Gamma_{\text{Fc}^+}(r,-d,t)$ is its surface concentration, and $\beta_{\text{Fc}^+}^{\text{HOPG}}$ is an equilibrium parameter in an Langmuir isotherm.[27] Overall, boundary conditions at the HOPG surface are defined as

$$D_{\text{Fc}^{2+}}\left[\frac{\partial c_{\text{Fc}^{2+}}(r,z,t)}{\partial z}\right]_{z=-d} = -v_{\text{et}}^{\text{HOPG}} \quad (12)$$

$$D_{\text{Fc}^+}\left[\frac{\partial c_{\text{Fc}^+}(r,z,t)}{\partial z}\right]_{z=-d} = v_{\text{et}}^{\text{HOPG}} - v_{\text{ads}}^{\text{HOPG}} \quad (13)$$

$$\left[\frac{\partial \Gamma_{\text{Fc}^+}(r,z,t)}{\partial t}\right]_{z=-d} = v_{\text{ads}}^{\text{HOPG}} \quad (14)$$

where the diffusion of Fc^+ on the HOPG surface is neglected.[16]

Glass. Boundary conditions are defined for the glass sheath surrounding a Pt tip, where Fc^{2+} may be adsorbed[16]

$$Fc^{2+}(\text{water}) \rightleftharpoons Fc^{2+}(\text{glass}) \quad (15)$$

The adsorption rate, $v_{\text{ads}}^{\text{glass}}$, is given by

$$v_{\text{ads}}^{\text{glass}} = k_{\text{ads}}^{\text{glass}} \left\{ c_{\text{Fc}^{2+}}(r,z,t)\left[\Gamma_{\text{Fc}^{2+}}^{\text{glass}} - \Gamma_{\text{Fc}^{2+}}^{\text{glass}}(r,z,t)\right] - \frac{\Gamma_{\text{Fc}^{2+}}^{\text{glass}}(r,z,t)}{\beta_{\text{Fc}^{2+}}^{\text{glass}}} \right\} \quad (16)$$

where k_{ads}^{glass} is the adsorption rate constant, $\Gamma_{Fc^{2+}}^{glass}$ is the saturated concentration of Fc^{2+} on the glass surface, $\Gamma_{Fc^{2+}}^{glass}(r,z,t)$ is its surface concentration, and $\beta_{Fc^{2+}}^{glass}$ is an equilibrium parameter in an Langmuir isotherm.[27] Accordingly, boundary conditions at the glass surface are given by

$$N_{Fc^{2+}}^{glass} = -\nu_{ads}^{glass} \quad (17)$$

$$N_{Fc^{+}}^{glass} = 0 \quad (18)$$

$$\left[\frac{\partial \Gamma_{Fc^{2+}}^{glass}(r,z,t)}{\partial t}\right] = \nu_{ads}^{glass} \quad (19)$$

where $N_{Fc^{2+}}^{glass}$ and $N_{Fc^{+}}^{glass}$ are fluxes of Fc^{2+} and Fc^{+} normal to the glass surface, respectively. The diffusion of Fc^{2+} on the glass surface is neglected.[16]

3.2.3 Fc^{+} Adsorption on the HOPG Surface.

Here, we consider relatively strong Fc^{+} adsorption on the HOPG surface to clearly demonstrate its effects on asymmetry and hysteresis of paired nanogap voltammograms. Specifically, a larger $\beta_{Fc^{+}}^{HOPG}$ value of 1.0×10^6 cm^3/mol[19] is used in comparison with our experimental $\beta_{Fc^{+}}^{HOPG}$ value of 1.7×10^5 cm^3/mol (see Results and Discussion). The respective $\beta_{Fc^{+}}^{HOPG}$ values correspond to a dimensionless parameter of Λ_{HOPG} = 0.30 and 0.05 (= $c_0 \beta_{Fc^{+}}^{HOPG}$ in eq 46). In addition, we assume that fast Fc^{+} adsorption on the HOPG surface maintains equilibrium ($\kappa_{HOPG} = k_{ads}^{HOPG} c_0 a^2 / D_{Fc^{+}} = 100$ in eq S-16) and only for simplicity that Fc^{2+} is not adsorbed on the glass surface (k_{ads}^{glass} = 0). Moreover, $D_{Fc^{+}}$ = $D_{Fc^{2+}}$ is assumed so that nanogap voltammograms

based on feedback and SG/TC modes are symmetric without Fc^+ adsorption on the HOPG surface (red lines in Figure 3-2). No hysteresis of the adsorption-free sigmoidal voltammograms confirms the quasi-steady-state mass transport of Fc^+ and Fc^{2+} across the nanogap during the cycle of the HOPG potential at 0.05 V/s, which corresponds to a sufficiently small dimensionless potential sweep rate, σ, of 8.1×10^{-4} (<< 0.01) in eq 41.[4]

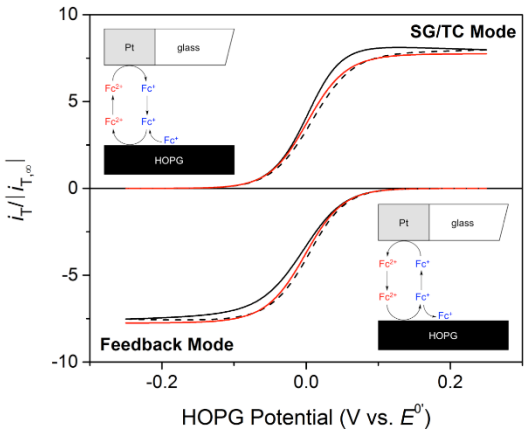

Figure 3-2. Simulated nanogap voltammograms with (black) and without (red) Fc^+ adsorption on the HOPG surface at $d/a = 0.1$. Solid and dashed lines represent forward and reverse waves, respectively, which overlap with each other without Fc^+ adsorption (red).

Relatively strong Fc^+ adsorption on the HOPG surface results in significantly higher and lower current responses in SG/TC and feedback modes, respectively, during the forward potential sweep than those during the reverse potential sweep, which are nearly symmetric between both operation modes to show hysteresis (Figure 3-2). On one hand, the tip current in the SG/TC mode is enhanced more during the forward potential sweep from –0.25 V to 0.25 V (solid line in the top panel of Figure 3-2) at the HOPG surface, where Fc^+ is initially adsorbed, and then desorbed and oxidized (eqs 10 and 2, respectively) at >0 V to generate Fc^{2+}, which enhances the tip current (the

top-left inset of Figure 3-2). Subsequently, no Fc^+ is adsorbed on the HOPG surface at the switching potential of 0.25 V so that the tip current during the reverse potential sweep (dashed line) is very similar to that without Fc^+ adsorption on the HOPG surface (red line). On the other hand, the tip current in the feedback mode is less enhanced during the forward potential sweep from 0.25 V to –0.25 V at the HOPG surface (solid line in the bottom panel of Figure 3-2), which is initially uncovered with Fc^+ to adsorb Fc^+ produced from tip-generated Fc^{2+} (the bottom-right inset of Figure 3-2). Subsequently, the tip current appears higher during the reverse potential sweep despite a negligible effect of Fc^+ adsorption from the HOPG surface, which is already equilibrated with Fc^+ to adsorb no more Fc^+ produced from tip-generated Fc^{2+}.

It should be emphasized that the asymmetry and hysteresis of experimental nanogap voltammograms are less serious, where Fc^+ adsorption on the HOPG surface is weaker than considered in this theory section. Nanogap voltammetry is intrinsically sensitive to surface adsorption because of the large surface–volume ratio of a tip–substrate nanogap.[16] In fact, the initial number of Fc^+ molecules adsorbed on the HOPG surface under a tip significantly exceeds the number of Fc^+ molecules in the solution in the nanogap under the tip. Quantitatively, the initial mole ratio of adsorbed Fc^+ with respect to Fc^+ in the gap is represented by a Langmuir isotherm as[27]

$$\frac{\Gamma_{Fc^+}^{HOPG}(r,-d,0)}{dc_0} = \frac{\Lambda_{HOPG}}{1+\Lambda_{HOPG}} \frac{\Gamma_{Fc^+}^{HOPG}}{dc_0} \tag{20}$$

Relatively strong Fc^+ adsorption (Λ_{HOPG} = 0.30) on the HOPG surface yields a mole ratio of 38.5 in eq 20 with d = 0.1 μm (= 0.2a) and $\Gamma_{Fc^+}^{HOPG}$ = 5 × 10^{-10} mol/cm^2.[16] Our experimental Λ_{HOPG} value of 0.05 yields a lower mole ratio of 7.9.

3.2.4 Fc^{2+} Adsorption on the Glass Surface.

Here, we find that Fc^{2+} adsorption on the glass surface[16] is unimportant, not only because the resultant pair of nanogap voltammograms (black lines in Figure 3-3) gives the same limiting current in both feedback and SG/TC modes as expected for adsorption-free voltammograms (red lines), but also because their hysteresis is different from the hysteresis of experimental voltammograms, which is ascribed to Fc^{+} adsorption on the HOPG surface as elaborated in the next paragraph. Importantly, our model does not consider the electron-exchange reaction mediated by Fc^{2+} adsorbed on the glass surface (eq 1), which is thermodynamically highly unfavorable, but was considered in the recently proposed model[16] to obtain asymmetric pairs of nanogap voltammograms. In addition, we neglect Fc^{+} adsorption on the HOPG surface ($k_{ads}^{HOPG} = 0$) only for simplicity. Otherwise, our model employs the same assumptions as the recent model[16] that Fc^{2+} adsorption on the glass surface is fast enough to maintain equilibrium ($\kappa_{glass} = k_{ads}^{glass} c_0 a^2 / D_{Fc^+} = 100$ in eq 50) and that substantial Fc^{2+} adsorption on the glass surface is represented by a $\beta_{Fc^{2+}}^{glass}$ value of 2.56×10^6 cm^3/mol,[16] which corresponds to a dimensionless parameter of $L_{glass} = 0.768$ (= $c_0 \beta_{Fc^{2+}}^{glass}$ in eq 53).

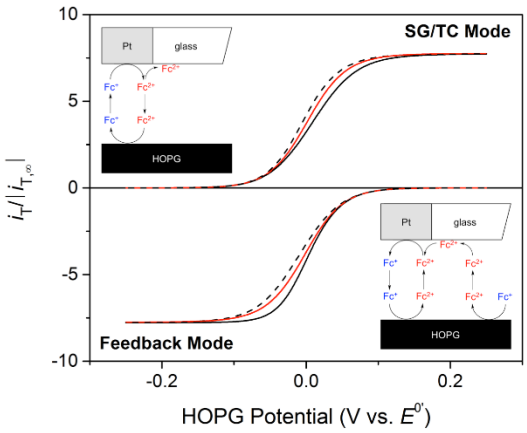

Figure 3-3. Simulated nanogap voltammograms with (black) and without (red) Fc^{2+} adsorption on the glass sheath of a tip at d/a = 0.1. Solid and dashed lines represent forward and reverse waves, respectively, which overlap with each other without Fc^{+} adsorption (red).

Advantageously, the hysteresis of nanogap voltammograms caused by Fc^{2+} adsorption on the glass surface (Figure 3-3) is distinguishable from the hysteresis caused by Fc^{+} adsorption on the HOPG surface (Figure 3-2). In the SG/TC mode, Fc^{2+} adsorption on the glass surface results in the less enhancement of the tip current during the forward potential sweep, where Fc^{2+} is generated at the HOPG surface under the tip and is adsorbed on the initially Fc^{2+}-free glass surface (the top-left inset of Figure 3-3). Subsequently, the tip current during the reverse potential sweep appears higher despite a small effect of Fc^{2+} adsorption on the glass surface to better overlap with an adsorption-free voltammogram. By contrast, Fc^{+} adsorption on the HOPG surface enhances the tip current more during the forward potential sweep in the SG/TC mode (Figure 3-2). In the feedback mode, the tip current is enhanced more during the forward potential sweep, where Fc^{2+} that is initially adsorbed on the glass surface is desorbed, and transported to and reduced at the HOPG surface to regenerate Fc^{+} for its oxidation at the tip (the bottom-right inset of Figure 3-3).

By contrast, Fc^+ adsorption on the HOPG surface results in the less enhancement of the tip current during the forward potential sweep in the feedback mode (Figure 3-2).

Overall, the hysteresis of experimental nanogap voltammograms is controlled by Fc^+ adsorption on the HOPG surface, not by Fc^{2+} adsorption on the glass sheath (see Results and Discussion). This result suggests that the latter is even weaker than the former, although this theory section employs the $\beta_{Fc^{2+}}^{glass}$ and $\Gamma_{Fc^{2+}}^{glass}$ (= 2.3×10^{-9} mol/cm^2) values that are larger than $\beta_{Fc^+}^{HOPG}$ and $\Gamma_{Fc^+}^{HOPG}$ values.[16]

3.3 EXPERIMENTAL SECTION

3.3.1 Chemicals and Materials.

The hexafluorophosphate salt of Fc^+ was prepared by the metathesis of its iodide salt (Strem Chemicals, Newburyport, MA) and ammonium hexafluorophosphate (Strem Chemicals). SPI-1 grade HOPG was obtained from SPI Supplies (West Chester, PA). A Milli-Q Advantage A10 water purification system (EMD Millipore) was used to obtain UV-treated ultrapure water with a TOC value of 2 ppb as measured by using an internal online TOC monitor. The final product of Milli-Q water purification process was passed through a specific activated-carbon filter (VOC Pak, EMD Millipore) to remove the traces of volatile organic contaminants. Filtered water was collected in a class 100 vertical laminar flow hood (AC632TLFC, AirClean Systems, Raleigh, NC) equipped with a bonded carbon filter (ACF100, AirClean Systems) to minimize airborne

contamination. The Milli-Q system was fed with the water (15.0 MΩ·cm) purified from tap water by using Elix 3 Advantage (EMD Millipore).

3.3.2 Tip Fabrication.

A Pt tip with inner and outer diameters of ~1 and ~2 μm was fabricated as reported elsewhere.[4,28] A Pt tip was milled by using a focused ion beam instrument (SMI3050SE FIB-SEM, Seiko Instruments, Chiba, Japan) with low-energy Ga^+ beam at 5 keV to reduce its implantation into the platinum surface. A freshly milled Pt tip was stored in a class 100 vertical laminar flow hood (AC632LFC, AirClean Systems) to prevent contamination with airborne particles. A tip was protected from electrostatic discharge[7,8] under sufficiently high humidity[29] (>50%).

3.3.3 SECM Measurement.

A homebuilt SECM instrument with an isothermal chamber[6] was used as reported elsewhere for the study of HOPG.[11] In this work, a non-protected HOPG surface was obtained by peeling HOPG using scotch tape in the clean hood with a bonded carbon filter. In addition, a water-protected HOPG surface was obtained by peeling HOPG under humidified conditions surrounded by dry ice[15] in the filtered air. A Pt tip was cleaned in piranha solution (a 1:3 mixture of 30% H_2O_2 and 95.0− 98.0% H_2SO_4) and ultrapure water immediately before it was immersed in the electrolyte solution of the sealed SECM cell. Caution: piranha solution reacts violently with organics and should be handled with extreme care! Pt and Ag/AgCl wires were used as counter and reference electrodes, respectively.

Electrochemical measurements were carried out by using a bipotentiostat (CHI 802D, CH Instruments, Austin, TX), which was modified[30] to eliminate possible causes of tip damage (Supporting Information). Tip and HOPG electrodes were connected to channels 1 and 2 of the bipotentiostat, respectively, to minimize the effect of their crosstalk on the tip current. These channels were "swapped" internally to apply constant tip potentials of 0.55 and 0.15 V in feedback and SG/TC modes, respectively, during the cycle of the HOPG potential at 0.05 V/s from initial potentials of 0.55 and 0.15 V to switching potentials of 0.15 and 0.55 V in the respective operation modes.

3.4 RESULTS AND DISSCUSSION

3.4.1 Nanogap Voltammetry with Non-Protected HOPG.

In the previous work, we obtained asymmetric pairs of nanogap voltammograms of the $Fc^{2+/+}$ couple in SG/TC and feedback modes when HOPG was not protected with a water adlayer[15] and was contaminated during its exfoliation and assembly into a sealed SECM cell in a clean hood.[11] In this study, we equipped a clean hood with a bonded carbon filter for the removal of airborne organic contaminants to obtain more symmetric pairs of nanogap voltammograms (Figure 3-4; the same color is used for a pair of voltammograms measured at the same tip position). This result supports our hypothesis that the asymmetry is due to airborne contamination of the HOPG surface (Figure 3-1).[11] The use of the carbon filter, however, still yielded the higher amperometric response of a 1 μm-diameter Pt tip in the SG/TC mode than in the feedback mode, which indicates that the non-protected HOPG surface was contaminated in the filtered air. Importantly, the

asymmetry is not due to different diffusion coefficients of Fc^{2+} and Fc^{+}. In fact, the identical diffusion coefficient of Fc^{+} and Fc^{2+} was confirmed by symmetric pairs of nanogap voltammograms as obtained when the tip–HOPG distance was long enough to observe no feedback effect (Figure 3-8). Moreover, the asymmetry is not due to the drift of the tip–HOPG distance, which was stabilized by using an isothermal chamber[6] (Figure 3-9).

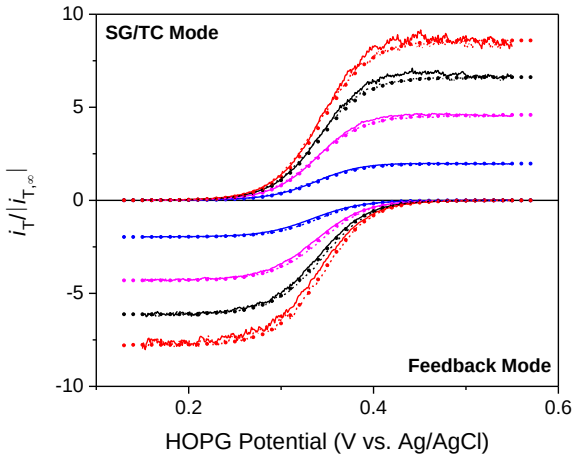

Figure 3-4. Asymmetric pairs of nanogap voltammograms of 0.3 mM Fc^{+} at the non-protected HOPG surface in 50 mM KCl. Forward and reverse waves are represented by solid and dashed lines. Dots represent reversible voltammograms without any adsorption effect (eqs 56 and 57 with $E^{0\prime}$ = 0.340 V, a = 506 nm, RG = 2.0, and parameters listed in Table 3-1).

We determined ratios of limiting currents in the SG/TC mode with respect to those in the feedback mode to quantitatively assess the asymmetry of paired nanogap voltammograms without the error caused by their hysteresis (Figure 3-4). The nearly identical limiting current was obtained near the switching potential without hysteresis between forward and reverse waves of each voltammogram. Ratios of 1.08 ± 0.04 (N = 25) were obtained with the non-protected HOPG surface exfoliated in the filtered air. These ratios are significantly smaller than ratios of up to 1.25

at the HOPG surface exfoliated in a clean hood without the bonded carbon filter.[11] By contrast, each voltammogram showed hysteresis around the formal potential of the $Fc^{2+/+}$ couple. This hysteresis is consistent with the hysteresis expected for Fc^{+} adsorption on the HOPG surface, which mainly affects the forward wave (Figure 3-2). In the SG/TC mode, the tip current was more enhanced during the forward potential sweep from 0.15 V to 0.55 V at the HOPG surface, where Fc^{+} was initially adsorbed and then desorbed and oxidized to produce additional Fc^{2+}. In the feedback mode, the tip current was less enhanced during the forward potential sweep from 0.55 V to 0.15 V, where the HOPG surface was initially free from Fc^{+} to eventually adsorb Fc^{+} from the solution in the gap in competition with its oxidation at the tip.

The reverse waves of asymmetric nanogap voltammograms (dashed lines in Figure 3-4) overlapped well with theoretical reversible voltammograms (dots) to yield slightly shorter tip–HOPG distances from higher limiting currents and, subsequently, slightly higher k^0 values for the SG/TC mode than the feedback mode (Table 3-1). We analyzed reverse waves, which are less affected by Fc^{+} adsorption on the HOPG surface (see the Theory section). Theoretical nanogap voltammograms were obtained from the approximate equations based on no Fc^{+} adsorption on the HOPG surface (eqs 56 and 57).[4] The k^0 values thus estimated from reversible nanogap voltammograms correspond to the diffusion-limited minimum value, i.e., $k^0 = 10D_{Fc^+}/d$,[11] where tip–substrate distances were determined from limiting currents. In addition, this analysis yielded very short tip–HOPG distances of down to $0.1a$ to confirm that sharp Pt tips with small *RG* values of ~2 were flat, smooth, and free from recession caused by electrostatic and electrochemical damage.[7,8]

Table 3-1. Parameters Determined from Asymmetric and Symmetric Pairs of Nanogap Voltammograms

Asymmetric Pairs[a]				Symmetric Pairs[b]	
SG/TC Mode		Feedback Mode		Both Modes	
d (nm)	k^0 (cm/s)	d (nm)	k^0 (cm/s)	d (nm)	k^0 (cm/s)
45	≥13	50	≥12	52	≥12
59	≥10	64	≥9.3	65	≥9.2
90	≥6.7	96	≥6.2	98	≥6.1
273	≥2.2	273	≥2.2	270	≥2.2

[a] From Figure 3-4. [b] From Figure 3-5.

3.4.2 Nanogap Voltammetry with Water-Protected HOPG.

We were able to obtain symmetric pairs of nanogap voltammograms of the $Fc^{2+/+}$ couple at the water-protected HOPG surface as exfoliated in humidified air[15] (Figure 3-5). This result unambiguously confirms that the asymmetry of paired nanogap voltammograms is due to airborne contamination of the HOPG surface as hypothesized in our previous work.[11] Quantitatively, ratios of limiting currents in the SG/TC mode with respect to those in the feedback mode were 0.98 ± 0.05 (N = 39) for water-protected HOPG. Moreover, the hysteresis of each nanogap voltammogram (Figure 3-5) is consistent with the hysteresis caused by adsorption of Fc^+ on the HOPG surface, which affects the forward wave of a nanogap voltammogram (see above). Thus, the reverse wave of each nanogap voltammogram (dashed lines in Figure 3-5) overlapped well with a reversible voltammogram given by approximate equations without Fc^+ adsorption on the HOPG surface[4]

(dots) to determine tip–HOPG distances and the corresponding diffusion-limited minimum k^0 values without an ambiguity due to an adsorption effect. Each symmetric pair of reversible nanogap voltammograms gave a consistent d value of down to 52 nm and the corresponding k^0 value of up to 12 cm/s or higher (Table 3-1).

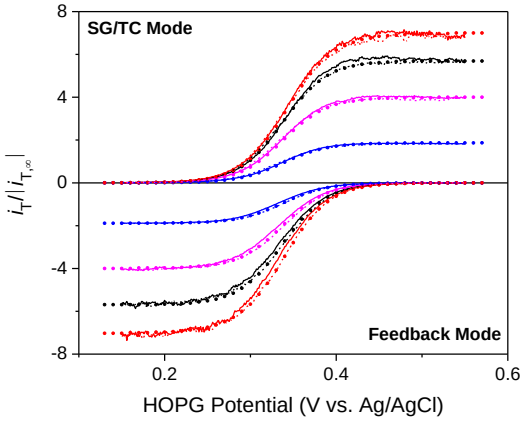

Figure 3-5. Symmetric nanogap voltammograms of 0.3 mM Fc^+ at the water-protected HOPG surface in 50 mM KCl. Forward and reverse waves are represented by solid and dashed lines. Dots represent reversible voltammograms without any adsorption effect (eqs 56 and 57) and fit with reverse waves to yield $E^{0'}$ = 0.340 V, a = 490 nm, RG = 1.9, and parameters listed in Table 3-1.

Extremely high k^0 values of ≥12 cm/s are not only reliably determined from symmetric pairs of nanogap voltammograms at water-protected cleaner HOPG surfaces, but also still lower than the highest k^0 value expected from the Marcus theory for an adiabatic outer-sphere ET reaction.[31] Importantly, the ET reaction of the $Fc^{2+/+}$ couple at the HOPG surface is mediated by the simple outer-sphere pathway as discussed below. A k^0 value of an adiabatic ET reaction is related to the self-exchange rate constant as given by[31]

$$k^0 = Z_{het}\sqrt{k_{ex} / Z_{bi}} \quad (21)$$

where $Z_{het} \sim 10^4$ cm/s and $Z_{bi} \sim 10^{11}$ $M^{-1}s^{-1}$ are heterogeneous and bimolecular collision frequencies, respectively.[31] A k^0 value of 1×10^2 cm/s is obtained from eq 21 with a k_{ex} value of 9×10^6 $M^{-1}s^{-1}$ for the $Fc^{2+/+}$ couple in water.[32] By contrast, much lower k^0 values of 0.1−1 cm/s were estimated for the $Fc^{2+/+}$ couple at the "pristine" HOPG surface[33] by scanning electrochemical cell microscopy.[34] These k^0 values were massively underestimated, perhaps because of much lower mass-transport conditions of this technique and/or because of contamination of the HOPG surface exposed to ambient air during the whole kinetic measurement.

3.4.3 Weak Fc^+ Adsorption on the HOPG Surface.

We demonstrate that Fc^+ adsorption on the non-protected HOPG surface is too weak to cause the asymmetry of paired nanogap voltammograms that was observed experimentally. In addition, this argument is supported by the finding that Fc^+ adsorption on non-protected and water-protected HOPG surfaces is similarly weak, thereby confirming that the symmetry of paired nanogap voltammograms at the latter surface (Figure 3-5) is not due to weaker Fc^+ adsorption on the cleaner HOPG surface. Specifically, we studied Fc^+ adsorption on non-protected and water-protected HOPG surfaces by cyclic voltammetry[19] (CV) at potential sweep rates of 0.1–10 V/s after nanogap voltammetric experiments (e.g., Figure 3-6A for water-protected HOPG). An *iR* drop through the 50 mM KCl solution was compensated to yield well-defined CVs at fast potential sweep rates, whereas the transient instability of the potentiostat was caused at initial and switching potentials. The forward waves of CVs at fast potential sweep rates were higher than expected for diffusion-limited CVs (e.g., 10 V/s in the inset of Figure 3-6A), which indicates that Fc^+ was

initially adsorbed on the HOPG surface.[19,35] We analyzed experimental CVs at non-protected and water-protected HOPG surfaces (see Supporting Information) to obtain similar $\beta_{Fc^+}^{HOPG}$ values of $(1.7 \pm 0.2) \times 10^5$ cm^3/mol ($N = 3$) and $(1.8 \pm 0.4) \times 10^5$ cm^3/mol ($N = 5$), respectively. These $\beta_{Fc^+}^{HOPG}$ values in 50 mM KCl are smaller than $\beta_{Fc^+}^{HOPG}$ values of $(5 \pm 3) \times 10^5$ and $(1.1 \pm 0.3) \times 10^6$ cm^3/mol as reported for freshly peeled and aged HOPG, respectively, in 1 M KCl.[19] Noticeably, Fc^+ adsorption on the HOPG surface was too weak in 2–100 mM KCl to be noticed by employing scanning electrochemical cell microscopy.[34]

Quantitatively, the finite element simulation gave nearly symmetric pairs of nanogap voltammograms based on weak Fc^+ adsorption on the non-protected HOPG surface (Figure 6B), where the $\beta_{Fc^+}^{HOPG}$ value was determined by CV (see above) to yield $\Lambda_{HOPG} = 0.05$ ($= c_0 \beta_{Fc^+}^{HOPG}$ in eq 46). The ratio of simulated limiting currents in the SG/TC mode with respect to those in the feedback mode was 1.02 at various tip–HOPG distances that were examined experimentally (Figure 3-4 and Table 3-1). We employed student's *t* test (95% confidence level) to find that this ratio is significantly smaller than experimental ratios of 1.08 ± 0.04 ($N = 25$) at non-protected HOPG surfaces as prepared in filtered air as well as ratios of up to 1.25 at non-protected HOPG surfaces as prepared in non-filtered air.[11] A simulated ratio of 1.02 with weak Fc^+ adsorption on the HOPG surface is also statistically higher than experimental values of 0.98 ± 0.05 ($N = 39$) at water-protected HOPG surfaces, but is much closer to an adsorption-free ratio of 1.00 than a simulated ratio of 1.06 (at switching potentials in Figure 3-2) for relatively strong Fc^+ adsorption on the HOPG surface with a larger $\beta_{Fc^+}^{HOPG}$ value of 1.0×10^6 cm^3/mol (see above).[19]

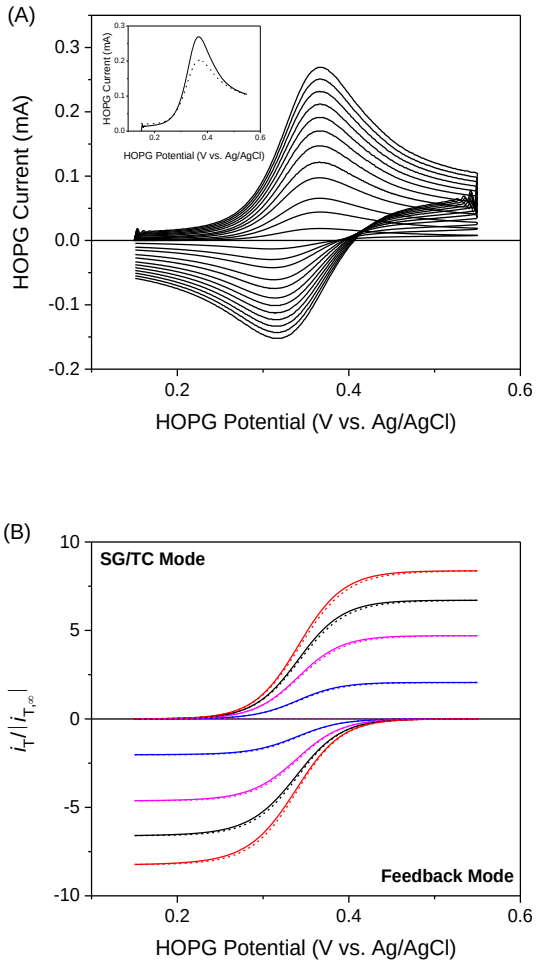

Figure 3-6. (A) CVs of 0.3 mM Fc^+ at the water-protected HOPG surface in 50 mM KCl. Potential sweep rates are 0.1, 0.5, 1, 2, 3, 4, 5, 6, 7, 8, 9, and 10 V/s. The inset shows forward waves of experimental (solid) and simulated (dashed) CVs at 10 V/s. (B) Nanogap voltammograms simulated with weak Fc^+ adsorption on the HOPG surface at various *d* values and other parameters as determined from Figure 3-4. Solid and dashed lines represent forward and reverse waves, respectively.

Noticeably, Fc^+ is weakly adsorbed on the HOPG surface to block less than 5% of the surface during nanogap voltammetry, thereby causing a negligible error (<5 %) on the

determination of k^0 values. Specifically, the coverage of the HOPG surface with Fc^+ was highest when the surface was initially equilibrated with the bulk solution of Fc^+ (i.e., no voltammetric depletion of Fc^+ near the HOPG surface). The highest surface coverage is given by a Langmuir isotherm as[27]

$$\frac{\Gamma_{Fc^+}^{HOPG}(r,-d,0)}{\Gamma_{Fc^+}^{HOPG}} = \frac{\Lambda_{HOPG}}{1+\Lambda_{HOPG}} \quad (22)$$

Eq 22 with our experimental Λ_{HOPG} value (= $c_0 \beta_{Fc^+}^{HOPG}$) of 0.05 gives 0.047, which indicates that less than 4.7 % of the HOPG surface was blocked by adsorbed Fc^+ during nanogap voltammetry. Importantly, adsorbed Fc^+ only blocks the underlying HOPG surface and can not be oxidized directly to adsorbed Fc^{2+} through the inner-sphere pathway (eq 3), which is thermodynamically prevented when Fc^{2+} is not adsorbed on the HOPG surface (see below). Furthermore, the surface coverage is reduced at positive HOPG potentials, where Fc^+ in the solution in the gap is oxidatively depleted through the outer-sphere pathway (eq 2) to induce Fc^+ desorption from the HOPG surface.

3.4.4 Outer-Sphere ET Pathway of the $Fc^{2+/+}$ Couple at the HOPG Surface.

The aforementioned CV study also indicates negligible Fc^{2+} adsorption on the HOPG surface,[16,19] which ensures that inner-sphere (eq 3) and electron-exchange (eq 4) pathways are thermodynamically prevented. Accordingly, the ET reaction of the $Fc^{2+/+}$ couple at the HOPG surface is mediated by the simple outer-sphere pathway (eq 2). Quantitatively, the formal potential of the inner-sphere pathway, $E_{ads}^{0'}$, is much more positive than the formal potential of the outer-sphere pathway, $E^{0'}$, as given by (see Supporting Information)

$$E_{\text{ads}}^{0'} = E^{0'} - \frac{RT}{F}\ln\frac{\Gamma_{\text{Fc}^{2+}}^{\text{HOPG}}\beta_{\text{Fc}^{2+}}^{\text{HOPG}}}{\Gamma_{\text{Fc}^{+}}^{\text{HOPG}}\beta_{\text{Fc}^{+}}^{\text{HOPG}}} \quad (23)$$

where $\Gamma_{\text{Fc}^{2+}}^{\text{HOPG}}$ is the saturated concentration of Fc^{2+} on the HOPG surface, and $\beta_{\text{Fc}^{2+}}^{\text{HOPG}}$ is its equilibrium parameter in an Langmuir isotherm.[27] Negligible Fc^{2+} adsorption on the HOPG surface corresponds to $\Gamma_{\text{Fc}^{2+}}^{\text{HOPG}}\beta_{\text{Fc}^{2+}}^{\text{HOPG}} << \Gamma_{\text{Fc}^{+}}^{\text{HOPG}}\beta_{\text{Fc}^{+}}^{\text{HOPG}}$, thereby yielding $E_{\text{ads}}^{0'} >> E^{0'}$. Similarly, the equilibrium constant of the electron-exchange pathway, $K_{\text{ex}}^{\text{HOPG}}$, is much smaller than 1 as given by

$$K_{\text{ex}}^{\text{HOPG}} = \frac{\Gamma_{\text{Fc}^{2+}}^{\text{HOPG}}\beta_{\text{Fc}^{2+}}^{\text{HOPG}}}{\Gamma_{\text{Fc}^{+}}^{\text{HOPG}}\beta_{\text{Fc}^{+}}^{\text{HOPG}}} \quad (24)$$

Noticeably, it is a misconception to consider the existence of the electron-exchange pathway for the $Fc^{2+/+}$ couple at the HOPG surface (eq 4) by analogically referring to the electron-exchange reaction of a solution redox species mediated by the surface-attached film of ferrocene groups, e.g., a self-assembled monolayer.[19] This analogy is not relevant, because both oxidized and reduced forms of the ferrocene groups are covalently bound to the electrode surface. By contrast, Fc^{2+} is not adsorbed on the HOPG surface,[16,19] which thermodynamically prevents the corresponding electron-exchange reaction (eq 4).

3.4.5 Misconception about Electron Exchange at the Glass Surface.

Finally, we quantitatively disprove that the asymmetry of paired nanogap voltammograms of the $Fc^{2+/+}$ couple at the HOPG surface is due to the electron-exchange reaction mediated by Fc^{2+} adsorbed on the glass sheath of a Pt tip (eq 1).[16] In this mechanism, the tip current is more enhanced in the SG/TC mode, where Fc^{2+} is regenerated from tip-generated Fc^{+} by electron exchange with Fc^{2+} adsorbed on the glass surface. This electron-exchange reaction, however, is

thermodynamically prevented, because Fc^+ is not adsorbed on the glass surface.[16] Quantitatively, the corresponding equilibrium constant, K_{ex}^{glass}, is much smaller than 1 as given by (see Supporting Information)

$$K_{ex}^{glass} = \frac{\Gamma_{Fc^+}^{glass} \beta_{Fc^+}^{glass}}{\Gamma_{Fc^{2+}}^{glass} \beta_{Fc^{2+}}^{glass}} \quad (25)$$

where $\Gamma_{Fc^+}^{glass}$ is the saturated concentration of Fc^+ on the glass surface, and $\beta_{Fc^+}^{glass}$ is its equilibrium parameter in an Langmuir isotherm.[27] Negligible Fc^+ adsorption on the glass surface corresponds to $\beta_{Fc^+}^{glass}\Gamma_{Fc^+}^{glass} << \beta_{Fc^{2+}}^{glass}\Gamma_{Fc^{2+}}^{glass}$ to yield $K_{ex}^{glass} << 1$ in eq 25. This thermodynamic constrain was not considered in a recent model,[16] where the electron-exchange reaction based on eq 1 was oversimplified and mistakenly assumed to be irreversible as given by

$$Fc^+(water) \rightarrow Fc^{2+}(water) \quad (26)$$

Alternatively, Fc^+ adsorption on the glass surface is not required when the electron-exchange reaction at the glass surface yields

$$Fc^+(water) + Fc^{2+}(glass) \rightleftharpoons Fc^{2+}(water) + Fc^+(water) \quad (27)$$

This reaction, however, is equivalent to Fc^{2+} desorption from the glass surface (eq 15).

3.5 CONCLUSIONS

This work demonstrates the advantage of SECM-based nanogap voltammetry to assess the cleanness of a substrate electrode surface in solution by confirming that airborne contamination of the HOPG surface causes the non-ideal asymmetry of paired nanogap voltammograms of the $Fc^{2+/+}$ couple. In fact, symmetric pairs of nanogap voltammograms were obtained with the water-

protected HOPG surface, where airborne contamination was significantly suppressed.[15] In this study, the HOPG potential was cycled slowly at 0.05 V/s to address the ET kinetics with the minimal effect of Fc^+ adsorption on the HOPG surface, which was too weak to be quantitatively studied from the small hysteresis of the resultant nanogap voltammogram. Interestingly, SECM-based nanogap voltammetry will enable us to quantitatively study local Fc^+ adsorption on the HOPG surface by employing faster potential sweep rates, which requires the precise measurement of a sub-nA tip response at the sub-millisecond resolution without crosstalk with a sub-mA substrate response. Advantageously, SECM-based nanogap voltammetry is free from charging current,[4] which is a serious obstacle in the quantitative electrochemical study of surface adsorption[20] (e.g., Figure 3-6A).

We applied SECM-based nanogap voltammetry to estimate extremely high k^0 values of ≥12 cm/s for the outer-sphere ET reaction of the $Fc^{2+/+}$ couple at the water-protected HOPG surface. These k^0 values are much higher than those of 0.1−1 cm/s as estimated with the "pristine" HOPG surface,[33] which was exposed to ambient air during the whole kinetic measurement by scanning electrochemical cell microscopy.[34] Our k^0 values are still diffusion-limited minimum values, thereby requiring narrower tip–HOPG gaps of <50 nm to determine an actual k^0 value without a diffusion limit. Significantly, no Fc^{2+} adsorption on the HOPG surface excludes inner-sphere ET and electron-exchange pathways. A reliable outer-sphere redox couple will be useful to address various mechanistic questions about heterogeneous electron transfer including its adiabaticity.[36] By contrast, the outer-sphere character of a redox couple is often argued when its voltammogram is unaffected by the modification of the electrode surface with a molecularly thin film.[37] This approach is more general, but is inconclusive when a redox couple gives reversible

voltammograms at both modified and unmodified electrodes, because an actual k^0 value at the modified surface may be lower than at the unmodified surface.

Significantly, SECM-based nanogap voltammetry of the water-protected graphitic surface[15] will enable the study of ultrafast ET kinetics of various redox couples with a minimal effect from airborne contamination. Importantly, the ET kinetics of highly charged redox couples is seriously compromised by airborne contamination of graphitic surfaces,[38,39] which is inevitable with scanning electrochemical cell microscopy.[33] Water-protected HOPG surfaces are highly reactive to the $Fe(CN)_6^{3-/4-}$ couple, which yielded reversible CVs at 0.1 V/s for hours.[15] By contrast, McCreery and co-workers obtained various peak separations of 58–1200 mV at 0.2 V/s for the $Fe(CN)_6^{3-/4-}$ couple at the freshly exfoliated HOPG surface, which was immediately immersed in solution to prevent airborne contamination.[40] So far, we have not succeeded in obtaining the HOPG surface with extremely low reactivity, on which McCreery's work was focused.[41] Nevertheless, we believe that the study of the highly reactive HOPG surface is still significant, because it is not only complimentary to McCreery's seminal work, but also relevant to recent findings of high reactivity of graphitic nanomaterials such as graphene[42] and single-walled carbon nanotubes.[43,44]

3.6 SUPPORTING INFORMATION

3.6.1 Dimensionless model.

In this work, we employed an SECM configuration in the cylindrical coordinate (Figure 3-7) to simulate the nanogap voltammograms based on the dimensionless parameters defined as follows.

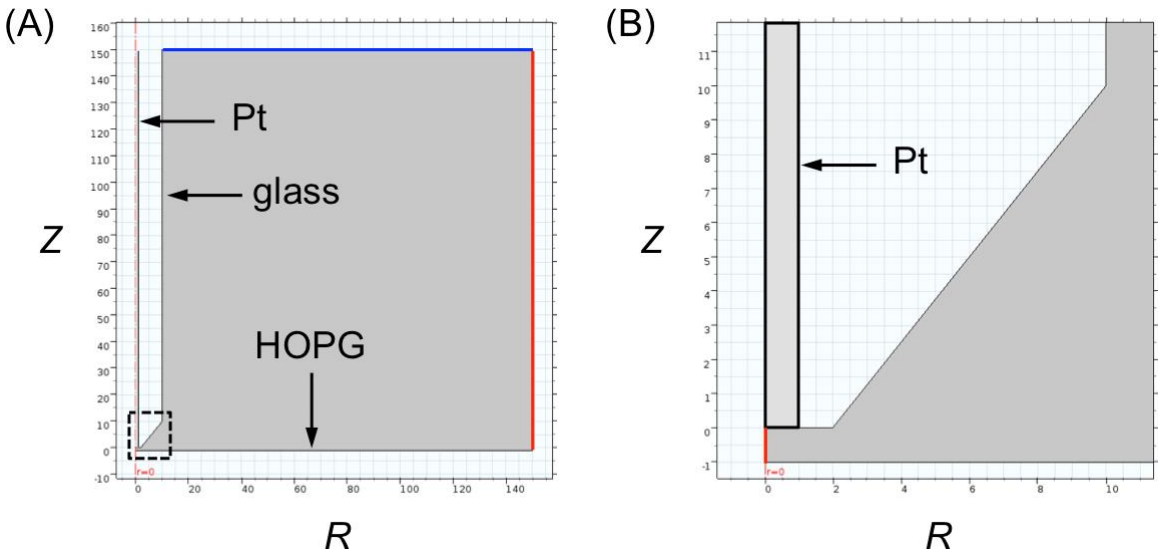

Figure 3-7. (A) Scheme of the SECM configuration employed in this study at $d = a$. Red boundaries show no normal flux. The blue boundary represents the bulk solution. Part (B) represents the region of part (A) surrounded by the dashed box.

Dimensionless forms of diffusion equations are given by

$$\frac{\partial C_{Fc^+}(R,Z,\tau)}{\partial \tau} = \left[\frac{\partial^2 C_{Fc^+}(R,Z,\tau)}{\partial R^2} + \frac{1}{R}\frac{\partial C_{Fc^+}(R,Z,\tau)}{\partial R} + \frac{\partial^2 C_{Fc^+}(R,Z,\tau)}{\partial Z^2} \right] \tag{28}$$

$$\frac{\partial C_{Fc^{2+}}(R,Z,\tau)}{\partial \tau} = \gamma \left[\frac{\partial^2 C_{Fc^{2+}}(R,Z,\tau)}{\partial R^2} + \frac{1}{R}\frac{\partial C_{Fc^{2+}}(R,Z,\tau)}{\partial R} + \frac{\partial^2 C_{Fc^{2+}}(R,Z,\tau)}{\partial Z^2} \right] \tag{29}$$

with

$$C_i(R,Z,\tau) = \frac{c_i(r,z,t)}{c_0} \tag{30}$$

$$R = \frac{r}{a} \tag{31}$$

$$Z = \frac{z}{a} \tag{32}$$

$$\tau = \frac{D_{Fc^+} t}{a^2} \tag{33}$$

$$\gamma = \frac{D_{Fc^{2+}}}{D_{Fc^+}} \tag{34}$$

Initial conditions are given by

$$C_{Fc^+}(R,Z,0) = 1 \tag{35}$$

$$C_{Fc^{2+}}(R,Z,0) = 0 \tag{36}$$

A boundary condition for Fc^{2+} at the HOPG surface is given by

$$g\left[\frac{\P C_{Fc^{2+}}(R,Z,t)}{\P Z} \right]_{Z=-L} = -/[q^{1-a} C_{Fc^+}(R,-L,t) - q^{-a} C_{Fc^{2+}}(R,-L,t)] \tag{37}$$

with

$$L = \frac{d}{a} \tag{38}$$

$$\lambda = \frac{a}{D_{Fc^+}} k^0 \tag{39}$$

$$q = \exp\left[\frac{F(E - E^{0'})}{RT}\right] \tag{40}$$

The substrate potential is cycled at the dimensionless sweep rate given by

$$\sigma = \frac{a^2 vF}{D_{Fc^+} RT} \tag{41}$$

A boundary condition for diffusing Fc^+ at the HOPG surface is given by

$$\left[\frac{\partial C_{Fc^+}(R,Z,t)}{\partial Z}\right]_{Z=-L} = l\,[q^{1-a} C_{Fc^+}(R,-L,t) - q^{-a} C_{Fc^{2+}}(R,-L,t)] - k_{HOPG}\left\{C_{Fc^+}(R,-L,t)[q_{Fc^+} - q_{Fc^+}(R,-L,t)] - \frac{q_{Fc^+}(R,-L,t)}{\Lambda_{HOPG}}\right\} \tag{42}$$

$$\kappa_{HOPG} = \frac{k_{ads}^{HOPG} a^2 c_0}{D_{Fc^+}} \tag{43}$$

$$\theta_{Fc^+} = \frac{\Gamma_{Fc^+}^{HOPG}}{ac_0} \tag{44}$$

$$q_{Fc^+}(R,Z,t) = \frac{\Gamma_{Fc^+}^{HOPG}(r,z,t)}{ac_0} \tag{45}$$

$$\Lambda_{HOPG} = c_0 b_{Fc^+}^{HOPG} \tag{46}$$

A boundary condition for Fc^+ adsorbed on the HOPG surface is given by

$$\left[\frac{\partial q_{Fc^+}(R,Z,t)}{\partial t}\right]_{Z=-L} = k_{HOPG}\left\{C_{Fc^+}(R,-L,t)[q_{Fc^+} - q_{Fc^+}(R,-L,t)] - \frac{q_{Fc^+}(R,-L,t)}{\Lambda_{HOPG}}\right\} \tag{47}$$

The initial condition for adsorbed Fc^+ is given by a Langmuir isotherm to yield

$$\theta_{Fc^+}(R,L,0)=\frac{\Lambda_{HOPG}}{1+\Lambda_{HOPH}}\theta_{Fc^+}^{HOPG} \tag{48}$$

Fc^{2+} adsorption on the glass sheath of a Pt tip yields a boundary condition for diffusing Fc^{2+} by using its dimensionless flux normal to the glass surface, $N_{Fc^{2+}}(R,Z,\tau)$, as

$$N_{Fc^{2+}}(R,Z,\tau)=-\kappa_{glass}\left\{C_{Fc^{2+}}(R,Z,\tau)\left[\theta_{Fc^{2+}}-\theta_{Fc^{2+}}(R,Z,\tau)\right]-\frac{\theta_{Fc^{2+}}(R,Z,\tau)}{\Lambda_{glass}}\right\} \tag{49}$$

where

$$\kappa_{glass}=\frac{k_{ads}^{glass}c_0a^2}{D_{Fc^+}} \tag{50}$$

$$\theta_{Fc^+}=\frac{\Gamma_{Fc^+}^{glass}}{ac_0} \tag{51}$$

$$q_{Fc^+}(R,Z,t)=\frac{\Gamma_{Fc^{2+}}^{glass}(r,z,t)}{ac_0} \tag{52}$$

$$L_{glass}=c_0b_{Fc^{2+}}^{glass} \tag{53}$$

In addition, the boundary condition for Fc^{2+} adsorbed on the glass surface is given by

$$\left[\frac{\partial q_{Fc^{2+}}(R,Z,t)}{\partial t}\right]=k_{glass}\left\{C_{Fc^{2+}}(R,Z,t)[q_{Fc^{2+}}-q_{Fc^{2+}}(R,Z,t)]-\frac{q_{Fc^{2+}}(R,Z,t)}{L_{glass}}\right\} \tag{54}$$

The initial condition for Fc^{2+} adsorbed on the glass surface is given by a Langmuir isotherm as

$$\theta_{Fc^+}(R,Z,0)=\frac{\Lambda_{glass}}{1+\Lambda_{glass}}\theta_{Fc^+} \tag{55}$$

Finally, the flux of Fc^+ normal to the glass surface is zero.

3.6.2 Bipotentiostat.

We modified both hardware and software of the commercial bipotentiostat to eliminate possible causes of tip damage. We ensured the connection of the bipotentiostat to the electrochemical cell not only by turning on the "cell-on-between-runs" function,[7] but also by removing the relay switches that were directly connected to the electrochemical cell.[30] In addition, we eliminated spike currents at the tip as well as click sounds, which were generated by turning on and off relay switches. Spike currents and click sounds were generated immediately before or after the cycle of the HOPG potential during an experimental run. Spike currents were detected by monitoring the analogue output of the tip current from the bipotentiostat with an oscilloscope. Actual tests were done by using 1 GΩ and 1 MΩ resisters as dummy tip and substrate, respectively.

The program commands that caused spike currents and click sounds were identified by inserting a breakpoint between consecutive commands to execute each command separately. Specifically, we revised or executed the program as follows to eliminate spike currents and click sounds.

(1) The original software transiently doubled the tip potential with respect to a target potential (e.g., 1.1 and 0.55 V, respectively), because the potential was set repetitively by using two D/A converters. The software was revised to use only one D/A converter.

(2) The substrate potential was instantaneously changed from the final potential of the last run (e.g., 0.15 V in the SG/TC mode) to the initial potential of the new run (e.g., 0.55 V in the feedback mode) so that a μA-level current flew transiently at the substrate to induce a current spike at the tip through crosstalk in the bipotentiostat. This problem was solved by changing the substrate potential stepwise with an increment of 10 mV. Similarly, the tip potential was changed stepwise with an increment of 10 mV.

(3) We disabled the static charge protection and automatic filter setting of the bipotentiostat. Optimum filters were found automatically and set manually before electrodes were connected to the bipotentiostat.

(4) We disabled the "S1" relay switch that selected the input of an A/D converter.

3.6.3 Identical Diffusion Coefficient of Fc^+ and Fc^{2+} as Determined by Nanogap Voltammetry.

The identical diffusion coefficient of Fc^+ and Fc^{2+} was determined from symmetric pairs of nanogap voltammograms at sufficiently long tip–HOPG distance, where the limiting current in the feedback mode was identical to the tip current in the bulk solution, $i_{T,\infty}$ (the bottom of Figure 3-8). Importantly, the tip–HOPG distance was still short enough to yield the limiting current in the SG/TC mode that was identical to $-i_{T,\infty}$. This result indicates that diffusion coefficients of Fc^+ and Fc^{2+} are identical.[4] Noticeably, the hysteresis of each nanogap voltammogram is consistent with the result of the finite element simulation that the forward wave is observed at more extreme potentials than the reverse wave, owing to the development of a time-dependent diffusion layer near the macroscopic substrate surface.[4]

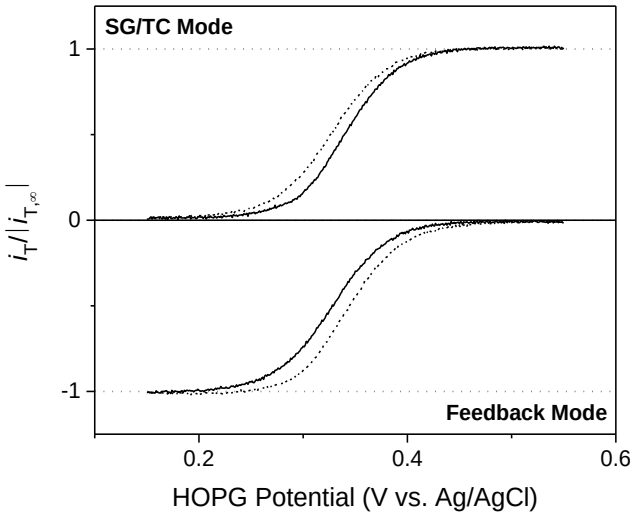

Figure 3-8. A symmetric pair of nanogap voltammograms of 0.3 mM Fc^+ in 50 mM KCl when a Pt tip was positioned just at the outside of the feedback distance from the non-protected HOPG surface. Forward and reverse waves are represented by solid and dashed lines, respectively.

3.6.4 Negligible Drift of the Tip–HOPG Distance.

We confirmed that the asymmetry of paired nanogap voltammograms was not due to the drift of the tip–HOPG distance. Two nanogap voltammograms in the same operation mode (e.g., the SG/TC mode in Figure 3-9) overlapped to each other very well when they were measured before and after a nanogap voltammogram was measured in the other operation mode (e.g., the feedback mode for Figure 3-3). This result confirms the negligible drift of the tip–HOPG distance during three consecutive cycles of the HOPG potential, which took ~1 minutes. The extremely stable nanogap was formed by using an isothermal chamber.[6]

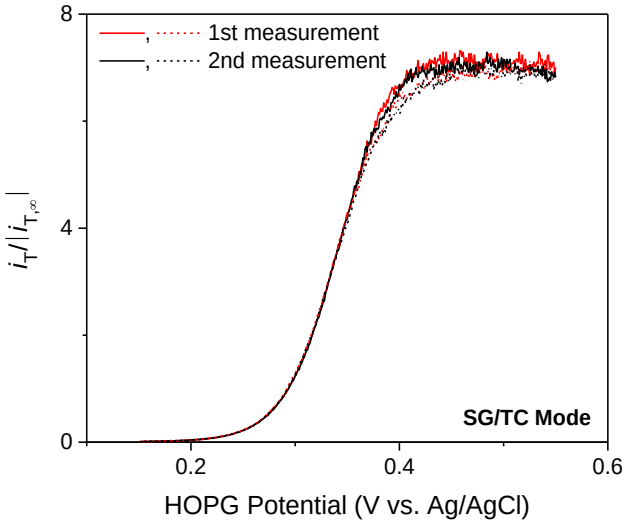

Figure 3-9. Nanogap voltammograms of 0.3 mM Fc^+ in 50 mM KCl at the water-protected HOPG surface as measured in the SG/TC mode before and after a nanogap voltammogram was measured in the feedback mode. Forward and reverse waves are represented by solid and dashed lines, respectively.

3.6.5 Analysis of Nanogap Voltammograms.

Nanogap voltammograms of the $Fc^{2+/+}$ couple at airborne-contaminated and water-protected HOPG surfaces (e.g., Figures 3-4 and 3-5, respectively) were analyzed to yield parameters listed in Table 3-1. Nanogap voltammograms of Fc^{2+} reduction at the HOPG surface in the feedback mode were fitted to the following equation[4]

$$\frac{i_T}{i_{T,\infty}} = \frac{p}{4xL\left(q + q^a / LI + 1\right)} + \frac{1}{q+1}\left(\frac{i_T^{PF}}{i_{T,\infty}} - \frac{p}{4xL}\right) \qquad (56)$$

where i_T^{PF} is the positive feedback current at the same distance and corresponds to the limiting

current of the nanogap voltammogram. On the other hand, nanogap voltammograms of Fc^+ oxidation at the HOPG surface in the SG/TC mode were fitted to the following equation[4]

$$\frac{i_T}{i_{T,\infty}} = \frac{p}{4xL\left(1/q + q^{a-1}/L/ + 1\right)} + \frac{q}{q+1}\left(\frac{i_T^{PF}}{i_{T,\infty}} - \frac{p}{4xL}\right) \quad (57)$$

The Tip–HOPG distances were determined from i_T^{PF} values by using the approximate equation given in ref. 45.

3.6.6 Analysis of CVs of Weak Fc^+ Adsorption on the HOPG Surface.

We analyzed CVs of the $Fc^{2+/+}$ couple (e.g., Figures 3-6 for water-protected HOPG) to demonstrate weak Fc^+ adsorption on the HOGP surface. First, the CV of Fc^+ at 0.1 V/s was fitted with a reversible CV simulated without Fc^+ adsorption on the HOPG surface to determine the area of the HOPG surface, A, exposed to the electrolyte solution in the sealed SECM cell (Figure 3-10A). Then, the CV of Fc^+ at 10 V/s was compared with an adsorption-free reversible CV simulated with the same surface area and interfacial capacitance to subtract the latter CV from the former CV. The forward wave of the subtracted CV (Figure 3-10B) was integrated to estimate the charge based on the oxidation of Fc^+ adsorbed initially on the HOPG surface, Q_{Fc^+}. Subsequently, we obtained the initial surface concentration of adsorbed Fc^+ as

$$\Gamma_{Fc^+} = \frac{Q_{Fc^+}}{FA} \tag{58}$$

Specifically, we obtained $\Gamma_{Fc^+} = (2.7 \pm 0.6) \times 10^{-11}$ mol/cm^2 for water-protected HOPG and $(2.4 \pm 0.3) \times 10^{-11}$ mol/cm^2 for non-protected HOPG. The respective values correspond to $L_{HOPG} = 0.06 \pm 0.01$ and 0.050 ± 0.006 in eq S-21 with $\Gamma_{Fc^+}^{HOPG} = 5 \times 10^{-10}$ mol/cm^2.[16] Finally, eq S-19 with $c_0 = 0.3$ mM yields $b_{Fc^+}^{HOPG}$ values of $(1.8 \pm 0.4) \times 10^5$ cm^3/mol ($N = 5$) and $(1.7 \pm 0.2) \times 10^5$ cm^3/mol ($N = 3$) at water-protected and non-protected HOPG surfaces, respectively.

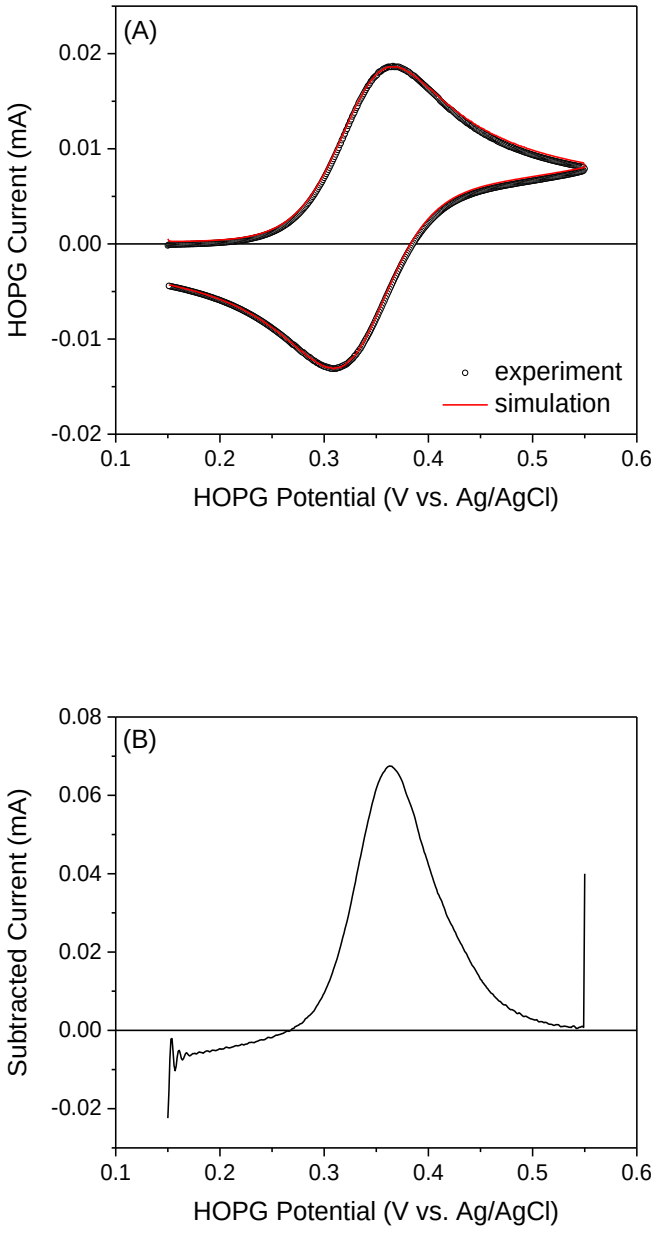

Figure 3-10. (A) Experimental and simulated CVs of 0.3 mM Fc^+ in 50 mM KCl with water-protected HOPG. Potential sweep rate, 0.1 V/s. (B) The forward wave of an experimental CV at 10 V/s after the subtraction of a simulated CV. See the inset of Figure 3-6A for forward waves of original experimental and simulated CVs.

Noticeably, we obtained smaller $b_{Fc^+}^{HOPG}$ values of (8 ± 4) × 10^4 and (6 ± 3) × 10^4 cm^3/mol for water-protected and non-protected HOPG surfaces, respectively, from differences between experimental and simulated anodic peak currents, Δi_p, which relied on CVs at slower potential sweep rates as proposed by Unwin and co-workers[19] in contrast to the aforementioned analysis. Specifically, Δi_p corresponds to the forward peak current of a subtracted CV (Figure 3-10B), but somehow varies non-linearly with the potential sweep rate to fit with a quadratic equation[19] (Figure 3-11). A Γ_{Fc^+} value was determined from the coefficient of the first-order term,[19] which emphasized Δi_p values at slow potential sweep rates. The Γ_{Fc^+} value was used to calculate a $b_{Fc^+}^{HOPG}$ value by using eqs 46 and 48.

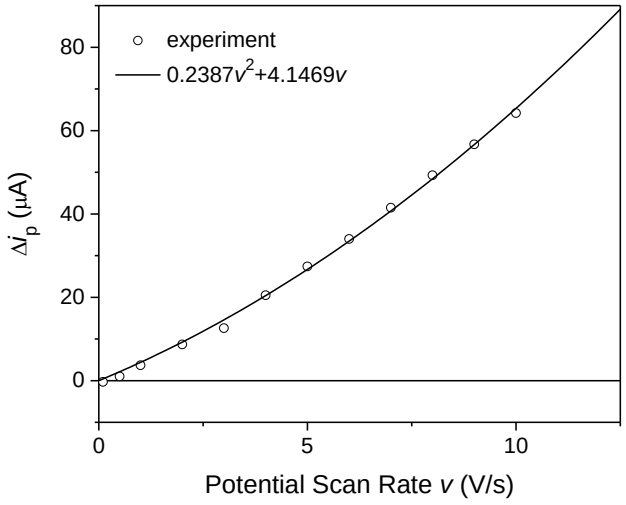

Figure 3-11. A plot of Δi_p versus v (open circles) from CVs of 0.3 mM Fc^+ at the water-protected HOPG surface in 50 mM KCl and a theoretical fit (solid line).

3.6.7 Derivation of Eqs 23 and 24.

We employ Nernst equations to obtain eqs 23 and 24 for inner-sphere and electron-exchange pathways at the HOPG surface, respectively. A Nernst equation is given for the inner-sphere pathway based on co-adsorption of Fc^+ and Fc^{2+} as[46]

$$\frac{\Gamma^{HOPG}_{Fc^{2+}}(r,-d,t)}{\Gamma^{HOPG}_{Fc^{+}}(r,-d,t)} = \left(\frac{\Gamma^{HOPG}_{Fc^{2+}}\beta^{HOPG}_{Fc^{2+}}}{\Gamma^{HOPG}_{Fc^{+}}\beta^{HOPG}_{Fc^{+}}}\right)\exp\left[\left(\frac{F}{RT}\right)(E-E^{0'})\right] \tag{59}$$

The logarithm of eq 59 yields

$$E = E^{0'} - \frac{RT}{F}\frac{\Gamma^{HOPG}_{Fc^{2+}}\beta^{HOPG}_{Fc^{2+}}}{\Gamma^{HOPG}_{Fc^{+}}\beta^{HOPG}_{Fc^{+}}} - \frac{RT}{F}\ln\frac{\Gamma^{HOPG}_{Fc^{+}}(r,-d,t)}{\Gamma^{HOPG}_{Fc^{2+}}(r,-d,t)} \tag{60}$$

which must be equivalent to

$$E = E^{0¢}_{ads} - \frac{RT}{F}\ln\frac{G^{HOPG}_{Fc^{+}}(r,-d,t)}{G^{HOPG}_{Fc^{2+}}(r,-d,t)} \tag{61}$$

A comparison of eq 61 with eq 60 yields eq 23.

A Nernst equation is defined for the outer-sphere pathway by

$$E = E^{0¢} - \frac{RT}{F}\ln\frac{c_{Fc^{+}}(r,-d,t)}{c_{Fc^{2+}}(r,-d,t)} \tag{62}$$

which is equivalent to

$$\frac{c_{Fc^{2+}}(r,-d,t)}{c_{Fc^{+}}(r,-d,t)} = \exp\left[\left(\frac{F}{RT}\right)(E-E^{0'})\right] \tag{63}$$

Eq 59 was divided by eq 63 to yield

$$\frac{\Gamma^{HOPG}_{Fc^{2+}}(r,-d,t)c_{Fc^{+}}(r,-d,t)}{\Gamma^{HOPG}_{Fc^{+}}(r,-d,t)c_{Fc^{2+}}(r,-d,t)} = \left(\frac{\Gamma^{HOPG}_{Fc^{2+}}\beta^{HOPG}_{Fc^{2+}}}{\Gamma^{HOPG}_{Fc^{+}}\beta^{HOPG}_{Fc^{+}}}\right) \tag{64}$$

The left-hand side of eq 64 was defined as K_{ex}^{HOPG} to yield eq 24.

3.6.8 Derivation of Eqs 25.

We consider co-adsorption of Fc^{+} and Fc^{2+} on the glass surface based on a Langmuir isotherm to yield eq 25. Specifically, concentrations of Fc^{+} and Fc^{2+} adsorbed on the glass surface are given by[47]

$$\Gamma_{Fc^{2+}}^{glass}(r,z,t)=\frac{\Gamma_{Fc^{2+}}^{glass}\beta_{Fc^{2+}}^{glass}c_{Fc^{2+}}(r,z,t)}{1+\beta_{Fc^{2+}}^{glass}c_{Fc^{2+}}(r,z,t)+\beta_{Fc^{+}}^{glass}c_{Fc^{+}}(r,z,t)} \tag{65}$$

$$\Gamma_{Fc^{+}}^{glass}(r,z,t)=\frac{\Gamma_{Fc^{+}}^{glass}\beta_{Fc^{+}}^{glass}c_{Fc^{+}}(r,z,t)}{1+\beta_{Fc^{2+}}^{glass}c_{Fc^{2+}}(r,z,t)+\beta_{Fc^{+}}^{glass}c_{Fc^{+}}(r,z,t)} \tag{66}$$

Eq 66 was divided by eq 65 to yield

$$\frac{\Gamma_{Fc^{+}}^{glass}(r,z,t)}{\Gamma_{Fc^{2+}}^{glass}(r,z,t)}=\frac{\Gamma_{Fc^{+}}^{glass}\beta_{Fc^{+}}^{glass}c_{Fc^{+}}(r,z,t)}{\Gamma_{Fc^{2+}}^{glass}\beta_{Fc^{2+}}^{glass}c_{Fc^{2+}}(r,z,t)} \tag{67}$$

Eq 67 was rearranged to

$$\frac{\Gamma_{Fc^{+}}^{glass}(r,z,t)c_{Fc^{2+}}(r,z,t)}{\Gamma_{Fc^{2+}}^{glass}(r,z,t)c_{Fc^{+}}(r,z,t)}=\frac{\Gamma_{Fc^{+}}^{glass}\beta_{Fc^{+}}^{glass}}{\Gamma_{Fc^{2+}}^{glass}\beta_{Fc^{2+}}^{glass}} \tag{68}$$

The left-hand side of eq 68 was defined as K_{ex}^{glass} to yield eq 25.

ACKNOWLEDGEMENTS

This work was supported by the National Science Foundation (CHE 1608703). We thank Professor Christian Amatore and Professor Richard L. McCreery for helpful comments on ET pathways and HOPG electrochemistry, respectively. We also thank Dr. Peixin He for modification of the bipotentiostat and its software as well as Prof. Allen J. Bard and Dr. Jiyeon Kim for their advice on the need of its hardware modification.

3.7 REFERENCES

(1) Amemiya, S.; Bard, A. J.; Fan, F.-R. F.; Mirkin, M. V.; Unwin, P. R. *Annu. Rev. Anal. Chem.* **2008**, *1*, 95.

(2) Amemiya, S. Scanning Electrochemical Microscopy of Nnaopores, Nanocarbons, and Nanoparticles. In *Nanoelectrochemistry*; Mirkin, M. V., Amemiya, S., Eds.; Taylor and Francis: Boca Raton, FL, 2015; p 621.

(3) Amemiya, S. Nanoscale Scanning Electrochemical Microscopy. In *Electroanalytical Chemistry*; Bard, A. J., Zoski, C. G., Eds.; Taylor and Francis: Boca Raton, FL, 2016; Vol. 26, p 1.

(4) Nioradze, N.; Kim, J.; Amemiya, S. *Anal. Chem.* **2011**, *83*, 828.

(5) Amemiya, S.; Nioradze, N.; Santhosh, P.; Deible, M. J. *Anal. Chem.* **2011**, *83*, 5928.

(6) Kim, J.; Shen, M.; Nioradze, N.; Amemiya, S. *Anal. Chem.* **2012**, *84*, 3489.

(7) Nioradze, N.; Chen, R.; Kim, J.; Shen, M.; Santhosh, P.; Amemiya, S. *Anal. Chem.* **2013**, *85*, 6198.

(8) Chen, R.; Hu, K.; Yu, Y.; Mirkin, M. V.; Amemiya, S. *J. Electrochem. Soc.* **2016**, *163*, H3032.

(9) Slevin, C. J.; Gray, N. J.; Macpherson, J. V.; Webb, M. A.; Unwin, P. R. *Electrochem. Commun.* **1999**, *1*, 282.

(10) Actis, P.; Tokar, S.; Clausmeyer, J.; Babakinejad, B.; Mikhaleva, S.; Cornut, R.; Takahashi, Y.; Cordoba, A. L.; Novak, P.; Shevchuck, A. I.; Dougan, J. A.; Kazarian, S. G.; Gorelkin, P. V.; Erofeev, A. S.; Yaminsky, I. V.; Unwin, P. R.; Schuhmann, W.; Klenerman, D.; Rusakov, D. A.; Sviderskaya, E. V.; Korchev, Y. E. *Acs Nano* **2014**, *8*, 875.

(11) Nioradze, N.; Chen, R.; Kurapati, N.; Khvataeva-Domanov, A.; Mabic, S.; Amemiya, S. *Anal. Chem.* **2015**, *87*, 4836.

(12) McCreery, R. L. *Chem. Rev.* **2008**, *108*, 2646.

(13) Li, Z.; Wang, Y.; Kozbial, A.; Shenoy, G.; Zhou, F.; McGinley, R.; Ireland, P.; Morganstein, B.; Kunkel, A.; Surwade, S. P.; Li, L.; Liu, H. *Nat. Mater.* **2013**, *12*, 925.

(14) Kozbial, A.; Li, Z.; Sun, J.; Gong, X.; Zhou, F.; Wang, Y.; Xu, H.; Liu, H.; Li, L. *Carbon* **2014**, *74*, 218.

(15) Li, Z.; Kozbial, A.; Nioradze, N.; Parobek, D.; Shenoy, G. J.; Salim, M.; Amemiya, S.; Li, L.; Liu, H. *ACS Nano* **2016**, *10*, 349.

(16) Tan, S.-Y.; Zhang, J.; Bond, A. M.; Macpherson, J. V.; Unwin, P. R. *Anal. Chem.* **2016**, *88*, 3272.

(17) Klymenko, O. V.; Svir, I.; Amatore, C. *Mol. Phys.* **2014**, *112*, 1273.

(18) Klymenko, O. V.; Buriez, O.; Labbe, E.; Zhan, D. P.; Rondinini, S.; Tian, Z. Q.; Svir, I.; Amatore, C. *ChemElectroChem* **2014**, *1*, 227.

(19) Cuharuc, A. S.; Zhang, G.; Unwin, P. R. *Phys. Chem. Chem. Phys.* **2016**, *18*, 4966.

(20) Laviron, E. Voltammetric Methods for the Study of Adsorbed Species. In *Electroanalytical Chemistry*; Bard, A. J., Ed.; Marcel Dekker: New York, 1982; Vol. 12, p 53.

(21) Shoup, D.; Szabo, A. *J. Electroanal. Chem.* **1984**, *160*, 27.

(22) Kwak, J.; Bard, A. J. *Anal. Chem.* **1989**, *61*, 1221.

(23) Zoski, C. G.; Aguilar, J. C.; Bard, A. J. *Anal. Chem.* **2003**, *75*, 2959.

(24) Eckhard, K.; Chen, X. X.; Turcu, F.; Schuhmann, W. *Phys. Chem. Chem. Phys.* **2006**, *8*, 5359.

(25) Bard, A. J.; Faulkner, L. R. *Electrochemical Methods: Fundamentals and Applications*; 2nd ed.; John Wiley & Sons: New York, 2001, p. 92.

(26) Klymenko, O. V.; Svir, I.; Amatore, C. *J. Electroanal. Chem.* **2013**, *688*, 320.

(27) Bard, A. J.; Faulkner, L. R. *Electrochemical Methods: Fundamentals and Applications*; 2nd ed.; John Wiley & Sons: New York, 2001, p. 566.

(28) Kim, J.; Izadyar, A.; Nioradze, N.; Amemiya, S. *J. Am. Chem. Soc.* **2013**, *135*, 2321.

(29) Kim, J.; Kim, B.-K.; Cho, S. K.; Bard, A. J. *J. Am. Chem. Soc.* **2014**, *136*, 8173.

(30) Kim, J.; Renault, C.; Nioradze, N.; Arroyo-Currás, N.; Leonard, K. C.; Bard, A. J. *J. Am. Chem. Soc.* **2016**, *138*, 8560.

(31) Marcus, R. A. *J. Chem. Phys.* **1965**, *43*, 679.

(32) Nielson, R. M.; McManis, G. E.; Weaver, M. J. *J. Phys. Chem.* **1989**, *93*, 4703.

(33) Lai, S. C. S.; Patel, A. N.; McKelvey, K.; Unwin, P. R. *Angew. Chem. Int. Ed.* **2012**, *51*, 5405.

(34) Snowden, M. E.; Guell, A. G.; Lai, S. C. S.; McKelvey, K.; Ebejer, N.; O'Connell, M. A.; Colburn, A. W.; Unwin, P. R. *Anal. Chem.* **2012**, *84*, 2483.

(35) Wopschall, R. H.; Shain, I. *Anal. Chem.* **1967**, *39*, 1514.

(36) Royea, W. J.; Hamann, T. W.; Brunschwig, B. S.; Lewis, N. S. *J. Phys. Chem. B* **2006**, *110*, 19433.

(37) Bard, A. J. *J. Am. Chem. Soc.* **2010**, *132*, 7559.

(38) Velický, M.; Bradley, D. F.; Cooper, A. J.; Hill, E. W.; Kinloch, I. A.; Mishchenko, A.; Novoselov, K. S.; Patten, H. V.; Toth, P. S.; Valota, A. T.; Worrall, S. D.; Dryfe, R. A. W. *ACS Nano* **2014**, *8*, 10089.

(39) Velický, M.; Bissett, M. A.; Toth, P. S.; Patten, H. V.; Worrall, S. D.; Rodgers, A. N. J.; Hill, E. W.; Kinloch, I. A.; Novoselov, K. S.; Georgiou, T.; Britnell, L.; Dryfe, R. A. W. *Phys. Chem. Chem. Phys.* **2015**, *17*, 17844.

(40) Kneten, K. R.; McCreery, R. L. *Anal. Chem.* **1992**, *64*, 2518.

(41) McCreery, R. L.; McDermott, M. T. *Anal. Chem.* **2012**, *84*, 2602.

(42) Chen, R.; Nioradze, N.; Santhosh, P.; Li, Z.; Surwade, S. P.; Shenoy, G. J.; Parobek, D. G.; Kim, M. A.; Liu, H.; Amemiya, S. *Angew. Chem. Int. Ed.* **2015**, *54*, 15134.

(43) Heller, I.; Kong, J.; Heering, H. A.; Williams, K. A.; Lemay, S. G.; Dekker, C. *Nano Lett.* **2005**, *5*, 137.

(44) Kim, J.; Xiong, H.; Hofmann, M.; Kong, J.; Amemiya, S. *Anal. Chem.* **2010**, *82*, 1605.

(45) Cornut, R.; Lefrou, C. *J. Electroanal. Chem.* **2008**, *621*, 178.

(46) Bard, A. J.; Faulkner, L. R. *Electrochemical Methods: Fundamentals and Applications*; 2nd ed.; John Wiley & Sons: New York, 2001, p. 590.

(47) Bard, A. J.; Faulkner, L. R. *Electrochemical Methods: Fundamentals and Applications*; 2nd ed.; John Wiley & Sons: New York, 2001, p. 589.

4.0 FOCUSED-ION-BEAM-MILLED CARBON NANOELECTRODES FOR SCANNING ELECTROCHEMICAL MICROSCOPY

This work has been published as Chen. R.; Hu, K.; Yu, Y.; Mirkin, M. V.; Amemiya, S., Focused-Ion-Beam-Milled Carbon Nanoelectrodes for Scanning Electrochemical Microscopy, *J. Electrochem. Soc.* **2016**, *163*, H3032-H3037. The thesis author fabricated electrodes by Focused-Ion-Beam, collected and analyzed experimental data.

4.1 INTRODUCTION

The development of nanometer-sized carbon electrodes is pivotal for various electrochemical applications including scanning electrochemical microscopy (SECM)[1,2]. Originally, carbon nanoelectrodes were fabricated by exposing the sharp tip of an etched carbon fiber from an insulating sheath. Flame-etched carbon nanoelectrodes[3,4] were developed to detect neurotransmitters released from single vesicles at single cells[5] and synapses[6]. Electrochemically etched carbon nanoelectrodes[7] were employed as non-catalytic conductive supports of single platinum nanoparticles to study their electrocatalytic activities[8]. Etched carbon-fiber nanoelectrodes, however, yielded only low SECM feedback responses[9] because of the conical tip geometry[10,11]. Alternatively, disk-shaped carbon nanoelectrodes[12] were developed by pyrolytic deposition of carbon[13]. Heat-pulled quartz nanopipets were filled with pyrolytic carbon for single-cell imaging[14-16] and were further modified with platinum for intracellular oxygen monitoring[17],

iridium oxide for pH mapping[18], or mercury for stripping voltammetry of lithium ion[19]. Pyrolytic carbon nanoelectrodes, however, demonstrated low feedback responses that poorly fit with SECM theory for inlaid disk tips[14-17].

Recently, selective chemical vapor deposition (CVD) of carbon in quartz nanopipets enabled the development of carbon nanoelectrodes with controlled geometries[20,21]. With this method, carbon is deposited more readily on the inner wall of a nanopipet than on its outer wall, because carbon sources (e.g., methane) are effectively trapped in the tapered nanopipet to ensure their frequent collision with the inner wall for carbon deposition[22]. Moreover, a precise amount of carbon can be deposited by adjusting the duration of the CVD process to control the tip geometry. Short deposition results in the coating of the inner wall of a nanopipet with a thin carbon film, producing a carbon nanopipet that can be filled with an electrolyte solution for resistive-pulse sensing[23]. Long deposition completely fills a nanopipet with carbon, with the exception of the tip, which was used as a nanocavity for sampling attoliter-to-picoliter volumes of electrolyte solutions[24] or was platinized for oxygen sensing[25]. Longer deposition yields a slightly protruded carbon tip to support single gold nanoparticles for the study of their electrocatalytic activity[26].

Here, we report on CVD-based carbon nanoelectrodes with high electrochemical reactivity and well-controlled size and geometry for nanoscale SECM[27] to enable reliable and quantitative nanoelectrochemical measurements. The intrinsically high electrochemical reactivity of CVD carbon[24-26] is advantageous to electrolyze efficiently a redox species under the extremely high mass-transport conditions of nanoscale SECM. Geometrically, the thin quartz sheath of nanopipet-supported CVD carbon facilitates the close approach of its nanotip to the surface of a target substrate without a tip–substrate contact, which is a prerequisite for enhanced spatial and kinetic resolution of nanoscale SECM. The tip of nanopipet-supported CVD carbon, however, is not

sufficiently flat because of the nanoscale protrusion or recession of carbon from the quartz sheath and the nanoscale roughness of both carbon and quartz tips. Mechanical polishing can smoothen successfully only the extremely small tips of CVD-carbon-filled nanopipets with radii of <5 nm, which were too small for SECM-based characterization[26].

In this work, we mill the tips of CVD-carbon-filled quartz nanopipets by focused ion-beam (FIB) technology[28,29] in order to yield inner and outer tip radii of down to ~27 and ~38 nm, respectively. Advantageously, the thin quartz sheath allows for high-resolution transmission electron microscopy (TEM) imaging of the flat and sharp carbon nanotips. The geometry of FIB-milled carbon nanotips is well-controlled not only to quantitatively assess their remarkably high electrochemical reactivity, but also to yield high feedback responses in SECM approach curve measurements in contrast to previously reported carbon nanotips[9,14-17]. Good agreement between experimental and simulated approach curves at SiO_2-coated silicon wafers reliably confirms the well-characterized tip geometry and size, and a lack of a conductive carbon film on the outer tip wall. Moreover, an approach curve at a gold-coated silicon wafer shows a higher positive feedback response as the concentration of a redox mediator is lowered, thereby revealing the limited conductivity of the thin gold film under high mass-transport conditions across carbon–gold nanogaps. Importantly, we enabled reliable and quantitative nanoelectrochemical measurements by protecting carbon nanotips from nanoscale electrostatic damage[30,31], unlike the recent study of pyrolytic carbon nanoelectrodes[17].

4.2 THEORY

Here, we simulate SECM approach curves for a disk-shaped tip with a conductive outer

wall for the first time to find that feedback responses are useful to assess the conductivity of the outer wall. In our model, the unbiased outer wall that is disconnected from the conductive tip serves as a bipolar electrode[32], where the product of a tip reaction, R, is electrolyzed to an original redox species, O, to affect the tip current not only in the bulk solution, but also near substrates in the SECM feedback mode (Figure 4-1A). Noticeably, only the substrate generation/tip collection mode was considered in a previous study of the SECM tip with a conductive outer wall to improve spatial resolution[33]. Specifically, we simulate the amperometric response of a disk-shaped SECM tip with a conductive or insulating outer wall for a comparison. The corresponding steady-state diffusion problem was defined in a cylindrical coordinate as

$$\frac{\partial c(r,z)}{\partial t} = D\left[\frac{\partial^2 c(r,z)}{\partial r^2} + \frac{1}{r}\frac{\partial c(r,z)}{\partial r} + \frac{\partial^2 c(r,z)}{\partial z^2}\right] \quad (1)$$

where $c(r,z)$ and D are the concentration and diffusion coefficient of the original redox species, O, respectively. Only the original redox species is initially present in the bulk solution and is electrolyzed at the tip at a diffusion-limited rate to yield a boundary condition at the tip as

$$c(r,z) = 0 \quad (2)$$

Alternatively, the Butler–Volmer model is employed to simulate a voltammogram at a carbon nanotip in the bulk solution. The electrolysis of the tip-generated species, R, to the original redox species, O, at the large surface of a conductive outer wall is also driven at a diffusion-limited rate (34) as given by

$$c(r,z) = c_0 \quad (3)$$

where c_0 is the bulk concentration of the original redox species. This boundary condition is also applied for a conductive substrate and simulation space limits. Finally, no redox reaction occurs at the insulating sheath of a tip, where a boundary condition is given by zero normal flux. This boundary condition is also applicable to an insulating substrate and the symmetry axis. This two-

dimensional diffusion problem was solved by employing the COMSOL Multiphysics finite element package (version 3.5a, COMSOL, Burlington, MA) to calculate the tip current, i_T, at various tip–substrate distances, d. In the following, simulation results are reported for the geometry of FIB-milled carbon nanotips with a tip angle, θ, of 5˚ and a ratio, RG, of 1.4 between outer and inner tip radii (a and r_g, respectively), as determined by TEM (see below).

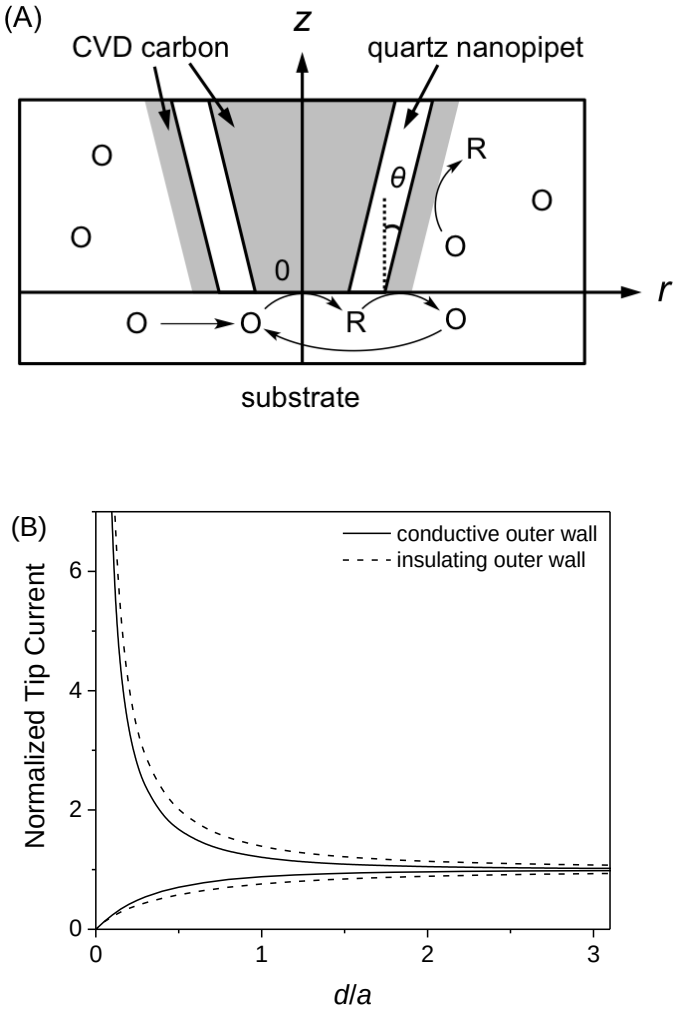

Figure 4-1. (A) Scheme of redox reactions at the tip and the conductive outer wall as defined in the cylindrical coordinate for simulation of SECM approach curves. (B) Approach

curves simulated for a disk-shaped tip with a conductive and insulating outer wall ($\theta = 5^{\circ}$ and RG = 1.4). The tip current was normalized against different $i_{T,\infty}$ values for a conductive and insulating outer wall (see eq 4).

The simulated approach curves at the conductive and insulating substrate clearly demonstrate that feedback responses significantly depend on the conductivity of the outer tip wall (Figure 4-1B). In these approach curves, the tip–substrate distance, d, is normalized against the inner tip radius, a, while the tip current is normalized against the tip current in the bulk solution, $i_{T,\infty}$. As expected, our simulation results demonstrate that $i_{T,\infty}$ also depends on the conductivity of the outer wall as given by

$$i_{T,\infty} = 4xnFDc_0a \qquad (4)$$

where x = 1.37 and 1.13 for the conductive and insulating outer wall with $\theta = 5^{\circ}$ and RG = 1.4, respectively. A significantly larger x value for a conductive outer wall indicates that a significant fraction of the tip-generated species is electrolyzed at the wall to regenerate the original redox species for the tip reaction (Figure 4-1A). Subsequently, a lower positive feedback response is expected when a tip with a conductive outer wall approaches a conductive substrate, where a smaller fraction of the tip-generated species is available for the regeneration of the original redox species. Similarly, a less negative feedback effect is expected for a nanotip with a conductive outer wall, which regenerates the original species to enhance the tip current. Noticeably, the effect of a conductive outer wall on the tip current becomes smaller for a thicker quartz sheath.

4.3 EXPERIMENTAL SECTION

4.3.1 Chemicals and Materials.

$Ru(NH_3)_6Cl_3$ was obtained from Strem Chemicals (Newburyport, MA). SiO_2-coated silicon wafers were obtained from Graphene Laboratories (Calverton, NY). Silicon wafers coated with a 5.0 nm-thick titanium adhesion layer and then with a 100 nm-thick gold layer were obtained from Platypus Technologies (Madison, WI). All sample solutions were prepared by using ultrapure water with total organic carbon (TOC) of ≤1 ppb[35], which was obtained by passing the final product of the Milli-Q Advantage A10 system (EMD Millipore, Billerica, MA) through a specific activated-carbon filter (VOC Pak, EMD Millipore). The Milli-Q water purification system was equipped with a Q-Gard T1 pack and a Quantum TEX cartridge (EMD Millipore) in order to produce ultrapure water with 18.2 MΩ·cm and TOC of 3 ppb. The Milli-Q system was fed with purified tap water (15.0 MΩ·cm) as obtained by using the Elix 3 Advantage system (EMD Millipore).

4.3.2 Tip Fabrication and Characterization.

A nanopipet was heat-pulled from a quartz capillary (1.0 mm outer diameter and 0.7 mm inner diameter, Sutter Instrument, Novato, CA) and filled with carbon by CVD to yield a slightly recessed tip[24]. Specifically, a nanopipet with a tip diameter of 10–100 nm was pulled by using a program based on HEAT = 800, FIL = 4, VEL = 22, DEL = 128, PUL = 110 and HEAT = 830, FIL = 3, VEL = 17, DEL = 130, PUL = 255. A nanopipet was nearly completely filled with carbon deposited from methane in argon (1:1 ratio) for 1 hour at 900 °C. A copper nickel wire (0.13 mm

diameter, Alfa Aesar, Ward Hill, PA) was used to establish a connection with a carbon nanotip for electrochemical measurements as well as its grounding to a sample stage in TEM, scanning electron microscopy (SEM), and FIB experiments and for protections from electrostatic damage. A recessed tip was milled by using an FIB instrument (SMI3050SE FIB-SEM, Seiko Instruments, Chiba, Japan)[28,29] to yield a flat tip as confirmed by TEM (JEM-2100, JEOL USA, Peabody, MA)[36]. The beam of gallium ion (30 keV and 10 pA) was focused at a carbon nanotip for ~3 second to mill the tip end, whereas the prior adjustment of the FIB condition took several minutes. A carbon nanotip was also characterized by SEM with the dual-beam FIB instrument before and after milling.

4.3.3 Electrochemical Measurements.

A homebuilt SECM instrument[37] was used for electrochemical measurements with CVD carbon nanotips. A patch-clamp amplifier (Chem-Clamp, Dagan, Minneapolis, MN) was used as a two-electrode potentiostat to prevent the electrochemical damage of a nanotip[30]. A Ag/AgCl wire was used as a counter/reference electrode. SiO_2- and Au-coated silicon wafers were cleaned in piranha solution (a 1:3 mixture of 30% H_2O_2 and 95.0–98.0% H_2SO_4) for 90 minutes and in Milli-Q water for 15 minutes (3 times), and immediately immersed into the electrolyte solution contained in an SECM cell (Caution: piranha solution reacts violently with organics and should be handled with extreme care!). The electrolyte solution was prepared by dissolving $Ru(NH_3)_6Cl_3$ in phosphate buffer solution (PBS) at pH 7.4 containing 0.137 M NaCl, 0.0027 M KCl, 0.01 M Na_2HPO_4, and 0.0018 M KH_2PO_4. The SECM cell was cleaned and sealed using a rubber cap and silicon gaskets in order to prevent the contamination of the electrolyte solution with airborne

organic impurities[35]. When a tip was attached to the SECM stage, the perpendicular alignment of the tip's axis with respect to the substrate surface was confirmed within ±0.5˚ by using a digital angle gauge.

4.4 RESULTS AND DISCUSSION

4.4.1 TEM, SEM and FIB Imaging.

CVD carbon nanoelectrodes were characterized by TEM, SEM, and FIB imaging before and after FIB milling. We selected a CVD condition to obtain a recessed tip without the formation of a conductive carbon film on the outer tip wall[24]. The high-resolution TEM image of an unmilled carbon nanotip confirmed the ~70 nm-depth recession of CVD carbon from the ~20 nm-radius orifice of the heat-pulled quartz pipet (Figure 4-2A). The hemispherical tip of CVD carbon had a base radius of ~60 nm and was surrounded by a ~25 nm-thick quartz wall, which corresponds to an *RG* value of ~1.4 as expected from the corresponding *RG* value of quartz capillaries. A recessed carbon nanotip was milled by FIB and imaged by TEM to confirm that the tip was flat and completely filled with CVD carbon to yield an outer tip radius of ~75 nm (Figure 4-2B). The excellent smoothness of a FIB-milled tip was achieved by employing a low current gallium ion (Ga^+) beam (10 pA at 30 keV). Noticeably, TEM images showed that the edge of the milled tips was rounded, which is ascribed to the Gaussian broadening of the focused Ga^+ beam[38].

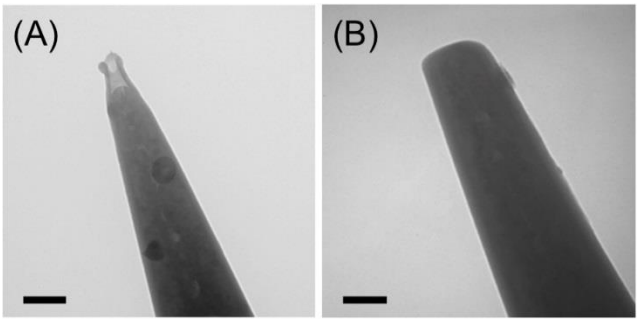

Figure 4-2. TEM images of carbon nanotips (A) before and (B) after FIB milling. Scale bar, 100 nm.

The dual-beam FIB/SEM instrument allowed us to visualize the tip of a carbon nanoelectrode by FIB and SEM imaging before and after milling. The resolution of an SEM image was high enough to ensure the intact tip end prior to milling (Figure 4-3A) when the tip was protected from electrostatic damage (see below). The tip end of an FIB-milled carbon nanotip was also clearly seen by SEM, which enabled us to estimate the outer radius of each milled tip. This information was useful for the analysis of electrochemical data, which depend not only on the radius of a carbon tip, a, but also on the outer radius of the quartz sheath, r_g (= ~50 nm in Figure 4-3B). The outer radius of the smallest FIB-milled tip was practically limited to ~50 nm by the resolution of FIB imaging, which was needed to locate the tip position prior to milling (Figure 4-3C). Accordingly, the Ga^+ beam was focused slightly above the 50 nm-radius portion of the unmilled quartz nanopipet to yield a milled nanotip with an outer radius of ~50 nm as checked by FIB and SEM imaging (Figures 4-3B and 4-3D, respectively). Noticeably, the blurriness of SEM and FIB images is due to the charging of the insulating quartz surface.

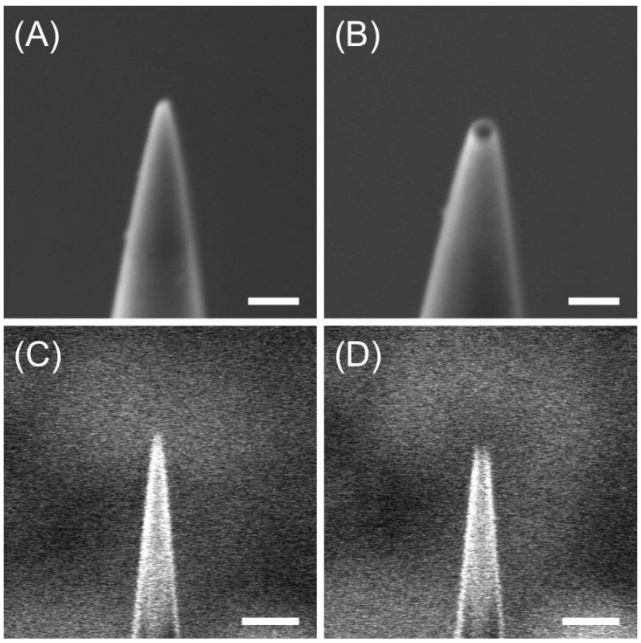

Figure 4-3. SEM images of (A) unmilled and (B) FIB-milled carbon nanotips and the corresponding FIB images in parts C and D, respectively. Scale bars: 200 nm in parts A and B, and 500 nm in parts C and D.

4.4.2 Voltammetric Characterization.

FIB-milled carbon nanoelectrodes were characterized by cyclic voltammetry (CV) to demonstrate their high electrochemical reactivity to the reduction of $Ru(NH_3)_6^{3+}$, which yielded nearly reversible CVs with well-defined limiting currents, $i_{T,\infty}$. The inner radius of a nanotip (a = 49 and 29 nm in Figures 4-4A and 4-4B, respectively) was determined from the limiting current by using eq 4 with $D = 6.7 \times 10^{-6}$ cm^2/s for $Ru(NH_3)_6^{3+}$ [39]. In addition, this analysis employed a simulated x value of 1.13 in eq 4 for an insulating outer wall with RG and θ values as determined by TEM. Thus, an inner tip radius determined voltammetrically gave an outer radius that is consistent with the outer radius estimated by SEM. Noticeably, we employed SECM to confirm

the size and geometry of an FIB-milled carbon nanotip as well as a lack of a conductive carbon film on the outer wall (see below).

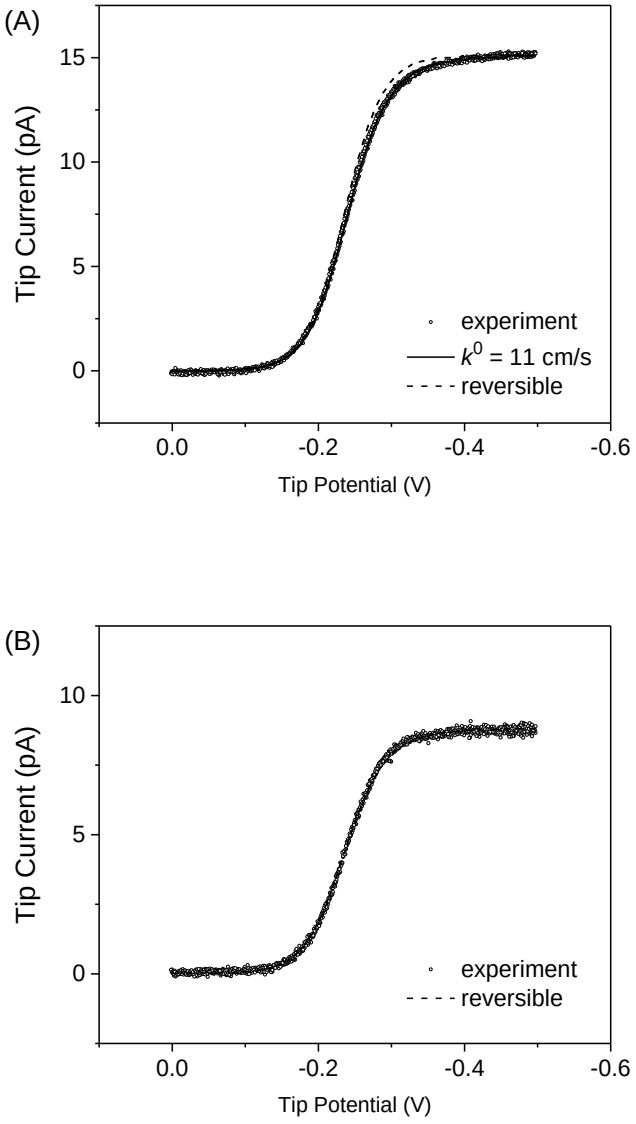

Figure 4-4. CVs (circles) of 1 mM $Ru(NH_3)_6Cl_3$ in PBS at (A) 49 and (B) 29 nm-radius tips of FIB-milled CVD carbon nanoelectrodes. Solid and dashed lines represent simulated CVs.

Nearly reversible CVs of $Ru(NH_3)_6^{3+}$ were analyzed to yield extremely high standard electron-transfer rate constants, k^0, of ≥10 cm/s by using four carbon nanoelectrodes with tip radii of <50 nm. For instance, the slightly quasi-reversible CV of $Ru(NH_3)_6^{3+}$ at the 49 nm-radius carbon electrode fitted well with a simulated CV with a k^0 value of 11 cm/s (i.e., $k^0a/D = 8$) and a transfer coefficient, α, of 0.5. On the other hand, the reversible CV of $Ru(NH_3)_6^{3+}$ at the 29 nm-radius carbon electrode yielded an even larger k^0 value of ≥23 cm/s (i.e., $k^0a/D \geq 10$). These k^0 values for $Ru(NH_3)_6^{3+}$ at FIB-milled carbon nanoelectrodes are close to k^0 values of 17 cm/s at platinum nanoelectrodes[40], 13 cm/s at gold nanoelectrodes[41], and 4 cm/s at individual single-walled carbon nanotubes[42]. Similar k^0 values for $Ru(NH_3)_6^{3+}$ among different electrode materials have been considered as evidence of adiabatic electron-transfer reactions[43,44]. We, however, emphasize that nanoelectrodes can be readily contaminated with adventitious impurities from ultrapure water[45] and ambient air, which may apparently limit k^0 values to the similar values[35]. Moreover, the electron-transfer kinetics of $Ru(NH_3)_6^{3+}$ at FIB-milled carbon nanotips may be affected by the implantation of gallium ion on the carbon surface[38]. In addition to these uncontrollable contaminants, the amorphous form of CVD carbon might have caused differences among the k^0 values obtained by using different FIB-milled carbon nanoelectrodes (Figure 4-4).

4.4.3 Approach Curves at an Insulating Substrate.

The well-defined geometry of FIB-milled carbon nanotips was confirmed by SECM approach curves at insulating substrates, where negative feedback responses are sensitive to the thickness of the insulating sheath[46,47] as well as the conductivity of the outer wall (see the Theory section). Experimentally, $Ru(NH_3)_6^{3+}$ was reduced at a carbon nanotip at a diffusion-limited rate while the tip approached a SiO_2-coated silicon wafer as a flat insulating substrate. Figure 4-5A

shows the resultant approach curve as obtained using a relatively large carbon nanoelectrode (a = 119 nm). The normalized experimental approach curve fitted well with a simulated approach curve for a tip with an insulating outer wall, but not with a curve for a tip with a conductive outer wall. The good fit was obtained by using an RG value of 1.4 as estimated by TEM. The theoretical analysis also yielded a very short distance of the closest approach, d_c, (i.e., the closest tip–substrate distance where the experimental curve fits with the theoretical curve) to be 8 nm, which confirms the flat tip end (Figure 4-2B). By contrast, much larger d_c values of 50–150 nm were reported for pyrolytic carbon nanoelectrodes with of a similar size (a = 120–150 nm and RG =1.5) at insulating substrates[14,15].

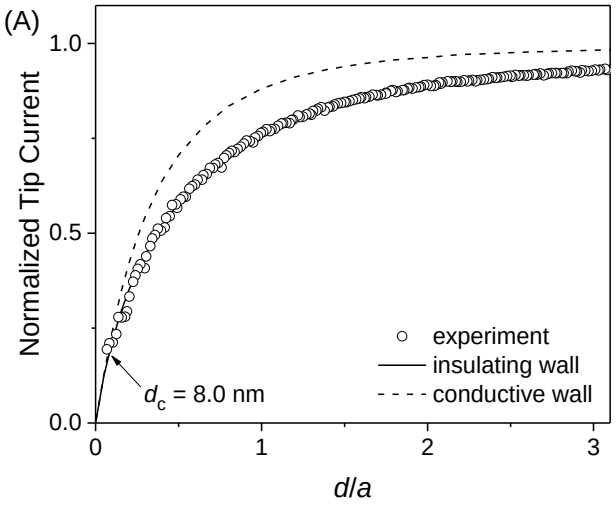

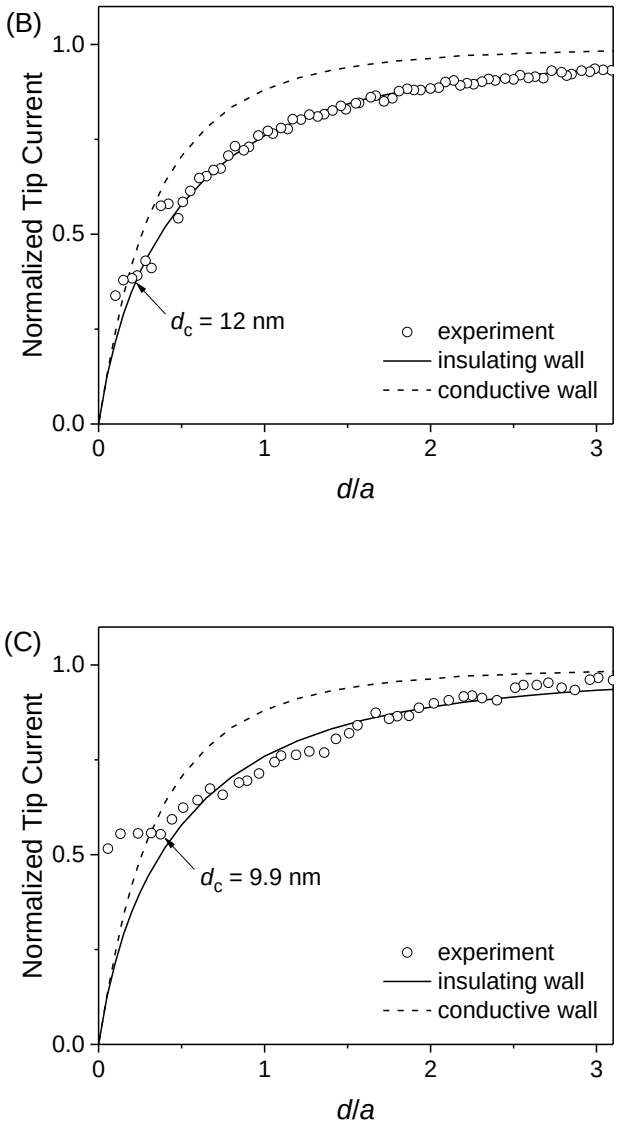

Figure 4-5. Approach curves of SiO_2-coated silicon wafers as obtained by using FIB-milled carbon nanotips with a = (A) 119, (B) 44, and 27 nm in PBS of 1 mM $Ru(NH_3)_6Cl_3$. Solid and dashed lines represent simulated curves.

Remarkably, good fits between experimental and simulated approach curves at an insulating substrate were obtained for FIB-milled nanoelectrodes with carbon radii of <50 nm.

Figures 4-5B and 4-5C show approach curves for FIB-milled carbon nanotips with a = 44 and 27 nm, respectively, where good fits were obtained at short distances of ~10 nm for the closest tip–substrate approach. These approach curves are strikingly different from those obtained previously with sub-100 nm-diameter carbon electrodes[14-17]. For instance, a radius of 6 nm was determined for a pyrolytic carbon nanoelectrode from a approach curve at an insulating substrate that showed a decrease of only 15% in the tip current and significantly deviated from SECM theory for a disk tip[15], thereby suggesting that the extremely small value of the tip radius may not be reliable. Noticeably, closest tip–substrate distances in this study were consistently ~10 nm for carbon nanotips with different radii (Figure 4-5), whereas the tip end was very flat (see Figure 4-2B). We speculate that the closest tip–substrate approach was limited by the contamination of tips, e.g., with aerosol nanoparticles during their storage in ambient air. Unfortunately, the cleaning of a carbon nanotip in piranha solution or by a UV cleaner damaged the tip end.

4.4.4 Approach Curves at a Conductive Substrate.

We employed FIB-milled carbon nanotips to study approach curves at gold-coated silicon wafers. Since the unbiased gold film was much larger than a carbon nanotip, we expected that a positive feedback response would be limited by the diffusion of $Ru(NH_3)_6^{3+}$ between the tip and the substrate[48,49]. A feedback response, however, was much lower than the diffusion-limited response when 5.0 mM $Ru(NH_3)_6Cl_3$ was employed (Figure 4-6A). The tip current was enhanced only by a factor of ~1.6 before the 134 nm-radius carbon tip nearly contacted the gold substrate to give much higher currents. Apparently, this approach curve agreed with a theoretical approach curve[50] limited by the irreversible oxidation of $Ru(NH_3)_6^{2+}$ at the gold surface to yield an electron-transfer rate constant, k_{et}, of 1.1 cm/s. The tip current, however, was limited not by the kinetics of

$Ru(NH_3)_6^{2+}$ oxidation, but by the subsequent transport of electrons through the thin gold film, because a higher positive feedback response was obtained as the concentration of $Ru(NH_3)_6Cl_3$ was lowered[51]. Specifically, approach curves with 1 and 0.2 mM $Ru(NH_3)_6Cl_3$ (Figures 4-6B and 4-6C, respectively) yielded the highest normalized tip currents of ~3.5 and ~6.0, respectively. The latter approach curve fitted well with the diffusion-limited approach curve at a conductive substrate to yield a short distance of 20 nm for the closet approach of the 139 nm-radius tip to the gold surface. Importantly, the limited conductivity of the gold films was manifested owing to extremely high mass-transport conditions under carbon nanotips, which requires a very high electron density on the gold film in the localized area. By contrast, the film conductivity was high enough to obtain high positive feedback responses by using 1 μm-diameter Pt tips[35], where a lower electron density on the film is needed. In addition, the CVs of $Ru(NH_3)_6Cl_3$ at a gold-coated silicon wafer gave a wider peak separation at a higher concentration of the redox species owing to an uncompensated resistance through a gold film, which was estimated to be 1.8×10^2 Ω according to the method proposed by McCreery and co-workers[52].

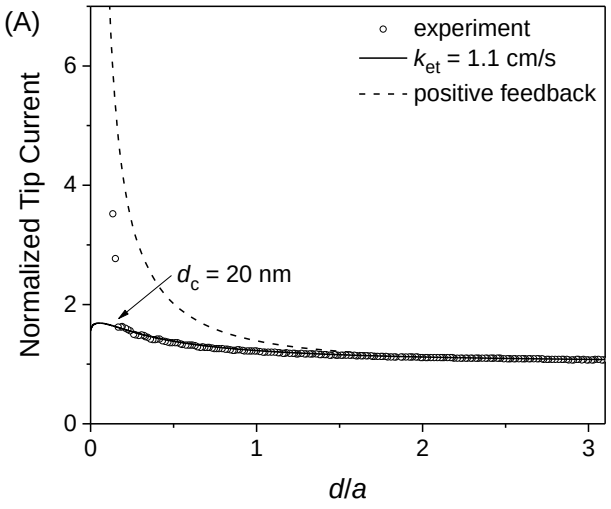

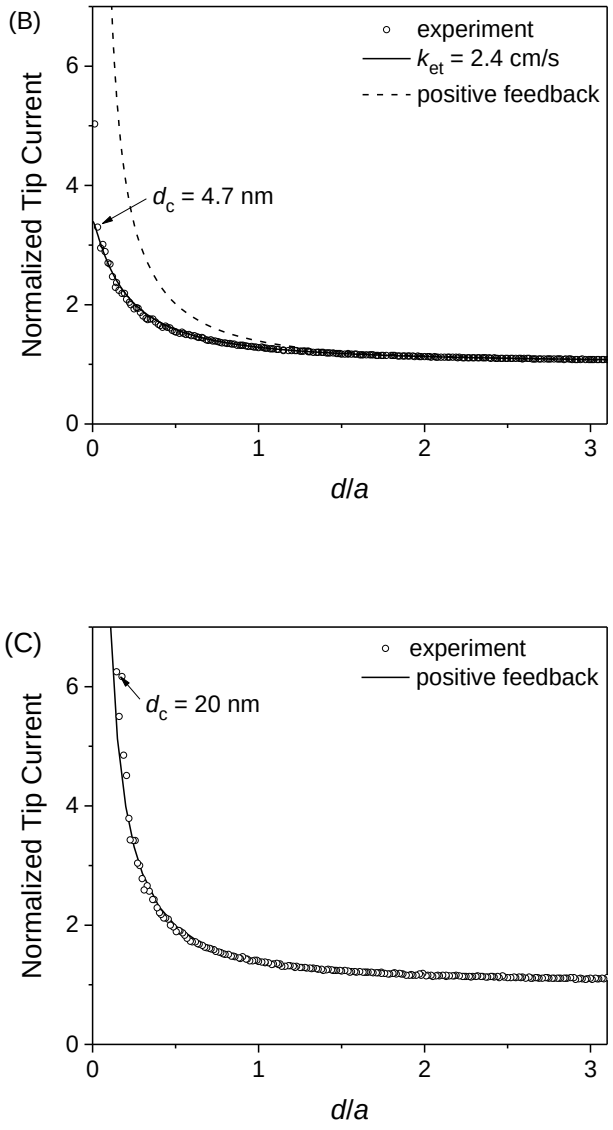

Figure 4-6. Approach curves at gold-coated silicon wafers as obtained with (A) 5.0, (B) 1.0, and (C) 0.2 mM $Ru(NH_3)_6Cl_3$ in PBS by using FIB-milled carbon nanotips with a = 134, 123, and 139 nm, respectively. Solid and dashed lines represent theoretical curves from ref. 50.

It was reported previously that a pyrolytic carbon nanoelectrode gave a positive feedback response that was much lower than a diffusion-limited response as expected for a platinum

substrate electrode[14]. The low feedback response was ascribed to a kinetic effect and was fitted with a kinetically limited theoretical response. The rather poor fit yielded an unrealistically low k_{et} value of 0.8 cm/s for the ferrocenemethanol couple in comparison with a k^0 value of 6.8 cm/s for this couple at platinum nanoelectrodes[40]. Alternatively, the low positive feedback response can be ascribed to the limited substrate conductivity[51] or the tip recession[53].

4.4.5 Electrostatic Tip Damage.

To enable quantitative nanoelectrochemical measurements discussed above, one has to avoid the nanoscale damage of carbon nanotips caused by electrostatic discharge (ESD)[30]. Specifically, the tip of a carbon nanoelectrode was maintained intact without ESD damage when an operator employed ESD protections[30] and handled the nanoelectrode under a high humidity of ~50% [31] in a plastic box equipped with a humidifier. In addition, we had to ground the lead wire of a carbon nanoelectrode when its tip was inspected by optical microscopy, where a sufficiently high humidity was not achievable. In fact, we found that ESD damage was caused unknowingly when the ungrounded lead wire of a carbon nanoelectrode contacted an insulated stage of the optical microscope under low humidity (<30%). ESD-damaged carbon nanotips had nanometer-sized pinholes when they were imaged by SEM prior to FIB milling (Figure 4-7A). In addition to pinholes, cracks were observed in FIB-milled carbon nanotips by SEM (Figure 4-7B) after they were used for CV measurements in the bulk solution. ESD damage was noticeable during the CV measurements, where the tip current was much higher than expected from the tip size owing to the diffusional access of $Ru(NH_3)_6^{3+}$ to the carbon surface through pinholes and cracks.

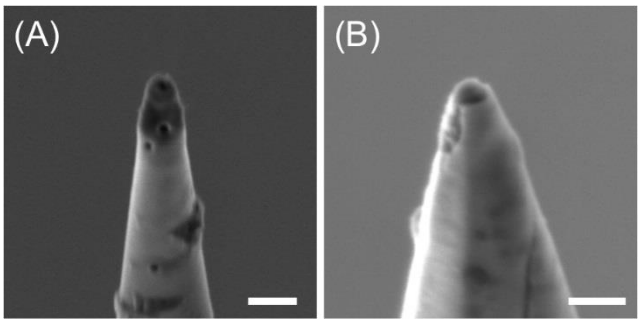

Figure 4-7. SEM images of (A) unmilled and (B) FIB-milled carbon nanotips with ESD damage. The latter tip was used for CV measurements in the bulk solution before SEM imaging. Scale bars: (A) 500 nm and (B) 200 nm.

4.5 CONCLUSIONS

In this work, we demonstrated that FIB-milled CVD carbon nanoelectrodes are useful as SECM nanotips with high electrochemical reactivity and well-controlled size and geometry. Flat carbon nanotips with inner and outer radii of down to ~27 and ~38 nm, respectively, were characterized by TEM and SEM and applied to SECM approach curve measurements. A lack of a conductive carbon layer on the outer tip wall was confirmed by approach curves at insulating substrates. FIB-milled carbon nanoelectrodes also revealed the limited conductivity of ~100 nm-thick gold films under extremely high mass-transfer conditions, where the carbon nanotips were sufficiently conductive and reactive. In addition, we found that nanopipet-supported CVD carbon tips can be damaged by ESD, while ESD damage was previously reported only for glass-sealed Pt

nanoelectrodes[30,31] and not for nanopipet-supported pyrolytic carbon tips[17]. Damage-free carbon nanoelectrodes will enable reliable and quantitative nanoelectrochemical measurements including high-resolution SECM imaging[54] and SECM-based nanogap voltammetry[28,35].

ACKNOWLEDGEMENTS

This work was supported by the National Science Foundation (CHE-1213452 for SA and CHE-1300158 for MM), the National Institutes of Health (R01 GM112656 for SA), and the *Air Force Office of Scientific Research* (MURI FA9550-14-1-0003 for MM).

4.6 REFERENCES

(1) Shen, M. ; Colombo, M. L. *Anal. Methods*, **2015**, *7*, 7095.

(2) Cox, J. T.; Zhang, B. *Annu. Rev. Anal. Chem.*, **2012**, *5*, 253.

(3) Strein, T. G.; Ewing, A. G. *Anal. Chem.*, **1992**, *64*,1368.

(4) Malinski, T.; Taha, Z. *Nature*, **1992**, *358*,676.

(5) Wu, W.-Z.; Huang, W.-H.; Wang, W.; Wang, Z.-L.; Cheng, J.-K.; Xu, T.; Zhang, R.-Y.; Chen, Y.; Liu, J. *J. Am. Chem. Soc.*, **2005**, *127*, 8914.

(6) Li, Y. T.; Zhang, S. H.; Wang, L.; Xiao, R. R.; Liu, W.; Zhang, X. W.; Zhou, Z.; Amatore, C.; Huang, W. H. *Angew. Chem., Int. Ed.*, **2014**, *53*, 12456.

(7) Schulte, A.; Chow, R. H. *Anal. Chem.*, **1998**, *70*, 985.

(8) Chen, S. L.; Kucernak, A. *J. Phys. Chem. B*, **2003**, *107*, 8392.

(9) Hussien, E. M.; Schuhmann, W.; Schulte, A. *Anal. Chem.*, **2010**, *82*, 5900.

(10) Xiong, H.; Guo, J.; Kurihara, K.; Amemiya, S. *Electrochem. Commun.*, **2004**, *6*, 615.

(11) Zoski, C. G.; Liu, B.; Bard, A. J. *Anal. Chem.*, **2004**, *76*,3646.

(12) Wong, D. K. Y.; Xu, L. Y. F. *Anal. Chem.*, **1995**, *67*, 4086 .

(13) Kim, Y.-T.; Scarnulis, D. M.; Ewing, A. G. *Anal. Chem.*, **1986**, *58*, 1782.

(14) Takahashi, Y.; Shevchuk, A. I.; Novak, P.; Zhang, Y.; Ebejer, N.; Macpherson, J. V.; Unwin, P. R.; Pollard, A. J.; Roy, D.; Clifford, C. A.; Shiku, H.; Matsue, T.; Klenerman, D.; Korchev, Y. E. *Angew. Chem., Int. Ed.*, **2011**, *50*, 9638 .

(15) Takahashi, Y.; Shevchuk, A. I.; Novak, P.; Babakinejad, B.; Macpherson, J.; Unwin, P. R.; Shiku, H.; Gorelik, J.; Klenerman, D.; Korchev, Y. E.; Matsue, T. *Proc. Natl. Acad. Sci. U. S. A.*, **2012**, *109*, 11540.

(16) McKelvey, K.; Nadappuram, B. P.; Actis, P.; Takahashi, Y.; Korchev, Y. E.; Matsue, T.; Robinson, C.; Unwin, P. R. *Anal. Chem.*, **2013**, *85*, 7519.

(17) Actis, P.; Tokar, S.; Clausmeyer, J.; Babakinejad, B.; Mikhaleva, S.; Cornut, R.; Takahashi, Y.; Cordoba, A. L.; Novak, P.; Shevchuck, A. I.; Dougan, J. A.; Kazarian, S. G.; Gorelkin, P. V.; Erofeev, A. S.; Yaminsky, I. V.; Unwin, P. R.; Schuhmann, W.; Klenerman, D.; Rusakov, D. A.; Sviderskaya, E. V.; Korchev, Y. E. *Acs Nano*, **2014**, *8*, 875.

(18) Nadappuram, B. P.; McKelvey, K.; Al Botros, R.; Colburn, A. W.; Unwin, P. R. *Anal. Chem.*, **2013**, *85*, 8070.

(19) Barton, Z. J.; Rodríguez-López, J. *Anal. Chem.*, **2014**, *86*, 10660.

(20) Kim, B. M.; Murray, T.; Bau, H. H. *Nanotechnology*, **2005**, *16*, 1317.

(21) Rees, H. R.; Anderson, S. E.; Privman, E.; Bau, H. H.; Venton, B. J. *Anal. Chem.*, **2015**, *87*, 3849 .

(22) Singhal, R.; Bhattacharyya, S.; Orynbayeva, Z.; Vitol, E.; Friedman, G.; Gogotsi, Y. *Nanotechnology*, **2010**, *21* .

(23) Hu, K.; Wang, Y.; Cai, H.; Mirkin, M. V.; Gao, Y.; Friedman, G.; Gogotsi, Y. *Anal. Chem.*, **2014**, *86*, 8897.

(24) Yu, Y.; Noël, J.-M.; Mirkin, M. V.; Gao, Y.; Mashtalir, O.; Friedman, G.; Gogotsi, Y. *Anal. Chem.*, **2014**, *86*, 3365 .

(25) Hu, K.; Gao, Y.; Wang, Y.; Yu, Y.; Zhao, X.; Rotenberg, S. A.; Gokmese, E.; Mirkin, M. V.; Friedman, G.; Gogotsi, Y. *J. Solid State Electrochem.*, **2013**, *17*, 2971.

(26) Yu, Y.; Gao, Y.; Hu, K.; Blanchard, P.-Y.; Noel, J.-M.; Nareshkumar, T.; Phani, K. L.; Friedman, G.; Gogotsi, Y.; Mirkin, M. V. *ChemElectroChem*, **2015**, *2*, 58.

(27) Amemiya, S., Nanoscale Scanning Electrochemical Microscopy, in *Electroanalytical Chemistry*, A. J. Bard and C. G. Zoski Editors, CRC Press, Boca Raton, FL, Vol. 26, 2015, 1.

(28) Nioradze, N.; Kim, J.; Amemiya, S., *Anal. Chem.*, **2011**, *83*, 828.

(29) Kim, J.; Izadyar, A.; Nioradze, N.; Amemiya, S. *J. Am. Chem. Soc.*, **2013**, *135*, 2321.

(30) Nioradze, N.; Chen, R.; Kim, J.; Shen, M.; Santhosh, P.; Amemiya, S. *Anal. Chem.*, **2013**, *85*, 6198.

(31) Kim, J.; Kim, B.-K.; Cho, S. K.; Bard, A. J. *J. Am. Chem. Soc.*, **2014**, *136*, 8173.

(32) Fosdick, S. E.; Knust, K. N.; Scida, K.; Crooks, R. M. *Angew. Chem., Int. Ed.*, **2013**, *52*, 10438.

(33) Minguzzi, A.; Alpuche-Aviles, M. A.; Rodríguez-López, J.; Rondinini, S.; Bard, A. J. *Anal. Chem.*, **2008**, *80*, 4055.

(34) Oleinick, A.; Yan, J.; Mao, B.; Svir, I.; Amatore, C. *ChemElectroChem*, **2016**, *3*, 487.

(35) Nioradze, N.; Chen, R.; Kurapati, N.; Khvataeva-Domanov, A.; Mabic, S.; Amemiya, S. *Anal. Chem.*, **2015**, *87*, 4836.

(36) Cai, H.; Wang, Y.; Yu, Y.; Mirkin, M. V.; Bhakta, S.; Bishop, G. W.; Joshi, A. A.; Rusling, J. F. *Anal. Chem.*, **2015**, *87*, 6403.

(37) Kim, J.; Shen, M.; Nioradze, N.; Amemiya, S. *Anal. Chem.*, **2012**, *84*, 3489.

(38) Ishitani, T.; Yaguchi, T. *Microsc. Res. Tech.*, **1996**, *35*, 320.

(39) Guo, J.; Amemiya, S. *Anal. Chem.*, **2005**, *77*, 2147.

(40) Sun, P.; Mirkin, M. V. *Anal. Chem.*, **2006**, *78*, 6526.

(41) Velmurugan, J.; Sun, P.; Mirkin, M. V. *J. Phys. Chem. C*, **2008**, *113*,459.

(42) Guell, A. G.; Ebejer, N.; Snowden, M. E.; McKelvey, K.; Macpherson, J. V.; Unwin, P. R. *Proc. Natl. Acad. Sci. U. S. A.*, **2012**, *109*, 11487.

(43) Iwashita, T.; Schmickler, W.; Schultze, J. W. *Ber. Bunsenges. Phys. Chem.*, **1985**, *89*, 138.

(44) Zhang, G.; Cuharuc, A. S.; Guell, A. G.; Unwin, P. R. *Phys. Chem. Chem. Phys.*, **2015**, *17*, 11827.

(45) Scherson, D. A.; Tolmachev, Y. V. *Electrochem. Solid-State Lett.*, **2010**, *13*, F1.

(46) Shao, Y.; Mirkin, M. V. *J. Phys. Chem. B*, **1998**, *102*, 9915.

(47) Amemiya, S.; Bard, A. J. *Anal. Chem.*, **2000**, 72, 4940.

(48) Wipf, D. O.; Bard, A. J. *J. Electrochem. Soc.*, **1991**, *138*, 469.

(49) Xiong, H.; Guo, J.; Amemiya, S. *Anal. Chem.*, **2007**, *79*, 2735.

(50) Cornut, R.; Lefrou, C. *J. Electroanal. Chem.*, **2008**, *621*, 178.

(51) Whitworth, A. L.; Mandler, D.; Unwin, P. R. *Phys. Chem. Chem. Phys.*, **2005**, *7*, 356.

(52) Ranganathan, S.; McCreery, R. L. *Anal. Chem.*, **2001**, *73*, 893.

(53) Sun, P.; Mirkin, M. V. *Anal. Chem.*, **2007**, *79*, 5809.

(54) Shen, M.; Ishimatsu, R.; Kim, J.; Amemiya, S. *J. Am. Chem. Soc.*, **2012**, *134*, 9856.

5.0 CHARACTERIZATION OF NANOPIPET-SUPPORTED ITIES TIPS FOR SCANNING ELECTROCHEMICAL MICROSCOPY OF SINGLE SOLID-STATE NANOPORES

This work has been accepted by *An. Chem.* as Chen, R.; Balla, R. J.; Lima, A. S.; Amemiya, S., Characterization of Nanopipet-Supported ITIES tips for Scanning Electrochemical Microscopy of Single Solid-State Nanopores. The thesis author fabricated electrodes, collected and analyzed experimental data.

5.1 INTRODUCTION

The power of nanoscale scanning electrochemical microscopy[1,2] (SECM) to image the chemical reactivity of single nanometer-sized objects is highly attractive for various applications including nanomaterial characterization. Such applications are exemplified by recent studies of single solid-state nanopores[3] and single metal nanoparticles.[4-7] Nanoscale SECM imaging, however, is still a challenging task owing to several technical difficulties, some of which were recently recognized and resolved,[8] i.e. thermal drift,[9] tip damage,[10] and adventitious contamination.[7,11] By contrast, a long-standing challenge is to reliably characterize the size and geometry of nanoelectrode tips,[1] which is required to quantitatively interpret SECM images. In fact, SECM was developed for more reliable in-situ characterization of the size and geometry of nanotips than other electrochemical methods.[12] Moreover, AFM[13] and scanning electron microscopy[10] (SEM) are useful, especially when a tip is protruded or recessed to complicate its

geometry. A higher resolution, however, is required to characterize very small tips (<100 nm) in detail.

Herein, we report on high-resolution transmission electron microscopy (TEM) of quartz nanopipet tips as supports of interfaces between two immiscible electrolyte solutions (ITIES) for nanoscale SECM imaging. TEM enables the characterization of <100 nm-diameter quartz nanopipets without metal coating,[14,15] which is usually made on nanopipets for SEM to inhibit charging and reduce thermal damage.[3,14,16,17] The TEM method was employed to examine carbon-filled nanopipets for SECM[18] in addition to non-filled nanopipets, which were further characterized by conductivity measurement in the aqueous electrolyte solution[19-21] and cyclic voltammetry at the nanopipet-supported ITIES.[21] Accordingly, this work is the first to assess the size and geometry of a nanopipet-supported ITIES by SECM with knowledge about the size and geometry of the nanopipet tip characterized by TEM. This assessment augments the reliability of nanopipet-supported ITIES, which found various electroanalytical applications[22-24] including high-resolution SECM imaging[3,25,26] and electrochemical sensing.[27,28] In addition, we optimize the intensity of the electron beam not to melt or deform insulating nanopipets during TEM characterization. The electron beam of SEM was previously used to melt quartz nanotips to smaller sizes.[29]

In this study, high-resolution TEM of quartz nanopipet tips allows us to quantitatively understand SECM images of single solid-state nanopores. Specifically, we image a nanoporous Si_3N_4 membrane by employing a nanopipet-supported ITIES tip (Figure 5-1A), where the amperometric current response based on the transfer of a target ion (tetrabutylammonium; TBA^+) is lowered over the pore wall by the negative feedback effect and is recovered over a nanopore to resolve it (Figure 5-1B). The Si_3N_4 membrane is perforated by a periodic array of 100 nm-diameter

nanopores in contrast to randomly distributed nanopores with various shapes and smaller sizes (~50 nm) as imaged in our previous study.[3] Moreover, we characterize quartz nanopipets by high-resolution TEM to determine a tip diameter of ~30 nm and a tip roughness of ~5 nm. Information about the size and geometry of nanopores and nanotips facilitates the finite element analysis of SECM images to reveal that the nanoscale ITIES supported by a rough nanopipet tip is represented by sphere-cap geometry and is also disturbed near nanopores, which are enlarged in their SECM images along the direction of the tip scan. High spatial resolution, however, is still achieved by scanning a sphere-cap tip at a very short distance from the substrate.

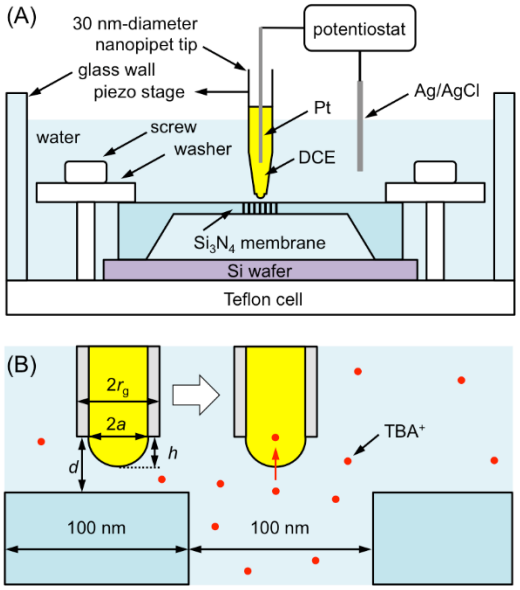

Figure 5-1. (A) An SECM cell with a nanoporous Si_3N_4 membrane and a DCE-filled nanopipet tip. (B) Constant-height SECM imaging of single Si_3N_4 nanopores.

5.2 EXPERIMENTAL SECTION

5.2.1 Chemicals and Materials.

Tetradodecylammonium (TDDA) bromide, 1,2-dichloroethane (DCE; >98%), tetrabutylammonium chloride, potassium chloride, and *N*-dimethyltrimethyl silylamine (Selectophore grade) were purchased from Sigma-Aldrich (Saint Louis, MO). Potassium tetrakis(pentafluorophenyl)borate (TFAB) was obtained from Boulder Scientific Company (Mead, CO). Isopropyl alcohol was obtained from J. T. Baker (Phillipsburg, NJ). All reagents were used as received. The TFAB salt of TDDA was prepared by metathesis.[30] 5 mM TBACl was dissolved with 0.3 M KCl in 18.3 MΩ cm deionized water obtained from a Milli-Q Advantage A10 water purification system (EMD Millipore, Billerica, MA) with a TOC value of 2 ppb as measured by using an internal online TOC monitor. The Milli-Q system was fed with the water (15.0 MΩ·cm) purified from tap water by using Elix 3 Advantage (EMD Millipore). The resulting solution was passed through a 0.02 μm filter (Whatman Anotop syringe filter, Sigma-Aldrich) before its use for SECM imaging of a nanoporous Si_3N_4 membrane (21585-10, Ted Pella, Redding, CA).

5.2.2 Tip Fabrication.

Quartz nanopipet tips were fabricated as reported elsewhere[3,9] with some modifications. A quartz capillary (O.D. 1 mm, I.D. 0.7 mm, 10 cm long, Sutter Instrument, Novato, CA) was air blow cleaned before pulling and was pulled in a CO_2-laser puller (Model P-2000, Sutter

Instrument). Approximately 30 nm-diameter nanopipets were obtained by running the line of a standard program[31] with parameters of heat = 700, filament = 4, velocity = 60, delay = 145, and pull = 125.

Modifications were made for cleaning and silanizing nanopipets. Specifically, pulled nanopipets were cleaned for three minutes in a plasma cleaner (PDC-32G, Harrick Plasma, Ithaca, NY). Ar was used as a carrier gas and passed through a water-filled bubbler to introduce water vapor into the chamber. The treatment of nanopipets with radio-frequency-generated Ar/H_2O plasma not only cleans the quartz surface, but also introduces hydroxyl groups on the surface[32] for more reproducible silanization. The clean nanopipets were dried for >1.5 hours under vacuum in a mini vacuum desiccator (Bel-Art Products, Pequannock, NJ) and then silanized by introducing 50 μL of *N*-dimethyltrimethyl silylamine into the desiccator. In this study, the mini desiccator was placed in a gas-purge desiccator cabinet (Bel-Art Products) filled with dry nitrogen. A silanization time was adjusted within a narrow range of 35 ± 5 min depending on the temperature and humidity of the atmosphere. After silanization, a vacuum was applied to the mini desiccator for ~1 min to remove the extra silanization agent.

5.2.3 TEM Characterization.

As-pulled quartz nanopipets were imaged by using a JEOL JEM-2100F microscope operating at 200 kV accelerating voltage. The intensity of the electron beam was optimized by adjusting “brightness” not to melt or deform a nanopipet tip.

5.2.4 SECM Measurement.

A homebuilt instrument[3] with an isothermal chamber[9] was used for nanoscale SECM imaging. A nanoporous Si_3N_4 membrane was cleaned for six minutes in piranha and for 11 minutes in Milli-Q water, and wet with isopropanol to prevent the formation of residual air bubbles in nanopores in the electrolyte solution[33] (Figure 5-1). Pt and Ag/AgCl wires were placed inside and outside of an organic-filled nanopipet (Figure 5-1A). Electrochemical measurements were carried out by using a commercial potentiostat (CHI 900A, CH Instruments, Austin, TX).

5.3 RESUTLS AND DISSCUSSION

5.3.1 High-Magnification TEM Images of Quartz Nanopipets.

We employed high magnifications of TEM to evaluate not only inner and outer diameters of quartz nanopipet tips ($2a$ and $2r_g$, respectively, in Figure 5-1B), but also their roughness. Specifically, we changed magnifications from ×50,000 to ×200,000 to obtain consistent inner and outer tip diameters of ~30 and ~42 nm, respectively (Figures 5-2A–5-2C). The corresponding *RG* value of $r_g/a = 1.4$ also agreed with the ratio of the outer diameter of a quartz capillary with respect to its inner diameter (1.0 mm and 0.7 mm, respectively). The consistent diameters and shape of a tip at various magnifications ensure that the electron beam did not melt or deform the tips without metal coating. Moreover, a pair of nanopipets pulled from the same capillary had nearly identical diameters and complementary shapes, which also supports that the tips were not melted or deformed by the electron beam. It should be noted that the TEM images were darkened

intentionally by employing the electron beam that had the sufficiently low intensity not to melt or deform the nanotips. The focal plane of the electron beam was adjusted to the central plane of a nanopipet as shown in Figures 5-2A–5-2C to measure inner diameters of 30 ± 2 nm for 12 quartz nanopipets with *RG* = 1.4 pulled by using the standard program.[31] By contrast, the electron beam was focused on the front side of a nanotip to estimate its roughness of ~5 nm (Figure 5-2D). The roughness of a borosilicate nanopipet tip was imaged previously by SEM, which required a metal-coated nanopipet with a larger diameter of ~150 nm.[17]

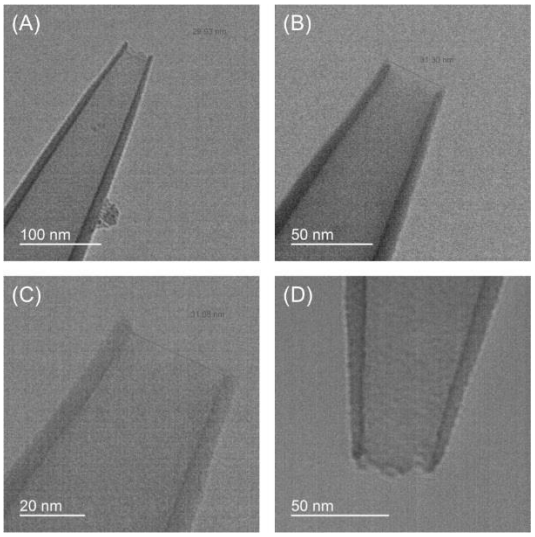

Figure 5-2. TEM images of a quartz nanopipet at (A) ×50,000, (B) ×100,000, and (C) ×200,000 as well as another nanopipet at (D) ×120,000.

The tip of a quartz nanopipet can be melted or deformed when the intensity of the electron beam is too high. This artifact was not pointed out in previous TEM studies of quartz nanopipets, which look deformed in some images. An intact nanopipet tip was imaged at various magnifications (Figures 5-2A– 5-2C) and then exposed to a more intense electron beam, which increased the inner tip radius, *a*, from 15 nm to 24 nm (Figure 5-3A). Such an outward deformation of a quartz nanopipet tip was observed also in the previous TEM study.[19] Another tip (Figure 5-

3B) was more seriously deformed when it was imaged by employing an even more intense electron beam to obtain a bright image at a higher magnification. The geometry of this deformed tip is very similar to the hourglass shape of a quartz nanopipet tip imaged by helium ion microscopy.[34] Also, the TEM image of a carbon-filled nanopipet tip showed an hourglass shape.[18]

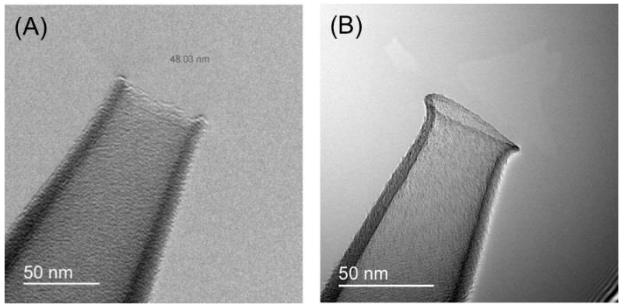

Figure 5-3. TEM images of nanopipets deformed by the electron beam at (A) ×80,000 and (B) ×100,000.

5.3.2 Nanopipet-Supported ITIES Tips.

In this study, quartz nanopipets were filled with an electrolyte solution of DCE to support nanoscale ITIES in the aqueous electrolyte solution of TBA^+ as a target ion (Figure 5-1). A Pt electrode was placed in an organic-filled nanopipet and biased against a Ag/AgCl electrode in the aqueous solution to drive the diffusion-limited transfer of TBA^+ across the nanopipet-supported ITIES. When the tip was positioned in the bulk solution, the corresponding amperometric limiting current, $i_{T,\infty}$, was given by

$$i_{T,\infty} = 4xzFDc_0a \quad (1)$$

where x depends on the tip geometry and equals to 1.18[35] for a disk tip with RG = 1.4, z (= +1) is the charge of the transferred ion, D (= 5.1 × 10^{-6} cm^2/s) and c_0 (= 5 mM) are the diffusion coefficient and concentration of the transferred ion in the bulk solution, respectively.

We found that a nanopipet-supported ITIES yielded a higher limiting current in the bulk solution than expected from eq 1 for a disk-shaped ITIES that is flush with the tip of a nanopipet. More quantitatively, eq 1 yields $i_{T,\infty}$ = 17.5 pA for a disk-shaped tip with a radius of 15 nm as determined for nanopipets by TEM. Experimental $i_{T,\infty}$ values, however, varied from ~20 pA to ~30 pA, which are likely dependent on the roughness of a nanopipet tip as well as .the degree of tip silanization. When a disk-shaped ITIES is assumed, these currents correspond to inner diameters of 34 nm–52 nm, which are too large in comparison with the inner diameters of nanopipet tips determined by TEM (30 ± 2 nm).

The higher currents at nanopipet-supported ITIES in the bulk solution are attributed to the sphere-cap geometry of the ITIES protruded from the tip of a pipet[36] as quantitatively supported by the finite element simulation (Supporting Information). For instance, a limiting current of 20.3 pA was obtained with a nanopipet-supported ITIES tip used for SECM imaging (see below) and was consistent with the current obtained by the finite element simulation of a sphere-cap tip with a = 15 nm, RG = 1.4, and h/a = 0.18 (h is the height of the sphere cap; see Figure 5-1B), thereby yielding x = 1.38 in eq 1. The actual height of this sphere-cap tip is only 2.7 nm, which is smaller than the roughness of the tip end estimated by TEM. By contrast, a much higher $i_{T,\infty}$ value of 27.9 pA was obtained with a nanopipet-supported ITIES tip for SECM imaging (see below) and was simulated for a sphere-cap tip with a = 15 nm, RG = 1.4, and h/a = 0.85 (i.e. h = 12.1 nm), where x = 1.89 in eq 1. It should be noted that the knowledge of nanopipet inner and outer diameters as obtained by TEM was essential to determine the height of the sphere-cap ITIES from a liming current by the finite element simulation.

5.3.3 SECM Imaging of Single Si_3N_4 Nanopores.

We employed nanopipet-supported ITIES tips for SECM to quantitatively image ion transport through single Si_3N_4 nanopores. In this study, we imaged a periodic array of circular nanopores with a diameter of 100 nm and a pore–pore separation of 100 nm as characterized by TEM (Figure 5-4) to facilitate the finite element analysis of their SECM images (see below). The nanopores were formed through a 200 nm-thick Si_3N_4 membrane, which was robust enough to self-stand in the aqueous electrolyte solution (Figure 5-1A). The Si_3N_4 membrane was also flat and oriented perpendicular to the tip, which can be scanned at a constant height without contact with the membrane surface over an area of 300 nm × 600 nm. The constant tip height was maintained by employing an isothermal chamber, which prevented the thermal drift of the tip position.[3,9] A single nanopipette was used to study 2-12 different locations of a single membrane. Overall, we studied 13 membranes and obtained good images with 10 membranes.

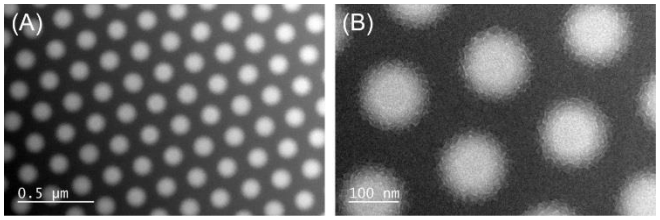

Figure 5-4. TEM images of a nanoporous Si_3N_4 membrane at (A) ×12,000 and (B) ×60,000.

Figure 5-5A shows an SECM image of an array of 100 nm-diameter Si_3N_4 pores, where the diffusion-limited tip current, i_T, was normalized against the tip current in the bulk solution, $i_{T,\infty}$. The normalized tip current, $i_T/i_{T,\infty}$, was reduced to ~0.70 by the negative feedback effect from the insulating membrane surface at $x = y = 0$, where the tip approached initially. The normalized tip

current was recovered to ~0.90 as the tip was scanned over the center of each nanopore, which mediated the flux of TBA^+ to the ITIES tip (Figure 5-1B). The periodicity of the nanopore array expected from the TEM image (Figure 5-4) was also seen in the SECM image. By contrast, nanopores in the SECM image look larger than their actual diameter and also slightly elongated along the direction of the tip scan, i.e. the *x*-direction. The diameter of a nanopore in the SECM image should be larger than its actual diameter by the tip diameter,[3] because the tip current is enhanced by the flux of TBA^+ from the nanopore even when the edge of the ITIES tip is positioned over the edge of a nanopore. This approximation was validated by the SECM image in the *y* direction, although the ITIES was slightly protruded from the nanopipet tip by $h/a = 0.18$ to yield $i_{T,\infty} = 20.3$ pA in eq 1 (see above). This result also implies that the SECM images of nanopores were enlarged along the *x* direction as ensured by the finite element analysis (see below).

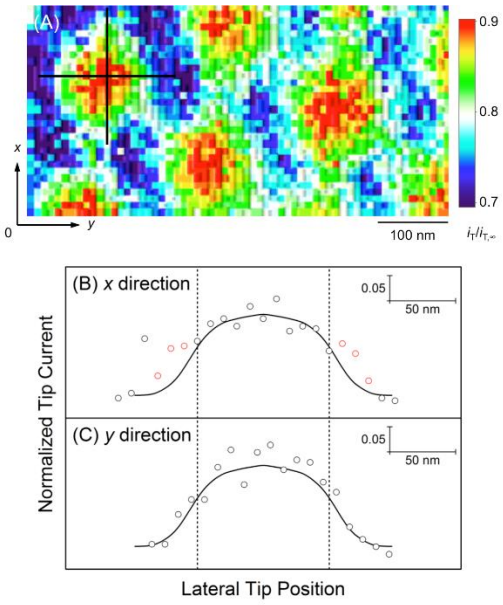

Figure 5-5. (A) A 300 nm × 600 nm SECM image of single Si_3N_4 nanopores as obtained with a sphere-cap nanopipet tip in 1 M KCl containing 5 mM TBACl. Cross sections (circles) as indicated by black lines in Part (A) along (B) *x* and (C) *y* directions. Red circles indicate the

experimental data points that broaden the nanopore image. Solid lines represent simulation results with a = 15 nm, r_g = 21 nm, h = 2.7 nm, and d = 14.25 nm. Dashed lines locate the edges of a 100 nm-diameter pore.

The finite element analysis indicates that the SECM image of a circular nanopore is enlarged along the x direction rather than contracted in the y direction. In this model, one cylindrical nanopore was considered and imaged with a sphere-cap tip (Figure 5-8A). A nanopipet–membrane distance, d, of 14.25 nm (Figure 5-1B) was employed in the simulation so that the simulated $i_T/i_{T,\infty}$ value increased from ~0.70 over the insulating membrane surface to ~0.90 over the center of the nanopore as observed experimentally along black lines across a nanopore in Figure 5-5A. The simulated tip current, however, was lower than the experimental current when the tip was scanned toward and away from the edge of a nanopore in the x direction, thereby elongating the experimental line scan (see red circles in Figure 5-5B for higher experimental currents). By contrast, no elongation was observed along the y direction (Figure 5-5C). It is unclear why the SECM image of nanopores looks elongated only in the x direction. However, this asymmetry of circular nanopores in their SECM images cannot be attributed to the drift of a tip positioner, which was mechanically locked.[7,8] Moreover, the SECM image of a nanopore was always elongated in the x direction when nanopore membranes were rotated with respect to the z direction. This result indicates that the elongation is not due to the presence of adjacent nanopores that can asymmetrically surround the central nanopore with respect to x and y directions. In fact, the finite element simulation showed no asymmetry between SECM line scans over a nanopore in x and y directions although it is surrounded by six closest nanopores asymmetrically between x

and *y* directions. This simulation result ensured that adjacent nanopores were located too far from the imaged nanopore to affect the tip current.

5.3.4 Single Nanopore Imaging with Largely Protruded ITIES Nanotips.

We also imaged single Si_3N_4 nanopores when the nanopipet-supported ITIES was largely protruded, i.e. $h/a = 0.85$. The large protrusion was noticeable, because a tip current of 27.9 pA in the bulk solution was much higher than expected for a disk-shaped ITIES supported by a nanopipet with a typical tip diameter of 30 nm. In fact, the experimental $i_{T,\infty}$ value corresponded to an inner diameter of 48 nm for a disk-shaped tip with $RG = 1.4$ in eq 1. However, the resultant SECM image of single nanopores (Figure 5-6A) yielded much higher spatial resolution than expected for a 48 nm-diameter disk-shaped tip.

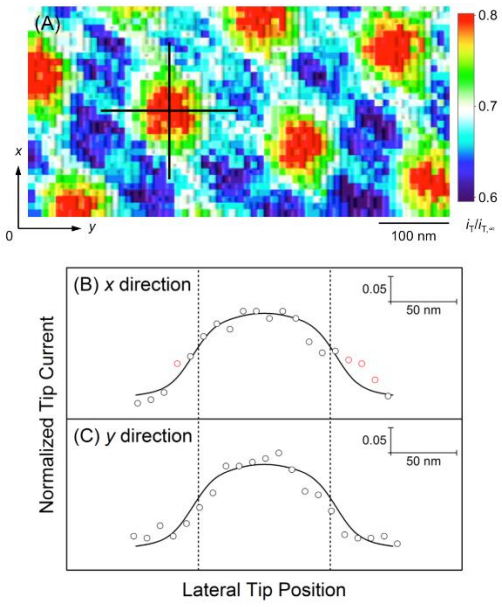

Figure 5-6. (A) A 300 nm × 600 nm SECM image of single Si_3N_4 nanopores as obtained with a sphere-cap nanopipet tip in 1 M KCl containing 5 mM TBACl. Cross sections (circles) as indicated by black lines in Part (A) along (B) *x* and (C) *y* directions. Red circles indicate the

experimental data points that broaden the nanopore image. Solid lines represent simulation results with a = 15 nm, r_g = 21 nm, h = 12.1 nm, and d = 16.8 nm. Dashed lines locate the edges of a 100 nm-diameter pore.

We employed the finite element method to better understand the SECM image of single nanopores as obtained with a largely protruded nanotip. The simulation of a sphere-cap tip with h/a = 0.85 accounted for not only the high $i_{T,\infty}$ value, but also the tip current during imaging when a nanopipet–membrane distance, d, of 16.8 nm was used. This distance corresponds to an actual separation, $d - h$, of only 4.7 nm between the membrane and the highest point of the sphere-cap ITIES (Figure 5-1B). The close distance of the sphere-cap tip from the membrane contributed to the high resolution of the SECM image as represented by line scans over the nanopore along the black lines in Figure 5-6A. Specifically, the corresponding experimental line scans in both x and y directions (Figures 5-6B and 5-6C, respectively) agreed well with line scans simulated for a sphere-cap tip with a = 15 nm and h = 12.1 nm, although the experimental tip current was slightly higher than the simulated current when the tip was scanned toward or away from the edge of the nanopore in the x direction (see red circles in Figure 5-6B). Such a deviation was observed also when a slightly protruded tip was used (Figure 5-5B).

5.3.5 A Comparison between Hemispherical and Disk Tips.

We performed the finite element simulation to compare the spatial resolution of SECM between hemispherical and disk tips (h/a = 1 and 0, respectively). In this simulation, we considered SECM line scans of two substrates. First, we simulated SECM line scans of a single nanopore (Figure 5-8A) based on the negative feedback mechanism as reported in this work. In addition, we

considered SECM line scans of a disk-shaped conductor embedded in an insulating substrate (Figure 5-8B) to examine the positive feedback mechanism.[37] In this case, the tip current is based on the electrolysis of a redox molecule and is enhanced by the conductor, which converts the tip-generated species to the original redox molecule.

Figure 5-7A shows SECM line scans of a nanopore with a disk-shaped tip as well as a hemispherical tip. A tip–substrate distance of $d/a = 0.75$ was selected for the disk tip to yield a normalized current of ~0.7 over the insulating surface. A nearly identical normalized current was obtained by positioning the hemispherical tip at $d/a = 1.3$ over the insulating surface, from which the highest point of the hemispherical tip was separated by only $d/a - h/a = 0.3$. These conditions mimic our experiments, where the tip approached to the insulating membrane surface until the tip current dropped to ~70% (Figures 5-5A and 5-6A). The simulated line scans of a nanopore show that the spatial resolution of the hemispherical tip (red circles) is comparable to that of the disk tip with the same radius (black circles). Noticeably, a higher current of the disk tip over the nanopore yielded a higher image contrast. A comparable image contrast was obtained by scanning the hemispherical tip at a shorter distance of $d/a = 1.1$ (blue circles). In this case, the highest point of the hemispherical tip was positioned at a very short normalized distance of 0.1 from the substrate surface, although, the tip of the cylindrical support (i.e. nanopipet) was still positioned farther from the substrate surface than the disk tip at $d/a = 0.75$.

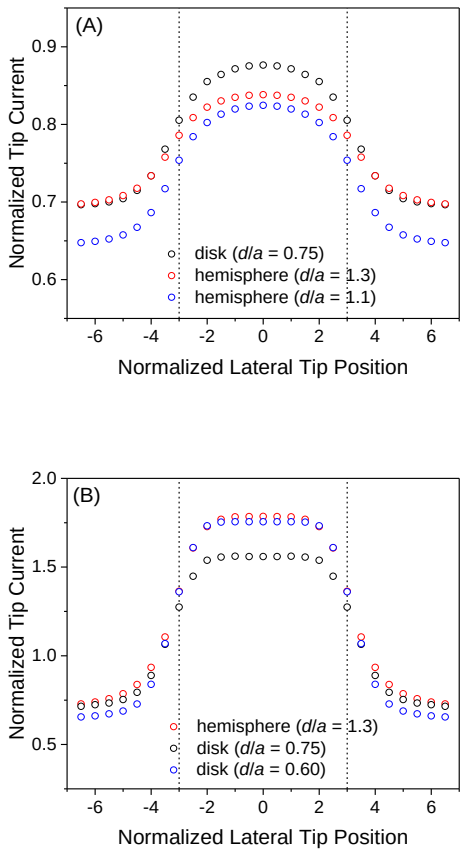

Figure 5-7. Finite element simulation of SECM line scans with disk and hemispherical tips over (A) single nanopore with a radius of 3*a* (dotted lines) and a length of 6*a* and (B) single conductive nanodisk with a radius of 3*a* (dotted lines). The lateral tip position was normalized against the tip radius, *a*.

SECM line scans of a conducive nanodisk were simulated by the finite element method to demonstrate that the spatial resolution based on the positive feedback mechanism is similar between a hemispherical tip (red circles in Figure 5-7B) and a disk-shaped tip with the same radius (black circles). In this simulation, both tips were positioned at different distances from the substrate surface so that their normalized current responses were nearly identical (i.e. ~0.70) over the insulating surface surrounding the nanodisk. The current responses of both tips were enhanced

over the conductive disk by the positive feedback effect to yield similar spatial resolutions. By contrast, the image contrast of the disk tip at this distance of d/a = 1.3 was lower than that of the hemispherical tip at the corresponding distance of d/a = 0.75, where the highest point of the hemispherical tip was positioned very close to the conductive disk, i.e. $d/a - h/a$ = 0.3. Image contrast was improved for the disk tip by scanning it a little closer to the substrate, i.e. d/a = 0.60 (blue circles). The corresponding spatial resolution, however, was still similar to the spatial resolution of the hemispherical tip, thereby confirming that the spatial resolution of disk and hemispherical tips is mainly determined by the tip radius.

5.4 CONCLUSIONS

In this study, we demonstrated a powerful combination of TEM of a nanopipet with SECM of a nanopipet-supported ITIES tip to advance quantitative SECM imaging at the nanoscale. The intrinsic size and roughness of quartz nanopipet tips were observable by TEM with higher resolution in this study than by SEM in previous studies,[3,14,16,17] not only because TEM does not need the metal coating of a nanopipet, but also because we optimized the intensity of the electron beam for TEM not to melt or deform the insulating nanotip at high magnification.[18,19,29,34] Moreover, a periodic array of 100 nm-diameter nanopores was imaged in this study in contrast to our previous study of randomly distributed nanopores with various sizes and shapes.[3] Information about the size and geometry of nanotips and nanopores was crucial for the reliable finite element analysis of SECM images, where the elongation of circular nanopores along the direction of the tip scan was identified.

In addition, this study compared protruded SECM tips for high-resolution imaging with disk tips, which are often desired. We ensured both experimentally and theoretically that spatial resolution is not compromised by using sphere-cap tips, which can be scanned in close proximity to a substrate without tip–substrate contact. This advantage of a sphere-cap tip originates from the protrusion of the tip from the insulating sheath in contrast to a flush disk tip, where the insulating sheath contacts a substrate to limit the closest tip–substrate distance.[38] To our knowledge, this work is the first to quantitatively compare tips with different geometries for SECM imaging. It will should be considered in future studies how the spatial resolution of SECM depends on the exact geometry of a protruded (or even recessed) tip, which can be more readily fabricated to facilitate high-resolution SECM imaging and also miniaturized to yield extremely small tips of down to a few nanometers.[39,40]

5.5 SUPPORTING INFORMATION

5.5.1 Finite Element Simulation.

The limiting current at a disk-shaped or sphere-cap tip in the SECM configuration was simulated by solving a three-dimensional (3D) diffusion problem with a cylindrical nanopore or disk-shaped conductor (Figures 5-8A and 5-8B, respectively) as defined in Cartesian coordinates. The origin of the coordinate axes was set at the center of the upper orifice of the nanopore or the disk center. Initially, the solution phase contains a target ion at a bulk concentration of c_0. The steady-state diffusion of a target ion in the solution phase was defined by

$$\frac{\partial c}{\partial t} = D\left(\frac{\partial^2 c}{\partial x^2} + \frac{\partial^2 c}{\partial y^2} + \frac{\partial^2 c}{\partial z^2}\right) = 0 \qquad (2)$$

where c is the ion concentration at (x, y, z). Ion diffusion in the inner organic solution does not affect the tip current, which is limited by the diffusion of the target ion in the outer aqueous solution. Accordingly, the zero ion concentration is used as the electrode surface boundary condition (red lines in Figure 5-8). The membrane surface and pore wall are impermeable to the target ion, which corresponds to zero flux perpendicular to these boundaries (black bold lines). Boundary conditions at simulation space limits are given by the bulk concentration of the ion, c_0 (blue lines). The simulation space is large enough to affect the simulated tip current less than 1.5 %.

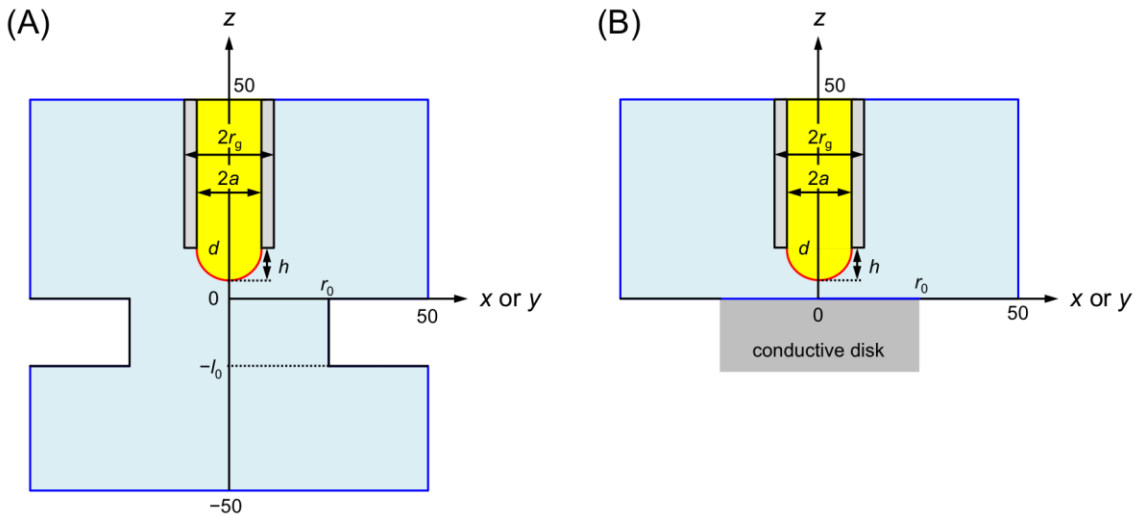

Figure 5-8. Scheme for the finite element simulation of SECM diffusion problems with a sphere-cap (or disk) tip positioned over (A) a nanopore and (B) a conductive nanodisk. Black boundaries are insulating, blue boundaries are simulation limits or a conductive substrate surface, and red boundaries are tip surfaces.

We employed COMSOL Multiphysics (version 5.2, COMSOL, Inc., Burlington, MA) to solve the 3D SECM diffusion problem in dimensionless form. Eq 2 was defined by dimensionless parameters as

$$\frac{\partial C}{\partial t} = \left(\frac{\partial^2 C}{\partial X^2} + \frac{\partial^2 C}{\partial Y^2} + \frac{\partial^2 C}{\partial Z^2} \right) = 0 \qquad (3)$$

where

$$C = \frac{c}{c_0} \tag{4}$$

$$t = \frac{4Dt}{a^2} \tag{5}$$

$$X = \frac{x}{a} \tag{6}$$

$$Y = \frac{y}{a} \tag{7}$$

$$Z = \frac{z}{a} \tag{8}$$

In addition, geometric parameters were defined by using dimensionless parameters as

$$L = \frac{d}{a} \tag{9}$$

$$H = \frac{h}{a} \tag{10}$$

This problem was solved numerically to calculate the normalized tip current, $i_T/i_{T,\infty}$, which was set to 1 at L = 25.

ACKNOWLEDGEMENTS

This work was supported by the National Institutes of Health (R01 GM112656). We thank Dr. Yu Yun and Prof. Michael V. Mirkin for their assistance with TEM of quartz nanopipets. A.S.L is thankful to grant #2013/16799-8, São Paulo Research Foundation (FAPESP).

5.6 REFERENCES

(1) Amemiya, S. Nanoscale Scanning Electrochemical Microscopy. In *Electroanalytical Chemistry*, Bard, A. J.; Zoski, C. G., Eds.; CRC Press, 2015, pp 1-72.

(2) Zoski, C. G. *Curr. Opin. Electrochem.* **2017**, *1*, 46.

(3) Shen, M.; Ishimatsu, R.; Kim, J.; Amemiya, S. *J. Am. Chem. Soc.* **2012**, *134*, 9856.

(4) Sun, T.; Yu, Y.; Zacher, B. J.; Mirkin, M. V. *Angew. Chem. Int. Ed.* **2014**, *53*, 14120.

(5) Yu, Y.; Sun, T.; Mirkin, M. V. *Anal. Chem.* **2015**, *87*, 7446.

(6) Blanchard, P.-Y.; Sun, T.; Yu, Y.; Wei, Z.; Matsui, H.; Mirkin, M. V. *Langmuir* **2016**, *32*, 2500.

(7) Kim, J.; Renault, C.; Nioradze, N.; Arroyo-Currás, N.; Leonard, K. C.; Bard, A. J. *J. Am. Chem. Soc.* **2016**, *138*, 8560.

(8) Kim, J.; Renault, C.; Nioradze, N.; Arroyo-Currás, N.; Leonard, K. C.; Bard, A. J. *Anal. Chem.* **2016**, *88*, 10284.

(9) Kim, J.; Shen, M.; Nioradze, N.; Amemiya, S. *Anal. Chem.* **2012**, *84*, 3489.

(10) Nioradze, N.; Chen, R.; Kim, J.; Shen, M.; Santhosh, P.; Amemiya, S. *Anal. Chem.* **2013**, *85*, 6198.

(11) Nioradze, N.; Chen, R.; Kurapati, N.; Khvataeva-Domanov, A.; Mabic, S.; Amemiya, S. *Anal. Chem.* **2015**, *87*, 4836.

(12) Mirkin, M. V.; Fan, F.-R. F.; Bard, A. J. *J. Electroanal. Chem.* **1992**, *328*, 47.

(13) Nogala, W.; Velmurugan, J.; Mirkin, M. V. *Anal. Chem.* **2012**, *84*, 5192.

(14) Yuill, E. M.; Sa, N. Y.; Ray, S. J.; Hieftje, G. M.; Baker, L. A. *Anal. Chem.* **2013**, *85*, 8498.

(15) Weber, A. E.; Baker, L. A. *J. Electrochem. Soc.* **2014**, *161*, H924.

(16) Wang, Y.; Velmurugan, J.; Mirkin, M. V.; Rodgers, P. J.; Kim, J.; Amemiya, S. *Analytical Chemistry* **2010**, *82*, 77-83.

(17) Elsamadisi, P.; Wang, Y.; Velmurugan, J.; Mirkin, M. V. *Anal. Chem.* **2011**, *83*, 671.

(18) Chen, R.; Hu, K.; Yu, Y.; Mirkin, M. V.; Amemiya, S. *J. Electrochem. Soc.* **2016**, *163*, H3032.

(19) Sa, N.; Baker, L. A. *J. Electrochem. Soc.* **2013**, *160*, H376.

(20) Perry, D.; Momotenko, D.; Lazenby, R. A.; Kang, M.; Unwin, P. R. *Anal. Chem.* **2016**, *88*, 5523.

(21) Cai, H.; Wang, Y.; Yu, Y.; Mirkin, M. V.; Bhakta, S.; Bishop, G. W.; Joshi, A. A.; Rusling, J. F. *Anal. Chem.* **2015**, *87*, 6403.

(22) Morris, C. A.; Friedman, A. K.; Baker, L. A. *Analyst* **2010**, *135*, 2190.

(23) Liu, S. J.; Li, Q.; Shao, Y. H. *Chem. Soc. Rev.* **2011**, *40*, 2236.

(24) Amemiya, S.; Wang, Y.; Mirkin, M. V. Nanoelectrochemistry at the liquid/liquid interfaces. In *Specialist Periodical Reports in Electrochemistry*, Compton, R. G.; Wadhawan, J. D., Eds.; RSC, 2013, p 1.

(25) Laforge, F. O.; Velmurugan, J.; Wang, Y.; Mirkin, M. V. *Anal. Chem.* **2009**, *81*, 3143.

(26) Wang, Y.; Kececi, K.; Velmurugan, J.; Mirkin, M. V. *Chem. Sci.* **2013**, *4*, 3606.

(27) Colombo, M. L.; Sweedler, J. V.; Shen, M. *Anal. Chem.* **2015**, *87*, 5095.

(28) Colombo, M. L.; McNeil, S.; Iwai, N.; Chang, A.; Shen, M. *J. Electrochem. Soc.* **2016**, *163*, H3072.

(29) Steinbock, L. J.; Steinbock, J. F.; Radenovic, A. *Nano Lett.* **2013**, *13*, 1717.

(30) Guo, J.; Amemiya, S. *Anal. Chem.* **2006**, *78*, 6893.

(31) Manual of P-2000 laser puller from Sutter Instruments.

(32) Kokkoli, E.; Ochsenhirt, S. E.; Tirrell, M. *Langmuir* **2004**, *20*, 2397.

(33) Kim, E.; Xiong, H.; Striemer, C. C.; Fang, D. Z.; Fauchet, P. M.; McGrath, J. L.; Amemiya, S. *J. Am. Chem. Soc.* **2008**, *130*, 4230.

(34) Zweifel, L. P.; Shorubalko, I.; Lim, R. Y. H. *ACS Nano* **2016**, *10*, 1918.

(35) Lefrou, C. *J. Electroanal. Chem.* **2006**, *592*, 103.

(36) Ishimatsu, R.; Kim, J.; Jing, P.; Striemer, C. C.; Fang, D. Z.; Fauchet, P. M.; McGrath, J. L.; Amemiya, S. *Anal. Chem.* **2010**, *82*, 7127.

(37) Bard, A. J.; Mirkin, M. V.; Unwin, P. R.; Wipf, D. O. *J. Phys. Chem.* **1992**, *96*, 1861.

(38) Cornut, R.; Bhasin, A.; Lhenry, S.; Etienne, M.; Lefrou, C. *Anal. Chem.* **2011**, *83*, 9669.

(39) Kim, J.; Kim, B.-K.; Cho, S. K.; Bard, A. J. *J. Am. Chem. Soc.* **2014**, *136*, 8173.

(40) Kim, J.; Bard, A. J. *J. Am. Chem. Soc.* **2016**, *138*, 975.

6.0 CONCLUSIONS

Chapter 2 shows the electrochemical reactivity of PS-supported CVD-grown graphene for FcMeOH couple to be at least 2–3 orders of magnitude higher than that of PMMA-transferred graphene. Remarkably, k^0 values of ≥25 cm/s at PMMA-free graphene exceeded the highest k^0 value reported for the FcMeOH couple so far, which is 6.8 cm/s at Pt nanoelectrodes. The unprecedentedly high electrochemical reactivity of CVD-grown graphene is highly significant both fundamentally and practically. In addition, we also demonstrate the electrochemical transparency of atomically thin graphene, where a supporting material can affect ET kinetics. The hydrophobic airborne contamination of graphene must be prevented to reliably study the electrochemical reactivity of graphene not only to outer-sphere redox couples, which are typically multiply charges and hydrophilic, but also to inner-sphere redox couples, which are surface sensitive.

Chapter 3 demonstrates the advantage of SECM-based nanogap voltammetry to assess the cleanness of a substrate electrode surface in solution by confirming that airborne contamination of the HOPG surface causes the non-ideal asymmetry of paired nanogap voltammograms of the $Fc^{2+/+}$ couple. In fact, symmetric pairs of nanogap voltammograms were obtained with the water-protected HOPG surface, where airborne contamination was significantly suppressed. In this study, the HOPG potential was cycled slowly at 0.05 V/s to address the ET kinetics with the minimal effect of Fc^+ adsorption on the HOPG surface, which was too weak to be quantitatively studied from the small hysteresis of the resultant nanogap voltammogram. Interestingly, SECM-based nanogap voltammetry will enable us to quantitatively study local Fc^+ adsorption on the HOPG surface by employing faster potential sweep rates, which requires the precise measurement of a

sub-nA tip response at the sub-millisecond resolution without crosstalk with a sub-mA substrate response. Advantageously, SECM-based nanogap voltammetry is free from charging current, which is a serious obstacle in the quantitative electrochemical study of surface adsorption.

We applied SECM-based nanogap voltammetry to estimate extremely high k^0 values of ≥12 cm/s for the outer-sphere ET reaction of the $Fc^{2+/+}$ couple at the water-protected HOPG surface. These k^0 values are much higher than those of 0.1−1 cm/s as estimated with the "pristine" HOPG surface, which was exposed to ambient air during the whole kinetic measurement by scanning electrochemical cell microscopy. Our k^0 values are still diffusion-limited minimum values, thereby requiring narrower tip–HOPG gaps of <50 nm to determine an actual k^0 value without a diffusion limit. Significantly, no Fc^{2+} adsorption on the HOPG surface excludes inner-sphere ET and electron-exchange pathways. A reliable outer-sphere redox couple will be useful to address various mechanistic questions about heterogeneous electron transfer including its adiabaticity. By contrast, the outer-sphere character of a redox couple is often argued when its voltammogram is unaffected by the modification of the electrode surface with a molecularly thin film. This approach is more general, but is inconclusive when a redox couple gives reversible voltammograms at both modified and unmodified electrodes, because an actual k^0 value at the modified surface may be lower than at the unmodified surface.

Chapter 4 demonstrates that FIB-milled CVD carbon nanoelectrodes are useful as SECM nanotips with high electrochemical reactivity and well-controlled size and geometry. Flat carbon nanotips with inner and outer radii of down to ~27 and ~38 nm, respectively, were characterized by TEM and SEM and applied to SECM approach curve measurements. A lack of a conductive carbon layer on the outer tip wall was confirmed by approach curves at insulating substrates. FIB-milled carbon nanoelectrodes also revealed the limited conductivity of ~100 nm-thick gold films

under extremely high mass-transfer conditions, where the carbon nanotips were sufficiently conductive and reactive. In addition, we found that nanopipet-supported CVD carbon tips can be damaged by ESD, while ESD damage was previously reported only for glass-sealed Pt nanoelectrodes and not for nanopipet-supported pyrolytic carbon tips. Damage-free carbon nanoelectrodes will enable reliable and quantitative nanoelectrochemical measurements including high-resolution SECM imaging and SECM-based nanogap voltammetry.

Chapter 5 shows a powerful combination of TEM of a nanopipet with SECM of a nanopipet-supported ITIES tip to advance quantitative SECM imaging at the nanoscale. The intrinsic size and roughness of quartz nanopipet tips were observable by TEM with higher resolution in this study than by SEM in previous studies, not only because TEM does not need the metal coating of a nanopipet, but also because we optimized the intensity of the electron beam for TEM not to melt or deform the insulating nanotip at high magnification. Moreover, a periodic array of 100 nm-diameter nanopores was imaged in this study in contrast to our previous study of randomly distributed nanopores with various sizes and shapes. Information about the size and geometry of nanotips and nanopores was crucial for the reliable finite element analysis of SECM images, where the elongation of circular nanopores along the direction of the tip scan was identified.

In addition, in Chapter 5 we compared protruded SECM tips for high-resolution imaging with disk tips, which are often desired. We ensured both experimentally and theoretically that spatial resolution is not compromised by using sphere-cap tips, which can be scanned in close proximity to a substrate without tip–substrate contact. This advantage of a sphere-cap tip originates from the protrusion of the tip from the insulating sheath in contrast to a flush disk tip, where the insulating sheath contacts a substrate to limit the closest tip–substrate distance.[38] To our

knowledge, this work is the first to quantitatively compare tips with different geometries for SECM imaging. It will should be considered in future studies how the spatial resolution of SECM depends on the exact geometry of a protruded (or even recessed) tip, which can be more readily fabricated to facilitate high-resolution SECM imaging and also miniaturized to yield extremely small tips of down to a few nanometers.

The achievements in Chapter 2 and 3 will make contribution not only to understanding the intrinsic reactivity of carbon materials, but also in the practical application of carbon nanomaterials. The high reactivity of graphene electrodes will open up new opportunities for its electrochemical application. The water-assisted protection method for HOPG surface can open up ways to maintain a clean surface for other nanomaterials, and the SECM-based nanogap voltammetry can be applied to check the cleanness of the surface in situ.

The work in Chapter 4 and 5 provides techniques to fabricate small and reliable nanoelectrodes as well as methods to characterize them properly. These nanoelectrodes will find application in the electrochemical mapping of surfaces and interfaces, imaging and activity study of biological structures in vivo or in vitro.

Based on these achievements, nanoscale SECM will become an even more powerful technique to characterize and understand various nanomaterials and interfaces.